De novo design of allosterically driven disassembly of protein complexes

Adam J. Broerman

A dissertation

submitted in partial fulfillment of the

requirements for the degree of

Doctor of Philosophy

University of Washington

2025

Reading Committee:

David Baker, Chair

Cole A. DeForest

Dustin J. Maly

Program Authorized to Offer Degree:

Chemical Engineering

University of Washington

Abstract

De novo design of allosterically driven disassembly of protein complexes

Adam J. Broerman

Chair of the Supervisory Committee:

David Baker

Department of Biochemistry

Protein design has focused on the design of ground states, ensuring they are sufficiently low energy to be highly populated. Designing the kinetics and dynamics of a system requires, in addition, the design of excited states that are traversed in transitions from one low-lying state to another. This is a challenging task as such states must be sufficiently strained to be poorly populated, but not so strained that they are not populated at all, and because protein design methods have mainly focused on creating near-ideal structures.

We developed a general approach for designing systems that use an induced-fit forcing motion to generate a strained excited state, allosterically driving protein complex dissociation in a process termed “facilitated dissociation.” Kinetic binding measurements demonstrate that incorporating excited states enables design of effector-induced acceleration of dissociation as high as 5,700-fold. Crystal structures throughout the facilitated dissociation process demonstrate accurate

design of such excited states. Within these excited states, we find that strain distributes nonuniformly depending on local topology, leading to kinetic asymmetry. Kinetic binding measurements with multiple effectors show that flexibility facilitates the force-generating conformational transition used to rapidly form the strained excited state.

We further investigated whether facilitated dissociation could enable faster-timescale control over cellular processes. Many cytokines form tight complexes with their receptors that dissociate or degrade on timescales of hours, so controlling the temporal dynamics of signaling is difficult: there is no off switch. We designed an off-switchable IL-2 mimic, enabling seconds-timescale control over its signaling, and used this tool to investigate early events in IL-2 signaling. This also demonstrated the generality of our approach: in principle, by fusing to our switch, almost any binder can be made to rapidly dissociate in the presence of effector.

Overall, this work provides a route to designing the rates and pathways of protein motion and change, which should ultimately enable construction of complex lifelike protein machines demanding precise timing and rapid functional change.

Table of Contents

Acknowledgements

Doing my PhD in the Baker lab has been one of the greatest experiences of my life. This is largely due to the fantastic people I've been privileged to work with and the dynamic research environment they have collectively cultivated. Working in this lab with you all has been intellectually stimulating and existentially satisfying. I would like to thank everyone in the lab for making this experience possible.

I was mentored by several people over the course of my PhD. Thanks to Ryan Kibler and Nick Woodall for getting me started, teaching me Rosetta and how to approach designing proteins. Thanks to Kejia Wu for modeling a way to think about science and life. Thanks to Phil Leung for showing me how to design switch proteins, writing a multistate design codebase with me, and steadily answering my endless design questions. And thanks to Florian Praetorius for rescuing me when I was floundering, for ideating with me, for teaching me how to write papers, for engendering community in all situations, and thus for being a role model for how to conduct science and for how to conduct one's life.

Thanks to Team Crispy Shifty: Florian Praetorius, Phil Leung, Cullen Demakis, Abbas Idris, Annika Philomin, and Kathryn Shelley. Thank you for providing a home for excitement around designing proteins that move.

Thanks to my collaborators: Christoph Pollmann in Jacob Piehler's lab, Yang Zhao and Masato Ogishi in Chris Garcia's lab, Maxx Tessmer and Mark Jackson in Stefan Stoll's lab, Harry Ryu in Dan Zuckerman's lab, Enrico Rennella in Lewis Kay's lab, and Surya Deopa in Tom Perkins' lab. Thank you for collaborating in characterizing our designed systems and for patiently helping me learn about your areas of expertise.

Thanks to all the students and postdocs I've mentored: Mauriz Lichtenstein, Will Grubbe, Ganyu Chen, Pooja Bandawane, and Tabitha Tcheau. Thanks to every one of you for being a constant source of inspiration and energy, for showing me how to grow as a mentor, and for working assiduously to push science forward. Thanks also to the rotation students I've mentored, Riley Quijano, Bianka Haro, Peixi Chen, and Shirley Ji, for your hard work and willingness to learn.

Thanks to David Baker for fostering a research environment that allows budding scientists to thrive, for recruiting me into opportunities that enable me to make my ideas reality, and for always pushing me to solve the next big problem.

Thanks to everyone else in the lab who I've worked with directly or talked with extensively: Arvind Pillai and Jinwei Xu for our far-ranging conversations; Cullen Demakis for all our discussions about motors; Green Ahn, Kirsten Thompson, Christina Savvides, and Mohamad Abedi for sharing ideas and working together on designing complex therapeutics; Basile Wicky, Lukas Milles, and Magnus Bauer for biophysics discussions; and Chuanyun Xu for helping me conceptualize neuroscience.

Thanks to Stacey Gerben and the General Production Core for producing large amounts (grams!) of high-quality protein, Asim Bera and the Crystal Core for solving many (14!) structures of my designs, Xinting Li and the Peptide Core for synthesizing peptides and measuring mass spectra of many of my designs, and Lance Stewart, Lynda Stuart, Luki Goldschmidt, Kandise VanWormer, Ian Haydon, and the rest of lab administration and management for all their work supporting science.

Thanks to my housemates Jorge, Lauren, Sean, and Lily for fun shenanigans and human connection during lockdown. Thanks to Linna and Amijai for co-hosting some great cookouts with me. Thanks to Jeremy, Harley, Dmitri, Linna, Derrick, Brian, Nico, Phil, Stacey, Erin, Clara, Lisa, Claire, Michelle, Sasha, and many others for awesome bouldering sessions over the years. Thanks to Jinwei for partnering up with me in learning how to ski. Thanks to everyone who has joined me for a hike/bike/run/kayak/ski. And thanks to Harley and Phil for introducing me to Seattle's metal scene.

Finally, I would like to thank my parents for expending so much effort in personalizing my education and for patiently nurturing, rather than suppressing, my incessant activity and curiosity. It must have been exhausting, but I think this trait has been the most important for my success in my PhD. And I would like to thank Claire for her complementary personality, mediating presence, and steadfast companionship.

Chapter I | Theoretical and practical basis for designing dynamic protein systems

Figures from Praetorius, F., Leung, P. J. Y., Tessmer, M. H., Broerman, A. J. *et al.* **Design of stimulus-responsive two-state hinge proteins.** *Science* **381**, 754–760 (2023). https://doi.org/10.1126/science.adg7731

Protein structure and functional dynamics

Proteins are the principal functional molecules of living systems, with complex 3D shapes that primarily determine their function. Proteins are constructed from “amino acid” building blocks. There are 20 naturally occurring amino acid molecules; each has a common “backbone” region that attaches to other amino acids and a unique “side chain” region that provides each amino acid with unique properties. To form proteins, the backbone atoms of amino acids are chained together into long polymers. Interactions between the amino acid side chains promote folding of the polymer into a 3D “tertiary” structure. Thus, the specific sequence of amino acids in the protein is the primary determinant of its structure and function.

Certain “secondary” structures form mostly due to interactions between the backbone atoms in the protein. The most common are alpha helices (in which the polymer coils into a helical structure) and beta sheets (in which parallel or antiparallel strands layer into sheets). Because the backbone atoms are identical across all amino acids, these structures can form somewhat independently of the side chain chemistry and so form common structural motifs that stably present the side chain atoms to interact with other amino acids more distant in the primary amino acid sequence, promoting formation of the 3D tertiary structure.

As part of their function, proteins act on other molecules. As a prerequisite to function, a protein generally must first bind to the molecule it acts on. The binding activity of a protein depends on its structure: a protein will bind to molecules that are shape-complementary to its surface. In this way, the protein structure can determine its function.

Proteins are dynamic molecules—at least because they begin as dynamic unfolded chains before folding into more defined structures. While some functions can be achieved by a final folded protein structure that is static and rigid, other functions require dynamic interchange among multiple folded conformations. For example, some enzymes close around their substrates to properly catalyze a reaction then open to release the reaction products, and other enzymes are regulated by binding effector molecules that stabilize them in either an active or inactive conformation. In extreme cases, the protein may not fold at all and instead perform its function while remaining completely disordered; such intrinsic disorder is increasingly being recognized as critical for certain functions.

Protein behavior can be modeled quantitatively using energy landscape theory[1]. In this model, each conformation of a protein has an associated free energy determined by the totality of the atomic interactions within the protein and between the protein and its environment. A protein will populate each conformation according to a Boltzmann distribution over these energies. Thus, proteins generally populate low-energy conformations at the bottom of energy wells; the energy difference between two wells defines the occupancy ratio between the corresponding conformational states. Proteins generally transition between wells along the paths through conformational space with the lowest energy barrier, the height of which defines the rate of the transition.

Binding interactions provide energy and can occur with specific conformational states; thus, adding a binding effector is a common way to perturb energy landscapes to switch protein function by reducing the energy of a specific conformation (Fig. 1A, right). The higher the binding affinity, the stronger the perturbation effector binding provides.

There are two basic mechanisms through which binding-responsive conformational change can occur: induced fit, in which first the effector binds and induces the subsequent conformational change, and conformational selection, in which the protein first spontaneously switches into the alternate conformation, then the effector binds to stabilize that change[2]. These mechanisms have important kinetic differences. Binding by conformational selection always can occur since, according to energy landscape theory, all conformations are populated to some degree, but will be quite slow when the energy difference or energy barrier between conformations is high in the absence of effector. Binding by induced fit can be faster in these situations because the effector can bind directly to the ground state conformation (rather than a rarer higher-energy conformation) and because the presence of the effector can lower energy barriers for the conformational change. Full binding mechanisms can involve multiple steps, each of which can have a more induced fit or conformational selection character. In particular, induced fit is equivalent to many small conformational selection steps along the reaction coordinate, each stabilized by forming new interactions with the effector.

De novo design of dynamic proteins

Computational methods have recently enabled completely new-to-nature (*de novo*) proteins to be reliably designed to perform desired functions[3]. Structure-based *de novo* protein design generally follows a standard pipeline. First, given a desired function, we determine structural requirements for the protein to perform that function. Second, we generate protein backbone structures satisfying those requirements, and for each backbone, design amino acid sequences that should stabilize the protein in the designed structure. We typically use parametric or deep learning–based methods such as RFDiffusion[4] for backbone generation and ProteinMPNN[5] for sequence design (soon, models that simultaneously generate structure and sequence in one step will likely replace these). Finally, we filter this set of designed sequences by their likelihood to fold into the desired structure satisfying all requirements (typically using structure prediction methods like AlphaFold[6]) and select the most promising designs for experimental testing.

We recently have developed methods to design proteins that switch between multiple well-defined conformations in response to stimuli[7]. Standard protein design methods optimize sequences for ideal backbones to fold into a deep energy well corresponding to a single stable state; multi-state protein design is a more challenging task since it requires designing a single sequence with multiple distinct energy minima. To simplify this challenge, we first designed hinge-like proteins in which two rigid domains move relative to each other while remaining individually folded, and in one conformation can bind a helical effector peptide (Fig. 1B–D). We reasoned that this approach would provide large conformational changes while changing few local interactions, helping to ensure the energy difference and energy barrier between states is small so that both states are kinetically and thermodynamically accessible. Binding the effector would stabilize one conformation over the other, altering the conformational equilibrium.

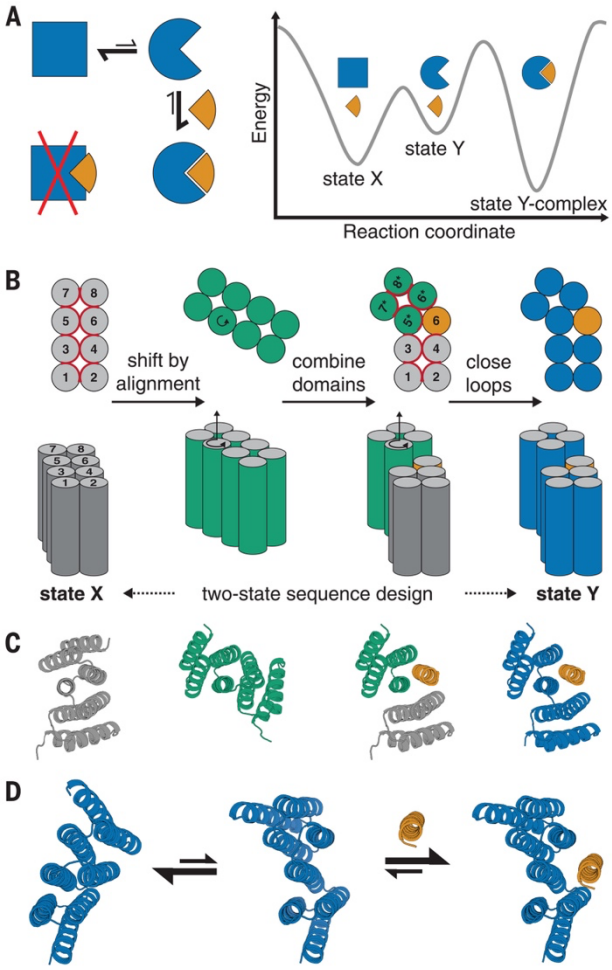

Fig. 1 | Strategy for designing proteins that can switch between different conformations. (**A**) (Left) reaction scheme for a protein (blue) that undergoes a conformational change and can bind an effector (orange) in one (circle) but not in the other conformational state (square). (Right) Energy landscape for the system shown on the left. (**B**) Schematic representation of the hinge design approach. Alpha-helices are represented as circles (top view, top) or cylinders (side view, bottom). (From left to right) A previously designed repeat protein (gray) serves as the first conformation of the hinge. To generate the second conformation, a copy of the repeat protein (green) is moved by shifted alignment along a pivot helix, causing a rotation (top and bottom, indicated by the circular arrow) and a translation along the helix axis (bottom). The first 4 helices of the original protein form domain 1 of the hinge, the last 4 helices of the rotated copy form domain 2, and an additional helix is copied over from the original protein to serve as an effector peptide (orange) that can bind to this second conformation of the hinge. The two domains of the hinge are connected into one continuous chain (blue) using fragment-based loop closure, and a single amino acid sequence is designed to be compatible with both conformations. (**C**) Design steps from (B) illustrated using cartoon representations of an exemplary design trajectory. (**D**) Exemplary design models of a designed hinge protein in state X (left), state Y (center), and in state Y bound to an effector peptide (right). Hinge is shown in blue, peptide in orange.

Design of rigid conformational change effectors

The most common failure mode for hinge proteins designed in this way was poor solution behavior of the effector peptide. Since these peptides are amphipathic with a strongly hydrophobic binding interface and also can adopt many conformations in isolation, they are prone to forming aggregates. To design effectors with improved solution behavior, I buttressed effector peptides with two additional helices to make three-helix bundle (3hb) proteins (Fig. 2), rigidifying the binding interface and reducing the space of possible aggregates that could form. The first 3hb effectors for hinge cs074 showed equivalent binding behavior to the original peptide effector cs074B, showing binding on size-exclusion chromatography (SEC) (Fig. 2, bottom left) and inducing the hinge conformational change according to Förster resonance energy transfer (FRET) (bottom middle) and double electron-electron resonance (DEER) (bottom right) spectroscopy experiments.

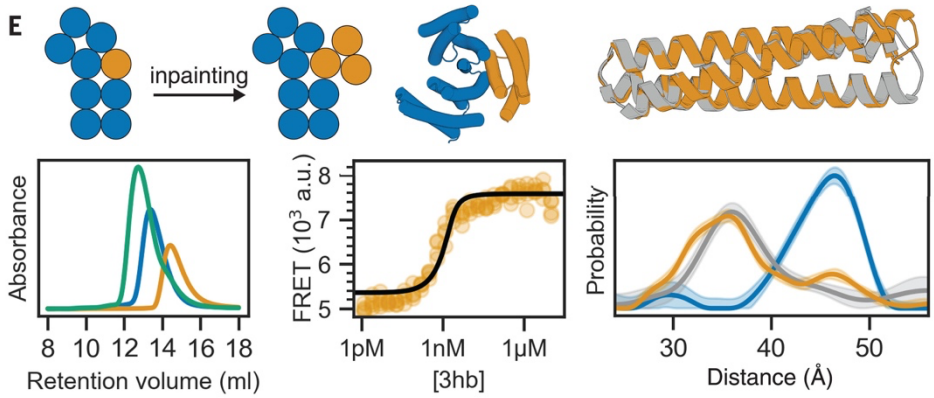

Fig. 2 | Design of structured protein effectors from peptide effectors. (Top from left to right) schematic representation of the inpainting procedure that adds two helices to the peptide effector yielding a three-helix bundle (3hb); cylindrical representation of 3hb_05 (orange) bound to hinge cs074 (blue); overlay of design model (orange) and crystal structure (gray) of 3hb_05. (Bottom from left to right) SEC traces for hinge cs074 (blue), 3hb_05 (orange), and a mixture of both (green); FRET-based titration of 2 nM extended labeled hinge cs074F and varying concentrations of 3hb_05 fitted with a standard binding isotherm (back line); distance distributions between spin labels covalently attached to cysteine side chains on cs074, obtained from DEER experiments with no effector (blue), excess 3hb_05 effector (orange), or excess peptide cs074B effector (gray) (shaded areas are 95% confidence intervals).

In many cases, rigidifying the effectors for other hinges improved solution behavior of the effector in isolation and also of the hinge·effector complex (Fig. 3). For hinge cs244, rigidifying the effector rescued the design, as it showed no clear binding with the original peptide effector (Fig. 3).

We studied the effects of effector rigidification on binding in more detail with hinge cs221. The rigidified effector binds significantly more strongly than the original peptide effector (Fig. 4, bottom right). This is partially due to a 5-fold increased on-rate (Fig. 4, bottom left), which likely arises from the effector being pre-folded, increasing the apparent concentration of binding-competent effector. Rigidification may also stabilize interfacial contacts, reducing the off-rate.

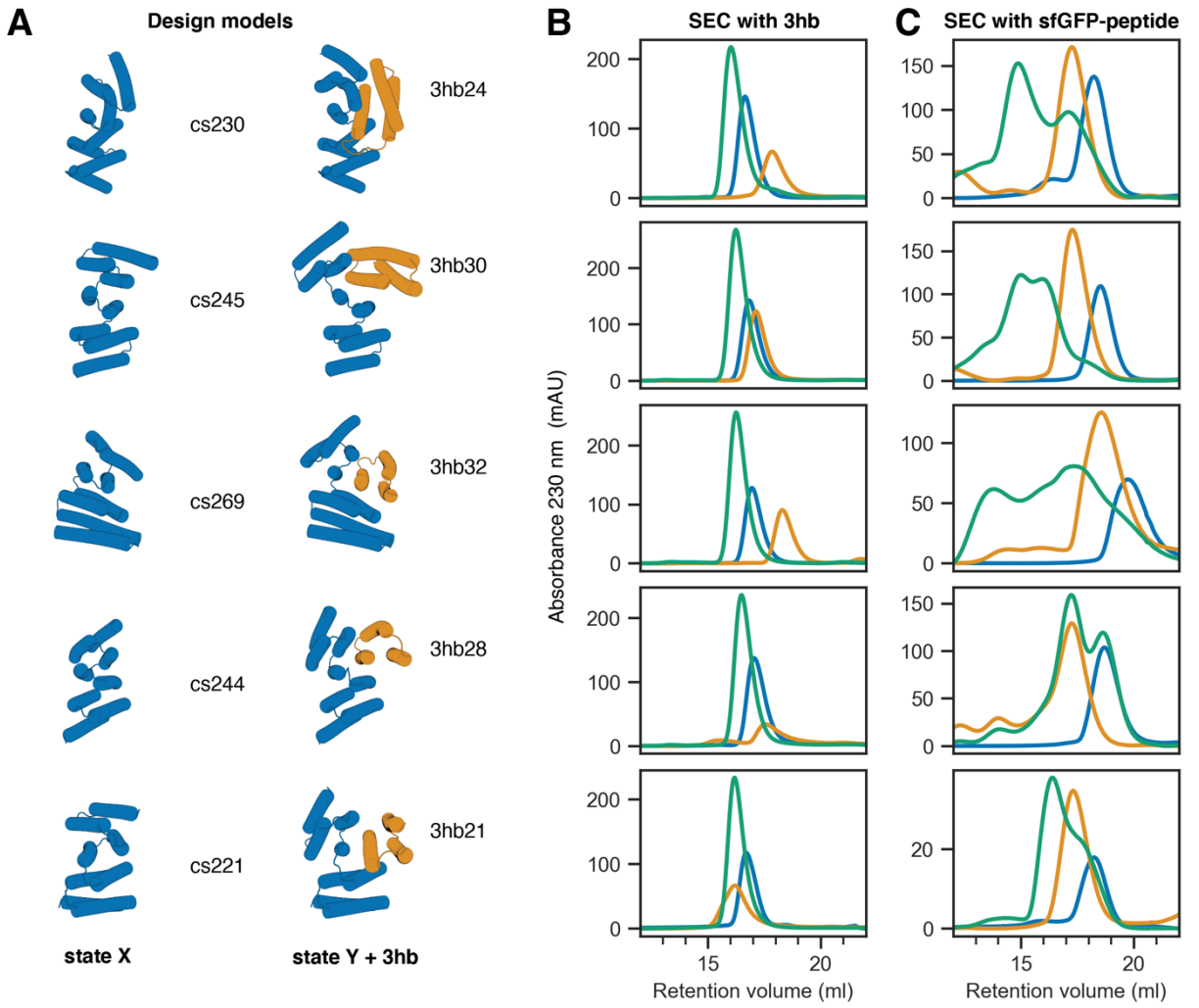

Fig. 3 | Additional three-helix bundle effectors. (**A**) Models of hinges (blue) in state X and in state Y bound to a three-helix bundle (3hb, orange). (**B**) SEC binding experiments of hinge (blue), 3hb (orange), and mixture of both (green) show clear monodisperse complex peaks. (**C**) SEC binding experiments of the same hinges with the original peptides fused to superfolder green fluorescent protein (sfGFP). For cs230, cs245, and cs269 the hinge-peptide complex shows higher-order peaks while the corresponding hinge-3hb peaks look much cleaner. For cs244, the original peptide showed no clear binding in the SEC experiment, while 3hb28 shows clear binding.

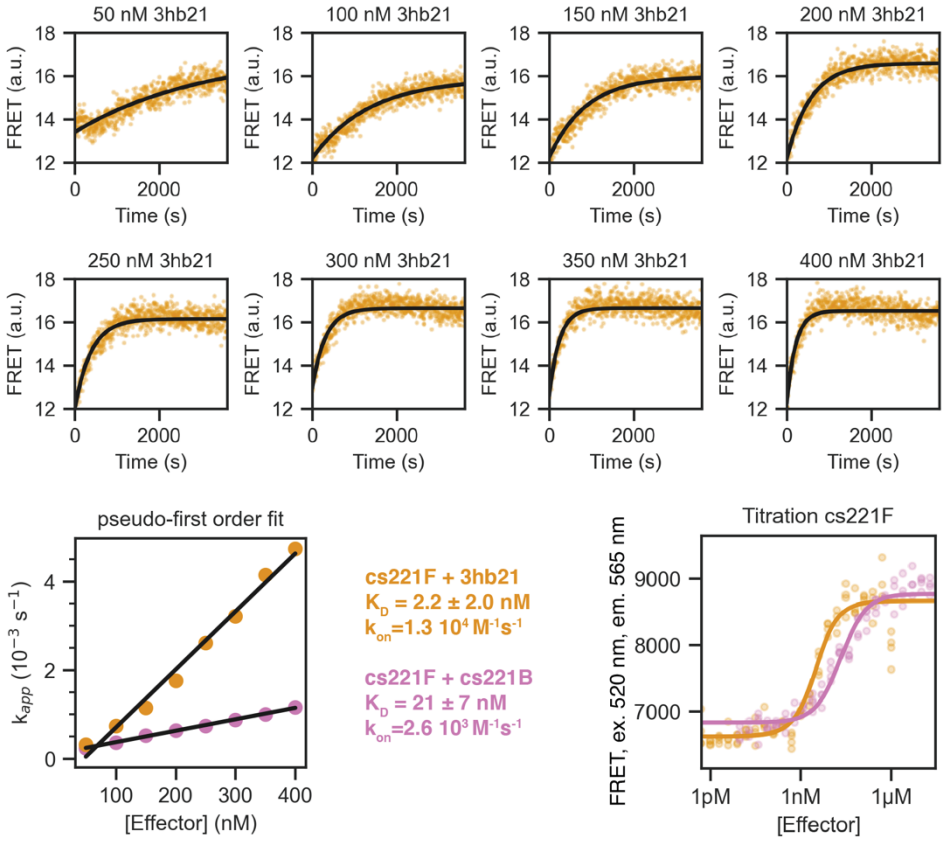

Fig. 4 | FRET-based quantitative analysis of the interaction between cs221F and 3hb21. Individual kinetic traces were obtained using a constant hinge concentration of 5 nM and varying 3hb concentrations as indicated by plot labels. Single exponential fits give apparent rate constants that increase linearly with the total 3hb concentration (orange points in pseudo-first order plot). The linear fit of k_{app} against 3hb concentration gives an observed on rate that is 5 times faster than the observed on rate of the original peptide (pink points). FRET titration of 2 nM hinge cs221F and varying concentrations of 3hb (orange) gives a KD below 2 nM which is at least 20 times stronger than the KD of the original peptide (pink).

Chapter II | Design of facilitated dissociation enables timing of cytokine signaling

Adapted from Broerman, A. J. *et al.* **Design of facilitated dissociation enables timing of cytokine signaling.** *Nature* (in press) (2025). https://doi.org/10.1038/s41586-025-09549-z

Abstract

Protein design has focused primarily on the design of ground states, ensuring they are sufficiently low energy to be highly populated[3]. Designing the kinetics and dynamics of a system requires, in addition, the design of excited states that are traversed in transitions from one low-lying state to another[8,9]. This is a challenging task because such states must be sufficiently strained to be poorly populated, but not so strained that they are not populated at all, and because protein design methods have generally focused on creating near-ideal structures[4,10–12]. Here we describe a general approach for designing systems that use an induced-fit power stroke[13] to generate a structurally frustrated[14] and strained excited state, allosterically driving protein complex dissociation. X-ray crystallography, double electron-electron resonance spectroscopy, and kinetic binding measurements demonstrate that incorporating excited states enables design of effector-induced increases in dissociation rates as high as 5,700-fold. We highlight the power of this approach by designing rapid biosensors, kinetically controlled circuits, and cytokine mimics that can be dissociated from their receptors within seconds, enabling dissection of the temporal dynamics of IL-2 signaling.

Main

Protein-protein interactions orchestrate much of biological function. High affinity interactions enable protein circuits to respond to low concentrations of stimuli and to potently act on targets; fast exchange enables them to respond quickly to changes in stimuli. These two properties usually cannot simultaneously be achieved in binary interactions because they depend on the interaction off-rate in opposite ways: high affinity usually requires slow dissociation (low off-rate) whereas rapid exchange requires fast dissociation (high off-rate) (Supplementary Fig. 1). Several natural systems exhibit “facilitated dissociation”[15–25] in which an effector (E) can bind to a target·host (TH) complex to form an excited ternary complex (THE)[25–31] from which the target dissociates quickly (Fig. 5a,b,c). In such a system, the target can bind tightly to the host yet can also be rapidly released by adding the effector[32]. In engineered DNA systems, the kinetic control afforded by an analogous phenomenon (toehold-mediated strand displacement) has enabled the construction of many complex functions[33,34], but DNA systems have limited utility for directly interfacing with biology. Protein binding/unbinding can be readily coupled to biological processes, but there has been no general approach to design kinetic control over protein interactions.

We set out to design protein systems that undergo facilitated dissociation. Given an interacting protein binder·target pair, we reasoned that we could construct host proteins with controllable dissociation kinetics by fusing an effector-responsive conformational switch to the binder such that when the effector is not bound, the target can bind normally, but in the alternate effector-bound conformation, the switch clashes with the target, leading to strain in the target·host·effector ternary complex which resolves when the target dissociates[35] (Fig. 5d,e; nomenclature detailed in Supplementary Note 1). This would allosterically couple the effector and target, and facilitated dissociation could proceed through the strained ternary complex intermediate faster than spontaneous dissociation of the target in mutually exclusive competition (Fig. 5c). Critically, the energy of this ternary intermediate must be neither too high (otherwise the facilitated dissociation pathway would not be faster) nor too low (otherwise the target would not dissociate) (Fig. 5b). To set the ternary intermediate energy within this optimal range (Supplementary Fig. 2), we reasoned that we could control the level of strain in the ternary complex by varying the geometry of the switch-binder fusion. To effectively access this strained state, we reasoned that binding the effector should rapidly drive the conformational change against the resisting force associated with generating strain. Such a "driven" motion would be akin to the power strokes of motor proteins: a large conformational change that is both thermodynamically and kinetically favored (a low-barrier descent down a steep energy gradient)[13,36]. Compared to the mechanism of direct steric overlap between target and effector, as in many existing facilitated dissociation systems[22–25,31,37], this allosteric mechanism if successful should be quite modular: such a force-generating switch could be fused to almost any binder to enable facilitated dissociation of its target.

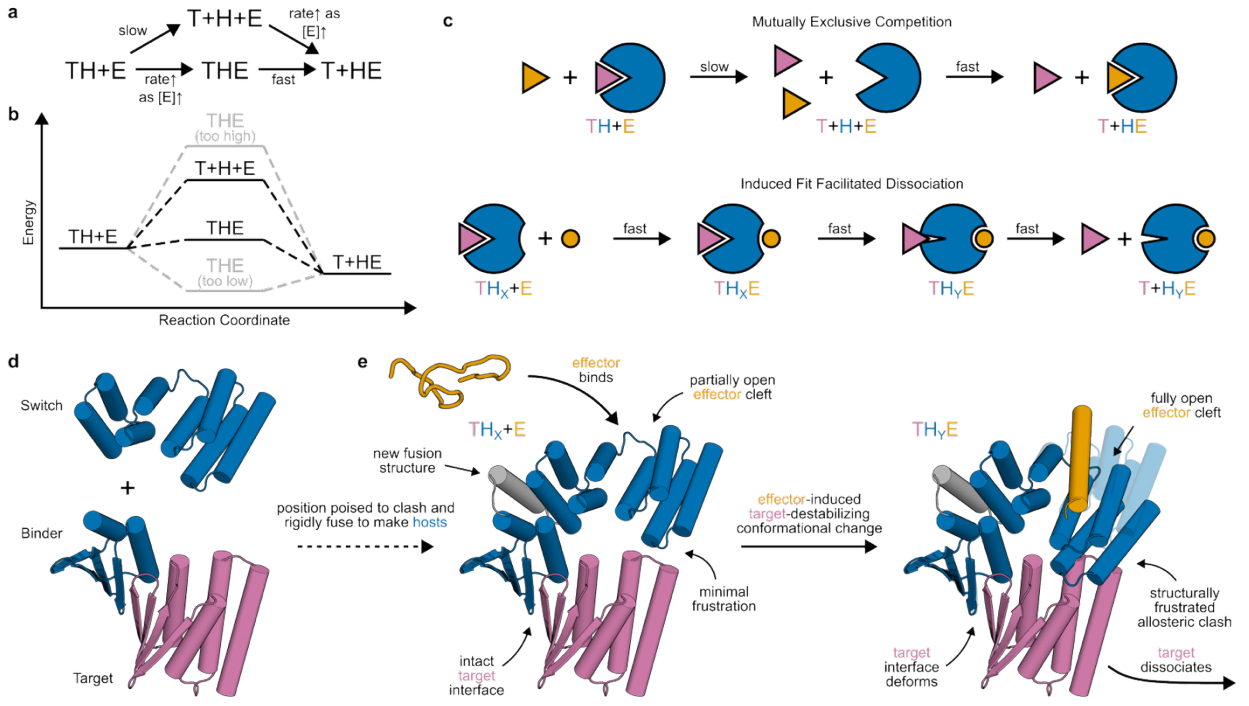

Fig. 5 | Strategy for designing proteins that reconfigure through facilitated dissociation. a, b, c, A high affinity interaction can rapidly exchange through facilitated dissociation (lower pathways), but not

through mutually exclusive competition (upper pathways). **a**, Reaction diagram. **b**, Energy diagram. **c**, Schematic of induced-fit facilitated dissociation (bottom) compared to slow mutually exclusive competition (top). The host protein (H, subscripted by conformational state X or Y) is shown in blue, the target (T) in pink, and the effector (E) in orange. **d**, Structural models of starting components (effector-responsive switch and arbitrary binder·target pair) combined to construct facilitated dissociation systems. **e**, Structural models of example proteins designed to undergo a facilitated dissociation process starting from a tightly interacting state X (left) through a structurally frustrated ternary intermediate in state Y (right, solid). State X (transparent) is included to show the conformational change.

We began by using a previously designed effector-responsive conformational switch (hinge protein cs221[7]) to test the concept of allosteric coupling via switching steric clashes between the host and target. This switch can undergo a rigid-body hinge motion to transition from a closed state (X) to an open state (Y), and in the open state Y can bind an effector peptide quite tightly (k_{off} = 5e–6 s^{-1}). For a model binder·target interaction, we chose a designed heterodimer pair (LHD101[38], modified as described in Supplementary Fig. 3) with slow enough dissociation (k_{off} = 9e–5 s^{-1}) that we could easily measure significant effector-induced acceleration of target dissociation, but not slower than the effector dissociation so that the target would be more likely than the effector to dissociate from the ternary complex. To allosterically couple binding the effector to dissociation of the target, we designed structured fusions of the hinge switch and binder such that when the switch is in state X, the target can bind, but when in the effector-bound state Y, it would strongly clash (Fig. 5d,e; Supplementary Fig. 4a,b; methods). We obtained synthetic genes encoding 12 designs, expressed and purified the proteins from E. coli, and found that the best ("allosteric switch 0" AS0) showed slow and significantly reduced effector association in the presence of the target (Supplementary Fig. 5d), indicating the desired allosteric coupling but also the need for designs with a faster, driven pathway for effector binding against the target.

In these first designs, since the effector binding cleft is closed in state X, the hinge switch must first transition to the open state Y before the effector can bind (a conformational selection mechanism). Since state Y clashes with the target, this conformational change is slow when the target is bound, limiting the rate of effector association and the overall rate of facilitated dissociation (Supplementary Fig. 4c). This slow step could be bypassed if the effector could instead first bind to state X and accelerate the transition to state Y. An induced-fit mechanism could provide the driving force: an intrinsically disordered effector could weakly engage with state X, and fold and make more extensive interactions in the strained ternary complex in state Y[39], driving the transition in a power stroke–like motion[40,41].

Such a mechanism would require new switches that, in state X and throughout the conformational transition, retain an open effector binding cleft where a flexible effector could associate (Fig. 5e, Supplementary Fig. 4d). Starting from AS0, we constructed a new state X by shifting the two domains from their state Y positions relative to each other (by one heptad along the helix of domain 1 that contacts domain 2), building a new loop between the domains, and optimizing single sequences that could adopt both this new state X and the original effector-bound state Y (Supplementary Fig. 4e, methods). This approach maintains the open cleft in state

X by introducing minimal rotation from state Y and simplifies the multi-state sequence design challenge by minimizing the local structural differences between the two states. Transition between conformational states occurs by a register shift throughout which the cleft remains open and binds the effector (Supplementary Fig. 4f). Since these new hosts retain the state Y backbone validated to clash with the target in AS0, we should observe allosteric coupling if the switch works as designed (Fig. 5e).

We obtained synthetic genes encoding 10 such designs, and found that 4 tightly bound the effector (K_D < 1 nM, Supplementary Fig. 6d). To measure facilitated dissociation kinetics, we used surface plasmon resonance (SPR): with the target affixed to the SPR surface, we incubated with host, then measured target:host dissociation under flow of various concentrations of effector. For these four designs, the target dissociates slowly in the absence of the effector; addition of effector dramatically increases the rate of dissociation (Fig. 6a, Supplementary Fig. 7), but minimally affects the target off-rate from a control static binder fusion lacking an effector binding site (Supplementary Fig. 7).

To probe the mechanism of facilitated dissociation (Fig 2b), we focused on AS1, the design with the tightest effector binding ($K_{D,H:E} \approx 10$ pM). We directly measured the rate constant of target dissociation from the strained ternary complex ($k_{off,T:HE}$) by flowing pre-incubated host·effector complex at high concentration to form the strained ternary complex with the target on the SPR surface, then tracking target:host dissociation under continued flow of the effector (Fig. 6e, Supplementary Fig. 7; methods). In the full facilitated dissociation process, as the concentration of added effector increases, the rate constant of facilitated target dissociation approaches $k_{off,T:HE}$ (Fig. 6g, Supplementary Fig. 7), strongly suggesting that the ternary complex is an intermediate in the facilitated dissociation process (Fig. 6b, lower pathways).

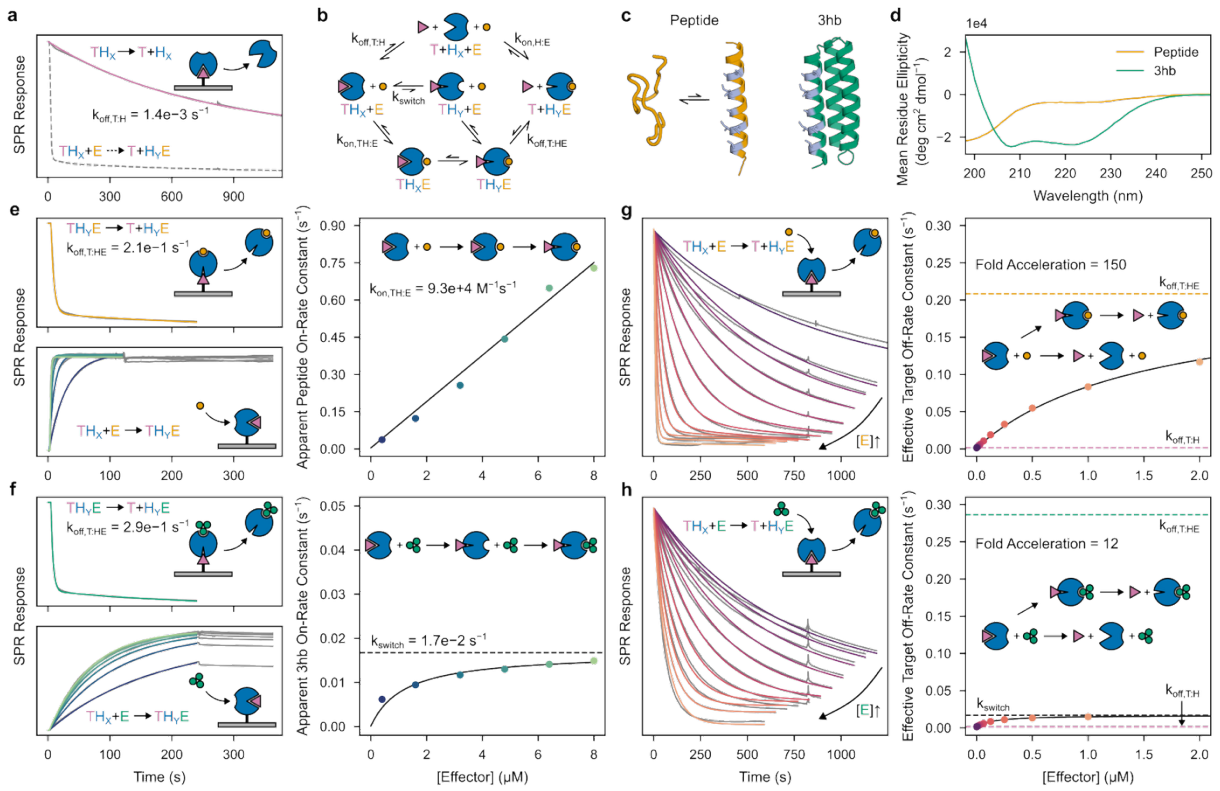

Fig. 6 | Kinetic characterization of facilitated dissociation in AS1. a, Slow dissociation of the target from the host in the absence of effector (solid) and fast dissociation in the presence of 2 μM effector (dashed) assessed by SPR. Slow dissociation data (solid gray) fit with a double exponential (pink). **b**, Kinetic model describing pathways of competition: (top) mutually exclusive competition, (middle) facilitated dissociation with effector binding rate-limited by conformational selection, (bottom) facilitated dissociation with induced-fit effector binding. The k labels are rate constants. **c**, Cartoon representations of the peptide (left) and 3hb (right) effectors; interface residues shown in gray. **d**, Circular dichroism (CD) spectra of the peptide and 3hb effectors. **e** and **f**, Kinetic characterization of the formation and breakage of the ternary complex intermediate with the peptide (e) and 3hb (f) effectors. (Top left) fast dissociation of the target from the ternary complex, data (gray) fit with double exponentials (orange/green); (bottom left) effector association to form the ternary complex and extremely slow subsequent dissociation, data (gray) fit with single exponentials (colors) in the association phase; (right) apparent effector on-rate constant plotted against effector concentration (circles) and a linear (e) or hyperbolic (f) fit. k_{switch} is the saturating value of the hyperbolic fit. **g** and **h**, Kinetic characterization of the full facilitated dissociation pathway with the peptide (g) and 3hb (h) effectors. (Left) effector concentration–dependent dissociation of the target, data (gray) fit (colors) as described in methods; (right) rate constant of facilitated target dissociation plotted against effector concentration (circles) and fit with a hyperbolic equation (black line). In **a** and the left plots of **e**–**h**, schematics show the arrangement of proteins relative to the SPR chip (gray). In the right plots of **e**–**h**, schematics show the mechanism that can be inferred from the data.

To further probe the mechanism of forming the strained ternary complex, we characterized facilitated dissociation with two different effectors: the peptide and a three-helix bundle "3hb" (3hb21[7]) (Fig. 6c). The two effectors make nearly identical interactions with AS1, but when unbound, the peptide is disordered whereas the 3hb is structured (Fig. 6d). With AS1 affixed to

the SPR surface, we measured the rate of effector association to form the strained ternary complex by first saturating AS1 with target, then flowing varying concentrations of effector mixed with constant excess target (to ensure target remains bound after effector association). The apparent on-rate for binding to the target·AS1 complex increases linearly with concentration for the peptide (Fig. 6e) but hyperbolically for the 3hb, saturating at the rate of a concentration-independent step (Fig. 6f). Notably, with the 3hb, the rate of facilitated target dissociation saturates at this same value (Fig. 6h). The simplest explanation of these results is that the rigid 3hb can only bind to the fully open state Y of AS1 and that the $TH_X \rightarrow TH_Y$ conformational change is slow (due to partial blocking by the bound target), so it becomes rate limiting for both the association with the target·AS1 complex and the overall facilitated dissociation process (Fig. 6b, middle pathway). In contrast to the 3hb, peptide effector binding (Fig. 6e) and resulting target destabilization (Fig. 6g) both can occur more rapidly than the $TH_X \rightarrow TH_Y$ conformational change, suggesting that the more flexible peptide effector can bind to AS1 in state X to accelerate this conformational change through an induced-fit mechanism (Fig. 6b, bottom pathway)[17,39,42].

We used x-ray crystallography to structurally characterize multiple states of our designed systems. For both the AS1 and AS5 systems, the crystal structures of the hosts alone (Fig. 7a, Extended Data Fig. 1a) and of the host·effector complexes (Fig. 7b, Extended Data Fig. 1b) closely match the design models (maximum 1.3 Å Cα RMSD). The unbound structures show an open hydrophobic cleft in the new designed state X poised to bind the effector, and the effector-bound structures show that binding the effector causes the two switch domains to register shift into the designed state Y. The structures also show sequence features present in almost all designs (insets in Fig. 7a,b and Extended Data Fig. 1a,b): a positively charged residue (K60) holds the cleft open in state X and moves to interact with the negative dipole of the effector helix in state Y, and the interface between domains in the designed one-heptad register shift contains sequence motifs repeated a heptad apart (on the C-terminal domain, L84 in state X and L91 in state Y pack against the same location on the N-terminal domain).

We solved structures of AS1 bound to the target from two different crystals, each containing two copies of the complex. Both copies in one crystal and one copy in the other closely match the state X design model with slight fluctuation in the target binding conformation (Fig. 7c, top; Extended Data Fig. 1d), showing that the target binds as designed to clash with the switch in state Y. In the remaining copy, AS1 adopts a different conformation in which the effector-binding cleft has collapsed to resemble the closed state X of the original hinge switch (Fig. 7c, bottom). The new state X of AS1 still slightly clashes with the target (Extended Data Fig. 1c), likely causing this dynamic target binding and cleft collapse.

We next sought to determine how the target·host·effector ternary complex deforms to resolve the designed clash. At the concentrations of the components used in the above experiments, the AS1 ternary complex is an only transiently populated excited state, but at high concentrations it becomes the dominant state ($K_{D,T:HE}$ = 200 nM, Supplementary Fig. 9). This enabled us to solve structures of AS1 in the ternary complex intermediate with both target and effector. In structures from two different crystals, the switch region closely matches the state Y design model while the rest of the structure strains to resolve the structural frustration from simultaneously binding the

target and occupying state Y (Fig. 7d). This strain distributes across multiple locations in the structure: the binder fusion bends, the portion of the target that directly clashes with the switch becomes disordered, and the target twists at its interface, disrupting the interfacial hydrophobic packing (Fig. 7e, top) and shearing the interfacial strand pairing (Fig. 7e, bottom).

We explored the dynamics within the AS1 ternary complex using molecular dynamics (MD) simulations and double electron-electron resonance (DEER) spectroscopy to measure pairwise distance distributions between residues on opposing sides of the conformational switch. For the three low-energy states, the AS1 alone, target·AS1 complex, and AS1·effector complex DEER distance distributions are consistent with the distances between spin labels simulated based on the corresponding crystal structures (Extended Data Fig. 2). For the higher-energy ternary complex, the DEER distance distribution contained two peaks: one aligned with the distances simulated from the ternary complex crystal structure and from two MD trajectories started from the AlphaFold2 (AF2) prediction of the ternary complex, and the other aligned with the distance simulated from a third trajectory (Extended Data Fig. 3). Thus, to resolve strain, the ternary complex can likely adopt multiple conformations with varying amounts of switch deformation, target deformation, and unfolding of the clashing region of the target (Extended Data Fig. 3).

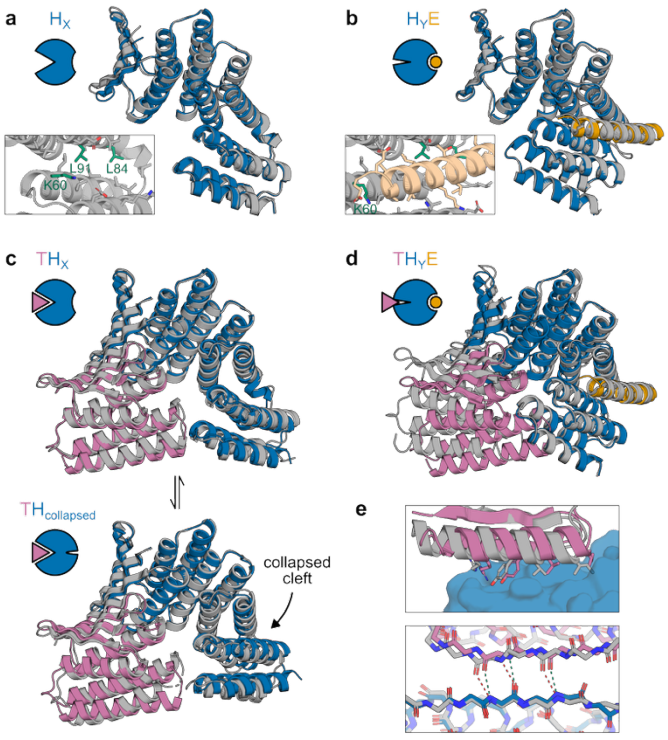

Fig. 7 | Structural characterization of AS1. a, Crystal structure of AS1 alone (gray) overlaid with the design model of AS1 in state X (blue). Inset shows a detailed view of side chains in the partially open effector-binding cleft. **b**, Cocrystal structure of AS1 and peptide effector (gray) overlaid with the design model of the AS1·effector complex in state Y (blue/orange). Inset shows the same view as in (a). **c**, (Top) cocrystal structure of AS1 (with intact cleft) and target (gray) overlaid with the design model of the target·AS1 complex in state X (blue/pink). (Bottom) cocrystal structure of AS1 (with collapsed cleft) and target (gray) overlaid with the design model of the target·AS0 complex (blue/pink) whose state X resembles this collapsed state. **d**, Cocrystal structure of AS1 (with hydrophobic surface mutations), target, and peptide effector (gray) aligned at the switch region with the design models of the target (pink) and AS1·effector complex in state Y (blue/orange) showing the designed clash. **e**, (Top) detailed view of the target interface side chains in the ternary complex (gray) and the target·AS1 complex (pink) interacting with AS1 (blue). (Bottom) detailed view of the backbone hydrogen bonding in the interfacial strand pairing. The target·AS1 complex (pink/blue) hydrogen bonds (green) are less strained than the ternary complex (gray) hydrogen bonds (red).

Modulation of dissociation acceleration

We next explored the factors contributing to the dissociation kinetics, seeking to maximize the dissociation rate enhancement by 1) reducing the base rate of target dissociation and 2) increasing the rate of facilitated dissociation. For (1), the target dissociates 20-fold faster from AS1 than from an unhindered binder fusion (Supplementary Fig. 7) likely due to minor strain in the target·AS1 complex (Extended Data Fig. 1c). For (2), with AS1, effector association can occur at least 5 times faster than target dissociation from the ternary complex, and hence moderately increasing the energy of the ternary complex could accelerate the target dissociation step without making effector association rate limiting, increasing the overall rate of facilitated dissociation. Assuming a simple spring model of the ternary complex, this could be achieved by deforming with a greater magnitude or in a direction of higher stiffness (Supplementary Fig. 10a).

We sought to maximize strain energy in the ternary complex by modulating the magnitude and direction of the deformation required to resolve the designed clash (Fig. 8a). Avoiding any clash in state X while maintaining a strong clash in state Y, we sampled a variety of target+binder positions relative to the switch from AS1, rebuilt fusions between the switch and the newly located binder, and selected variants that AlphaFold2 (AF2) predicted had substantial deformations spanning a variety of directions (AF2 predictions of the strained AS1 ternary complex were within 1.0 Å Cα RMSD of the target·AS1·effector crystal structure). These changes to the fusion region, though distant from both binding sites, caused dramatic variation in the kinetics of target dissociation and their modulation by the effector (Supplementary Fig. 11). Most of these variants showed reduced target off-rates (compared to AS1) in the absence of effector which increased in the presence of effector (Supplementary Fig. 11, Supplementary Table 1), and for the fastest variant (AS117), adding effector accelerated target dissociation by 2400-fold, reaching a rate exceeding that of original AS1 (Fig. 8b).

Surprisingly, the AS1 variants with the largest deformations in the strained ternary complex do not have the fastest dissociation rates: for example the predicted deformation magnitude for variant AS114 is double that of the fastest variant AS117 (Supplementary Fig. 10b,c), yet its accelerated target dissociation is 40-fold slower (Fig. 8b). This could reflect the strain being so great in state Y that the AS114 ternary complex instead occupies state X, but DEER measurements of the AS114 ternary complex confirm that it primarily occupies state Y (Extended Data Fig. 2c). Rather, designs like AS1 and AS117 must deform in directions of higher stiffness than the slower but more highly deforming variants like AS114. Due to differences in the relative switch and binder positions, the binder:target interface in the predicted ternary complex experiences shear strain in designs like AS1 and AS117 but bending strain in designs like AS114 (Supplementary Fig. 10b). Beta sheets are stiffest against shear[43,44], so deforming in a direction that shears the binder:target interface likely leads to the higher-energy ternary complexes seen in designs like AS1 and AS117. Thus, the global strain energy of the ternary complex depends on both the magnitude and direction of the deformation (Supplementary Fig. 10e).

To explore whether these designs vary not only the global strain energy of the ternary complex but also the distribution of this strain throughout the structure, we used a fluorescence polarization competition assay to measure target-induced acceleration of effector dissociation (the reverse direction of facilitated dissociation) (Fig. 8b, Supplementary Fig. 12). Designs like

AS114 showed approximately equal fold acceleration in the forward and reverse directions, whereas designs like AS1 and AS117 showed 5–15-fold greater acceleration in the forward direction (Extended Data Fig. 4). This suggests that in these designs, much of the strain energy is directed towards shearing the target interface, promoting target dissociation over effector dissociation, whereas other deformation directions more uniformly distribute strain across the complex. This is supported by the crystal structures of AS1, in which the binder:target interface deforms from its binary complex conformation much more than the switch:effector interface (1.4 Å vs 0.5 Å Cα RMSD) (Extended Data Fig. 4d).

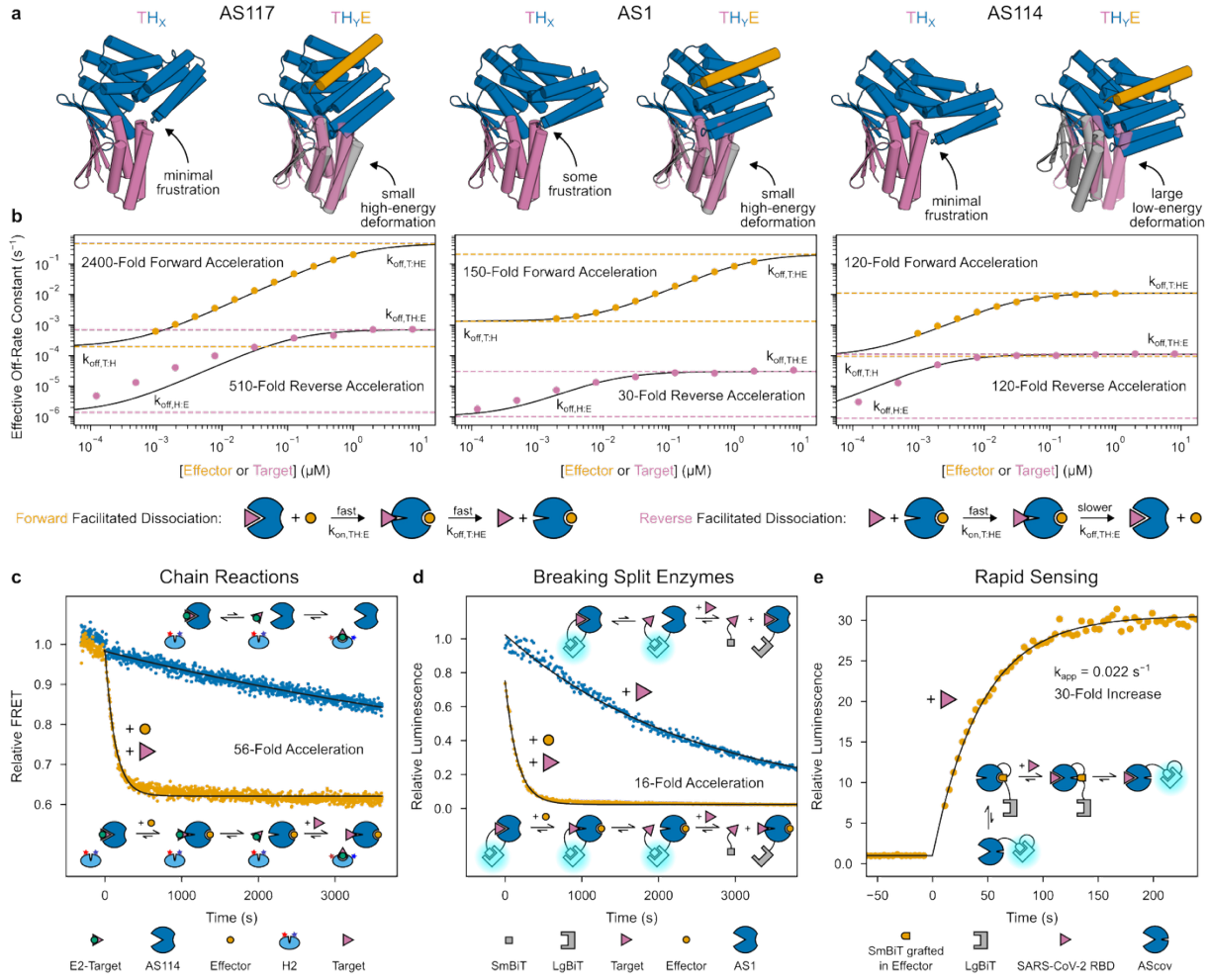

Fig. 8 | Modulation and applications of facilitated dissociation. a,**b**, Comparison of three representative designs with different facilitated dissociation kinetics. **a**, (For each design) (left) model of host in state X (blue) aligned to the target (pink) to show any clash influencing the target off-rate in the absence of effector; (right) model of host·effector complex in state Y (blue and orange) aligned to the target (pink) to show the designed clash, and (gray) AF2 prediction of the target position relative to the switch in the ternary complex to show how the clash resolves through global strain. **b**, Forward and reverse facilitated dissociation rates: target off-rate constants vs effector concentration (orange circles) and effector off-rate constants vs target concentration (pink circles) fit with hyperbolics (black lines). Cartoons illustrate the forward and reverse facilitated dissociation pathways. **c**, FRET time courses showing slow transfer of a kinetically trapped

effector (blue, upper schematic) and accelerated transfer through facilitated dissociation (orange, lower schematic). **d**, Luminescence time courses showing breakage of a reversible split luciferase through slow direct competition (blue, upper schematic) and faster facilitated dissociation (orange, lower schematic). **e**, Luminescence time course (orange) showing rapid sensing of SARS-CoV-2 through facilitated dissociation (schematic). **c**–**e**, Data fit with single exponentials (black lines).

Applications of facilitated dissociation

We next set out to use facilitated dissociation to construct protein systems with kinetic behaviors previously inaccessible to design. First, inspired by toehold-mediated strand displacement in DNA[33], we sought to create a kinetically trapped system that, upon stimulation, quickly reconfigures through a chain reaction. To investigate this, we fused the effector peptide (E2) for a second reporter hinge (H2) to the target such that E2 is occluded when this fusion (E2-target) is bound to a host (Extended Data Fig. 5). As intended, release of E2-target from AS114 and subsequent switching of H2 is slow, but is dramatically accelerated upon adding original effector which accelerates E2-target dissociation (we include excess original target to prevent E2-target rebinding[45]; Fig. 8c, Extended Data Fig. 5). In principle, multiple orthogonal hosts could be constructed and chained together through such target-effector fusions.

Second, we reasoned our designs could complement split protein systems with high affinity and enable them to be rapidly switched off. To test this, we tagged AS1 and the target with NanoBiT split luciferase fragments, LgBiT and SmBiT[46]. When combined, these components exhibit high luciferase activity which disappears much more rapidly upon addition of effector and excess untagged target than upon addition of excess untagged target alone (Fig. 8d).

Third, in thermodynamically controlled biosensors designed previously which operate through a conformational selection mechanism, there is a tradeoff between dynamic range and response time (reducing background by lowering the energy of the “off” state generally slows interconversion with the “on” state)[47,48]. We reasoned that sensors based on facilitated dissociation could be limited by the rate of target association rather than internal conformational switching, and found that by caging the SmBiT peptide within the effector bound to a host, facilitated dissociation (in the reverse direction compared to previously) upon binding the target rapidly uncaged the SmBiT to enable luciferase reconstitution (methods). Using this strategy together with a designed SARS-CoV-2 RBD binder (LCB1[49]), we generated 16 “AScov” sensor designs in which the RBD clashes with the switch in state Y but not in state X. Upon addition of SARS-CoV-2 RBD, the best sensor shows a 30-fold increase in luciferase activity with a half-time of 30 seconds (Fig. 8e, Extended Data Fig. 6)—70 times faster than a previously designed LOCKR-based SARS-CoV-2 sensor which relies on conformational selection[47]. Thus, using this platform, a binder to almost any target can be turned into a single-component sensor that is sufficiently fast that in most practical applications, its response time will be limited by target association rather than a slow conformational change.

Rapid modulation of IL-2 signaling

Finally, we investigated whether facilitated dissociation could be used to control cellular processes with high temporal resolution. In cellular signaling, the residence time of the ligand stimulating the receptor is thought to modulate the signaling and cellular responses[50–52]. The central immune cytokine interleukin-2 (IL-2) activates the IL-2 receptor (IL-2Rβγc) by inducing heterodimerization of chains β and γc[53]. The resulting complexes dissociate or degrade on timescales of hours[54,55], so controlling the temporal dynamics of IL-2 signaling is difficult: there is no off-switch (Fig. 9a).

We set out to construct a switchable IL-2 mimic that enables seconds-timescale control over the lifetime of the IL-2Rβγc complex (Fig. 9b). Neo-2, a previously designed IL-2 mimic, tightly binds IL-2Rβγc to elicit downstream signaling[56]. Sampling a variety of γc positions relative to the switch from AS1, we rigidly fused Neo-2 to the switch such that in state X, γc can bind, but in the effector-bound state Y, it would strongly clash (Fig. 9c). We identified several designs for which binding the effector dramatically accelerates dissociation of γc from the active signaling complex (Supplementary Fig. 13). For one of these, ASNeo2, binding the effector induces a 1500-fold increase in γc off-rate (Fig. 9d).

For downstream applications, it would be desirable to have versions of ASNeo2 that 1) rapidly dissociate from IL-2Rβ after γc dissociates, 2) do not release active cytokine in the event of limited proteolysis, and 3) are effective at lower effector concentrations. For (1), we found that mutation H198E increases the ASNeo2:IL-2Rβ off-rate by 5-fold (Supplementary Fig. 16a). For (2), splitting the Neo-2 across the switch would ensure that activity is lost if the switch regulating it degrades, and for (3), ASNeo2 binds the effector considerably slower than AS1 (Supplementary Fig. 16b), suggesting the effector-binding cleft is predominantly collapsed prior to effector binding and requiring higher effector concentrations than AS1 for a rapid response (Fig. 8a, 5d). To address both (2) and (3), we used a split Neo-2 (Neo2A-Neo2B pair[57]) which minimally signals unless reconstituted, repositioned the switch relative to split Neo-2 to reduce strain in state $\beta\gamma_c H_X$, then rigidly fused Neo2B to the switch C-terminus and connected Neo2A to the switch N-terminus with a flexible linker (Extended Data Fig. 8a). For several of these variants (especially ASNeo2_cp03), dissociation of γc from the active signaling complex dramatically accelerates under lower effector concentrations than required for the original design, suggesting that the effector-binding cleft is more intact (Extended Data Fig. 8d). γc dissociation from ASNeo2_cp08 is accelerated by 5700-fold, the highest fold change of all our designed systems (Extended Data Fig. 8d).

To explore the switching capability of ASNeo2 in a physiological context, we quantified dimerization of labeled IL-2Rβ and γc in the plasma membrane of live cells by single-molecule fluorescence microscopy. Dual-color co-tracking and mobility analyses confirmed that ASNeo2 efficiently dimerizes IL-2Rβ and γc, and that adding the effector rapidly and completely reverses this association even at elevated excess of γc (Fig. 9e,f; Extended Data Fig. 7c–i). By double-labeling ASNeo2 on opposite sides, we could observe the effector-induced intramolecular conformational change at the plasma membrane using single-molecule Förster resonance energy transfer (smFRET) (Extended Data Fig. 7j,k). ASNeo2 activates signaling in human NK (YT) cells, and its activity is greatly reduced in the presence of the effector (Fig. 9g). Upon adding the

effector, STAT5 phosphorylation immediately stops accumulating and gradually decreases to a low level (Fig. 9h). The effector blocks ASNeo2 activity nearly as effectively as Ruxolitinib, a JAK1 inhibitor.

To explore how the duration of IL-2 signaling affects the downstream cellular response, we stimulated primary human T cells with ASNeo2 and induced dissociation at different time points. Whereas sustained stimulation was required for proliferation[58] (Fig. 9i), protection from apoptosis was evident after short transient stimulation: cells treated with ASNeo2 followed by effector 5 minutes later survived 3 days later at double the rate of an unstimulated control (Fig. 9j), despite suppression of most downstream IL-2 target proteins (Extended Data Fig. 9e). This likely reflects reduced caspase-3 activity and increased *BCL2* expression after transient stimulation (Fig. 9k, Extended Data Fig. 9g).

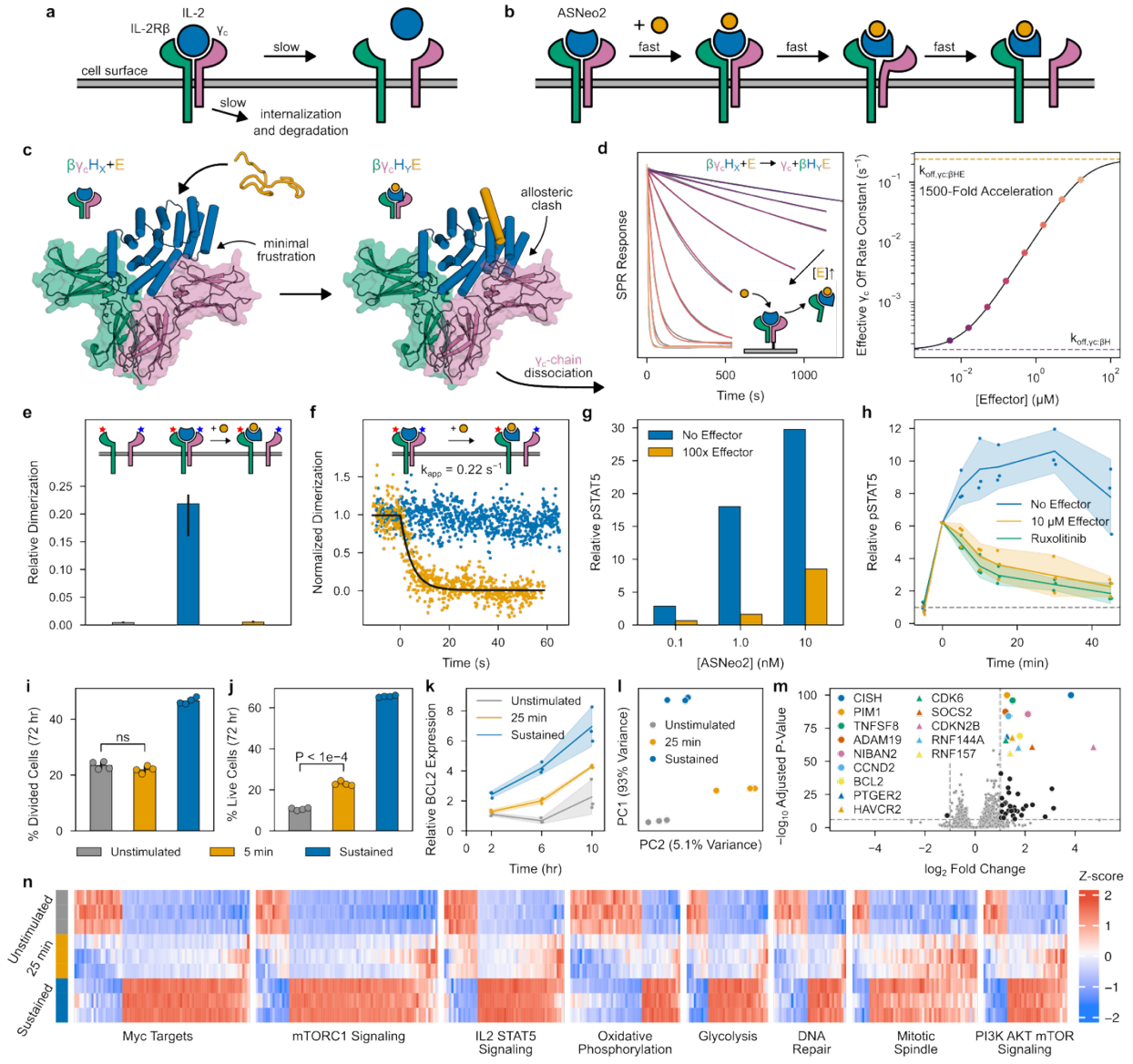

Fig. 9 | Characterization of a rapidly switchable IL-2 mimic. a, Natural pathways for terminating IL-2 signaling are slow. **b**, Through facilitated dissociation, signaling could be rapidly terminated. **c**, Model of ASNeo2 binding IL-2Rβγ_c to activate signaling (left), which quickly terminates after adding effector (right). **d**, (Left) accelerated dissociation of γ_c, data (gray) fit (colors) as described in methods. (Right) γ_c dissociation rate constant vs effector concentration (circles) fit with a hyperbolic (black line). **e**, Relative IL-2Rβ/γ_c dimerization on the cell surface initially (gray, n=37), after adding ASNeo2 (blue, n=32), and after that adding effector (orange, n=33). **f**, Time courses of IL-2Rβ/γ_c dimerization after pre-stimulation with ASNeo2 then adding nothing (blue) or effector (orange), fit with an exponential (black) yielding the rate constant k_{app}. **g**, Dose-response of STAT5 phosphorylation from stimulation with ASNeo2 alone (blue) or with effector (orange) (n=1). **h**, Time courses of STAT5 phosphorylation after stimulation with ASNeo2 for 5 minutes then adding nothing (blue), effector (orange), or ruxolitinib (green) (n=3). **i**–**n**, Human T cells were stimulated with ASNeo2 or left untreated as a control (gray). Signaling was sustained (blue) or terminated with effector (orange) after the indicated duration. **i**, **j**, Cell division (i, by CFSE staining) and survival (j) 3 days after stimulation (n=4); statistics from ANOVA with two-sided Tukey's post-test. **k**, Time courses of BCL2 expression (by qPCR, n=3). **l**–**n**, RNA-seq analysis 6 hours after stimulation (n=3). **l**, Principal component analysis. **m**, Changes in gene expression after transient stimulation. Points denote differentially expressed genes; the most significant are labeled. **n**, Heatmap of differentially expressed genes from hallmark gene sets with high gene correlation. **e**, **h**–**k**, Lines/bars represent medians (e) or means (h–k); error bars/shaded areas represent 95% confidence intervals; n refers to biologically independent samples.

To further investigate the dependence of IL-2 signaling on the lifetime of the signaling complexes, we compared RNA-seq data from T cells treated with ASNeo2 transiently, continuously, or not at all (Fig. 9l–n, Supplementary Fig. 14). Transient stimulation (through incubation with ASNeo2 followed by effector induced dissociation) upregulated genes involved in suppressing apoptosis (*BCL2*, *NIBAN2*, *RNF157*), cell cycle regulation (*CDKN2B*, *CDK6*, *CCND2*, *PIM1*), cytokine signaling suppression (*SOCS2*, *CISH*), and immune activation (*TNFSF8*, *HAVCR2*, *PTGER2*) (Fig. 9m). Upon activation, T cells typically shift their energy production from oxidative phosphorylation to glycolysis[59], and we observed that transient stimulation downregulates oxidative phosphorylation genes (Fig. 9n, Supplementary Fig. 15; glycolysis genes are not yet upregulated). Sustained stimulation activates genes associated with mTORC-driven metabolic changes and c-Myc and E2F-driven cell cycle progression (e.g. *CDK4* and *POLD2*), but transient stimulation does not (Fig. 9n, Extended Data Fig. 9i, Supplementary Fig. 15), suggesting that IL-2 signaling must be sustained to pass the G1/S checkpoint. Transient stimulation did activate genes associated with formation of the mitotic spindle (e.g. *DOCK2* and *KIF1B*) (Fig. 9n, Extended Data Fig. 9i, Supplementary Fig. 15), suggesting that preparations for mitosis are made immediately upon T cell activation prior to cell cycle checkpoints. These results illustrate how designed facilitated dissociation can be used to probe outstanding cell biological questions.

Conclusions

We show that by explicitly considering excited intermediate states in designing coupled protein systems, a broad range of facilitated dissociation systems can be designed. We employ a switchable target binder (host) and a flexible effector that can rapidly bind and switch the

target·host complex to induce a large steric clash with the target, forming a strained excited ternary complex. By modulating the strain energy of the ternary complex, we can tune the resulting acceleration of target dissociation. Crystal structures throughout the facilitated dissociation process confirm our ability to design excited states and large register-shift conformational changes. Our designed dynamic systems have both high dynamic range and rapid stimulus response, illustrating the kinetic advantage of facilitated dissociation over mutually exclusive competition.

Power stroke mechanisms[13,36] can more efficiently generate force compared to ratchet mechanisms (in which a single large step is rectified at the end of the conformational change)[41]. Induced folding underlies the kinesin power stroke[60], and our flexible effector likely also folds upon binding, accelerating the conformational transition by lowering the energy barrier: energetic costs of uphill steps along the transition coordinate are compensated by formation of additional interactions with the folding peptide[39,40,61]. In contrast to this induced-fit mechanism of the flexible effector, we find that a rigid effector provides reduced rate acceleration even though it binds more tightly[42]. In kinesin and other biological systems it is difficult to directly probe the role of effector flexibility and folding upon binding on overall function; our designed model systems in contrast allow direct comparison of flexible and rigid effectors and demonstrate that the former yield faster conformational transitions against loads.

Most known examples of facilitated dissociation couple the target and effector through a combination of direct steric overlap[22–25,31,37] and intricate allostery[19,20,27–30]. In contrast, because our allosteric mechanism of switching steric clashes places no specific requirements on the binder or target, our approach can be used to dynamically regulate protein-protein interactions quite generally: by fusing to our switch, almost any binding interaction can be made to rapidly switch off in the presence of an effector. Our approach immediately transferred to rapidly switching active IL-2-like signaling complexes: we obtained multiple working designs on the first attempt from testing 24 designs. Such switchable cytokines enable controlling the duration of IL-2 signaling to investigate early events in signaling and to tune the cell response through timing-sensitive regulatory mechanisms further downstream[58] (e.g., disrupting signaling complexes at the cell surface or later in the endosome[55] could distinguish cellular responses induced by signaling from each compartment[62]). Therapeutically, systemic administration of the effector and local administration of the switchable cytokine could elicit strong immune activation at only the site of administration (since any cytokine that escapes into circulation would be deactivated by the effector). More generally, our work provides a route to designing the rates and pathways of protein motion and change, which should ultimately enable construction of complex lifelike protein machinery.

Methods

Design of structured switch-binder fusions (hosts) allosterically coupling the target and effector

In PyMOL, we manually positioned the switch relative to the binder·target complex subject to several constraints: there is no steric overlap between the target and switch state X, there is large steric overlap between the target and switch state Y, the smallest deformation that could be undergone by the switch and target to resolve this clash is in the desired direction, and the switch C-terminus and binder N-terminus are relatively oriented such that sensible additional structure could be built between the switch and binder to rigidly fuse them as positioned. To aid in visualizing this additional structure, we also included placeholder helices while manually positioning the switch and binder, effectively "sketching" the fusion (Supplementary Fig. 4b).

We then refined these sketches into actually plausible backbones. For the initial fusions including AS0, we extracted the center four residues of the placeholder helix, then used inpainting with RosettaFold[63] to scaffold that fragment between the switch and binder. For later fusions including the AS1 variants and ASNeo2 designs, we first used Rosetta FastDesign[64] to sample around the starting sketch for designable positions of the switch, binder, and placeholder helices while keeping the region of the state X switch that clashes in state Y fixed relative to the target, then used RFDiffusion[4] (conditioned on the secondary structure and block adjacency of the sketches) to build structure between the sampled switch and binder positions. During both structure generation approaches, we masked noncritical residues on the switch and binder interfacing with the fusion structure. Following generation of the fusion backbone structure, we used ProteinMPNN[5] to optimize sequences for the fusion structure and the masked residues on the switch and binder. To filter designs, we used AF2[6] (with initial guess (AF2-IG)[65] for complex predictions) to predict the structure of the fusions alone, with the target, and with the effector, selecting designs for which each structural state is correctly and confidently predicted by a majority of the five model weight sets. Finally, for the AS1 variants and ASNeo2 designs, we used AF2-IG to predict the structure of the strained ternary complexes, selecting sets with a diversity of deformation directions.

Design of induced-fit register shift switches

Designs AS1, AS2, AS5, and AS7 were generated starting from design AS0, which contains the hinge switch cs221. When cs221 was designed, its state Y was generated by copying the N-terminal domain (helices 1–4) of its parent scaffold (DHR20[66]), aligning helix 4 of the copy to the corresponding helix of DHR20 offset by 3 residues, and combining the transformed N-terminal domain and original C-terminal domain into a single protein[7]. Thus, relative to the C-terminal domain, the N-terminal domain is both rotated around and translated along the axis of helix 4, exposing a cleft between the domains for binding a helical peptide. Now, to generate a new state X for this switch that retains an open cleft, we repeated this procedure but aligned the N-terminal domain with a residue offset of −4 instead of 3, so that overall this position of the N-terminal domain is shifted from state Y along helix 4 by one heptad (Supplementary Fig. 4e). This introduces minimal rotation and thus maintains the open cleft. We combined this new position of the N-terminal domain with the entire C-terminal domain of AS0 (including the fusion to LHD101B), then used Rosetta FastDesign to further sample designable positions of the N-terminal domain around this starting point. In half the design trajectories, we included a placeholder helix in the cleft to help ensure it remains open. We then used inpainting with

RosettaFold to generate loops connecting the domains, then paired these complete state X backbones with the original effector-bound state Y of AS0 (also generating new loops between domains in state Y as necessary to match the loop lengths of each new state X).

To generate single sequences supporting both states, we first performed multi-state design with Rosetta FastDesign (enforcing sequence symmetry between states) to further refine the paired backbones so they are more mutually compatible, then used ProteinMPNN with residue probabilities tied at corresponding positions between states to optimize sequences simultaneously for both conformations[7]. During these sequence design steps, the sequence of the effector and of the binder fusion was kept fixed. To filter designs, we used AF2-IG to predict the structure of the switches both with and without the effector, selecting designs for which the new state X (in the absence of effector) and state Y (in the presence of effector) are correctly and confidently predicted by a majority of the five model weight sets. To further ensure these designs favor state X in the absence of effector and state Y in the presence of effector, we only selected designs that scored more favorably in Rosetta in state X than in state Y, but also scored more favorably in state Y with the effector bound than the sum of the scores of state X and the unbound effector.

Design of rapid sensors

We first sought to cage the SmBiT peptide within the effector so that, through reverse facilitated dissociation, binding the target would rapidly uncage the SmBiT to enable luciferase reconstitution. We grafted SmBiT onto the effector peptide at a range of positions, then screened these "SmBiTgraft" variants for binding to AS0 and rapid dissociation upon binding the target. We used AS0 as the base design, reasoning that its closed state X would slow undesired peptide reassociation. For each working SmBiTgraft, we then generated a flexibly linked LgBiT-SmBiTgraft-AS0 construct. The best construct shows low luciferase activity which rapidly increases upon addition of target, but only slowly upon addition of effector peptide (which must compete directly with SmBiTgraft) (Extended Data Fig. 6). To demonstrate the modularity of this platform, using the methods described above for designing hosts, we rigidly fused a SARS-CoV-2 RBD binder (LCB1[49]) to the switch in place of the target binder such that the RBD clashes with the switch in state Y but not in state X, and tested 16 of these "AScov" fusion designs.

Recombinant expression and purification

Synthetic DNA fragments encoding each design were obtained from IDT as eBlocks and cloned into custom vectors using Golden Gate assembly[67]. Designs usually carried a C-terminal sequence-specific nickel-assisted cleavage (SNAC) tag[68] and 6xHis tag (MSG-Protein-GSGSHHWGSTHHHHHH). Proteins to be captured on the chip for SPR experiments carried an N-terminal AviTag™ and C-terminal 6xHis tag (MSGLNDIFEAQKIEWHESSG-Protein-GSGHHHHHH). For the SEC binding experiments shown in Supplementary Fig. 6 and for screening SmBiTgraft effector peptide variants with SPR, the effector was fused to superfolder GFP in a sfGFP-GSSG-Effector-GSHHHHHH construct. To rapidly break split luciferases, AS1 was fused to LgBiT in a MSG-AS1-linker-LgBiT-GSHHHHHH construct and the target was fused

to SmBiT in a MSG-target-linker-SmBiT-GSHHHHHH construct. In the rapid sensors, AS0 and AScov were fused to LgBiT and a SmBiT-containing effector in a MSGHHHHHHGS-LgBiT-linker-SmBiTgraft-linker-(AS0 or AScov)-GS construct.

All proteins were expressed from NEB BL21(DE3) *E. coli* cells using TBII (MpBio) autoinduction media with 0.5% (w/v) glycerol, 0.05% (w/v) glucose, 0.2% (w/v) lactose, 20 mM $MgSO_4$, trace metal mix, and 50 µg/mL kanamycin. 50 mL expression cultures were grown either at 37°C for 16–20 hr or at 37°C for 6–8 hr then at 18°C for 16–20 hours. Cells were harvested by centrifugation, resuspended in 5 mL lysis buffer (100 mM Tris HCl pH 8.0, 200 mM NaCl, 50 mM imidazole, 1 mM PMSF, 1 Pierce™ Protease Inhibitor Mini Tablets, EDTA-free per 50 mL), and lysed by sonication. The lysate was clarified by centrifugation at 14,000 x g for 30 min. Protein in the soluble lysate was bound to 1 mL Ni-NTA resin (Qiagen), washed with 5 mL low salt wash buffer (20 mM Tris HCl pH 8.0, 200 mM NaCl, 50 mM imidazole), 5 mL high salt wash buffer (20 mM Tris HCl pH 8.0, 1 M NaCl, 50 mM imidazole), and 5 mL low salt wash buffer, and eluted in 1.2 mL elution buffer (20 mM Tris HCl pH 8.0, 200 mM NaCl, 500 mM imidazole) after a 0.4 mL pre-elution. The proteins were further purified by SEC on an FPLC system with a Superdex 200 Increase 10/300 GL column in TBS (20 mM Tris pH 8.0, 100 mM NaCl) with 1 mL fractions. When possible, fractions probably corresponding to protein monomers were selected. Final protein concentrations were estimated using molar extinction coefficients predicted from the protein sequence and integrating the absorbance at 280 nm over the selected fractions. Correct protein molecular weights were confirmed using LC-MS.

Peptide synthesis

The effector peptide cs221B was chemically synthesized by GenScript. The TAMRA-labeled effector used in FP experiments was synthesized as previously described[7].

Size-exclusion chromatography (SEC) binding assay

Individual host proteins, sfGFP-effector, and 1:1 host:sfGFP-effector mixtures were prepared at 20 µM in TBS (20 mM Tris pH 8.0, 100 mM NaCl). 0.5 mL of each solution was injected onto a Superdex 200 Increase 10/300 GL column in TBS and absorbance at 230 nm was monitored for changes in retention volumes of the mixture compared to the individual proteins.

Fluorescence polarization (FP)

FP binding experiments with TAMRA-labeled effector were performed at 25°C in TBS (20 mM Tris pH 8.0, 100 mM NaCl) with 0.05% v/v TWEEN20 in 96-well plates (Corning 3686). Parallel and perpendicular fluorescence intensity was measured using a Synergy Neo2 plate reader with an FP 530/590 filter cube. Fluorescence polarization *P* (in units of mP) was calculated by the following expression.

$$P = \frac{\{parallel\ fluorescence\ intensity\} - \{perpendicular\ fluorescence\ intensity\}}{\{parallel\ fluorescence\ intensity\} + \{perpendicular\ fluorescence\ intensity\}} \times 1000$$

For affinity measurements, host proteins were titrated by two-fold serial dilution across TAMRA-effector (at a constant concentration between 0.1 and 1 nM) through 24 wells, with a final volume of 80 µL in each well. Plates were incubated for at least 12 hours at room temperature to fully equilibrate before measurement. To determine affinities, the following binding isotherm function was fitted to the measured polarization values using nonlinear least-squares minimization.

$$P = P_0 + P_1 f_{bound}$$

$$f_{bound} = \frac{1}{2[E]}\left([H] + [E] + K_D - \sqrt{([H] + [E] + K_D)^2 - 4[H][E]}\right)$$

where P is the modeled polarization, P_0 is the polarization of free effector, P_1 is the change in polarization upon binding the host, f_{bound} is the fraction of effector bound to the host, [*H*] and [*E*] are the total concentrations of host and effector respectively, and K_D is the affinity between the host and effector. When the fit K_D is lower than [*E*], affinities are too strong to be accurately measured with this method, so "K_D < [*E*]" is reported.

For kinetic competition measurements, the target LHD101An1 was titrated by two-fold serial dilution across the host protein (at a constant concentration of 22 nM) through 5 wells (a 6th well with just the host was also included) with a final volume of 72 µL in each well. Plates were incubated for 1 hour to allow the host and target to equilibrate. To each well, 8 µL of 200 nM TAMRA-effector was added and rapidly mixed using a multichannel pipette, and the measurement was started immediately afterward. This resulted in a 20 nM final concentration of both host and effector in 80 µL final volume per well. The following single exponential decay function was fitted to the measured polarization time courses using nonlinear least-squares minimization.

$$P = P_0 + P_1\left(1 - e^{-k_{app}t}\right)$$

where P is the modeled polarization, P_0 is the polarization of free effector, P_1 is the amplitude of the change in polarization, k_{app} is the apparent rate constant, and t is the time after the start of the measurement.

To measure facilitated dissociation in the reverse direction, host and TAMRA-effector were incubated at a 2:1 ratio to fully saturate the effector with host, diluted to 4 nM host and 2 nM effector, and distributed across 11 wells (40 µL in each well). In 9 separate wells, the target was titrated by a four-fold serial dilution with constant excess unlabeled effector (40 µM). Just excess unlabeled effector at 40 µM was prepared in the 10th separate well (to measure the base rate of effector dissociation), and buffer was prepared in the 11th (to confirm the baseline remains stable). 40 µL of these target+effector solutions were added to the 11 host+TAMRA-effector wells and rapidly mixed using a multichannel pipette, and the measurement was started immediately afterward. This resulted in final concentrations of 2 nM host, 1 nM TAMRA-effector, 20 µM unlabeled effector (to make dissociation of TAMRA-effector irreversible), and varying concentrations of target in 80 µL final volume per well. The following single exponential decay

function was fitted to the measured polarization time courses using nonlinear least-squares minimization.

$$P = P_0 + P_1 e^{-k_{app} t}$$

The following hyperbolic function was fitted to the apparent rate constants k_{app}.

$$k_{app} = \frac{k_{off,TH:E}[T]}{K_{1/2} + [T]} + k_{off,H:E}$$

where $k_{off,H:E}$ is the base effector off-rate constant, $k_{off,TH:E}$ is the off-rate constant for accelerated effector dissociation from the ternary complex, $K_{1/2}$ is the concentration at which half the rate increase from $k_{off,H:E}$ to $k_{off,TH:E}$ is reached, and [T] is the concentration of target present.

Surface plasmon resonance (SPR)

Proteins to be captured on the SPR chip were expressed with an N-terminal AviTag™ and purified as described above, except that the proteins were biotinylated following elution from the Ni-NTA resin: to the elutions, 5 µg/mL BirA (Avidity), 10 mM ATP, 10 mM $Mg(OAc)_2$, and 100 µM d-biotin were added and allowed to incubate at room temperature for at least 4 hours prior to further purification by SEC. Successful biotinylation was confirmed using LC-MS. SPR measurements were performed at 25°C in HBS-EP+ buffer (Cytiva) on a Biacore 8K instrument. Biotinylated proteins were immobilized on the chip using the Biotin CAPture system (Cytiva).

For measurements of target off-rate constants, biotinylated target protein was immobilized on the chip. To measure base off-rate constants $k_{off,T:H}$, host proteins at 50 nM were flowed over the chip for 60 s, then dissociation was measured for 2 hr. To measure accelerated off-rate constants $k_{off,T:HE}$, preincubated host-effector complexes (host at 1 µM and effector at 5 µM to ensure the host is saturated with effector) were flowed for 60 s to form the ternary complex on the chip, then dissociation was measured for 4–20 min under constant flow of 5 µM effector. Most dissociation data was fitted with the following double exponential decay function to account for populations of host protein with different dissociation kinetics.

$$S = S_0 + S_1 e^{-k_{app,1}(t-t_0)} + S_2 e^{-k_{app,2}(t-t_0)}$$

where S is the modeled SPR response, S_0 is the baseline, S_1 and S_2 are amplitudes relating to the sizes of each host population, $k_{app,1}$ and $k_{app,2}$ are apparent rate constants corresponding to each host population, t is the time, and t_0 is the time at which dissociation initiates. The reported rate constant typically corresponds to the faster and higher amplitude exponential in the fit; instances where other criteria are used to determine which rate constant corresponds to the change of interest are noted. When clearly only one host population is present (often indicated by $k_{app,1} \approx k_{app,2}$ or a large difference between S_1 and S_2 when fitting a double exponential), the following single exponential decay function was fitted instead, where the parameters are the same as above. Instances where single exponentials were used are noted.

$$S = S_0 + S_1 e^{-k_{app}(t-t_0)}$$

To measure the rate constant of effector association to form the ternary complex, biotinylated host protein was immobilized on the chip. The host protein was saturated with target by flowing 5 μM target over the chip for 4 min, then a varying concentration of effector and 5 μM target was flowed over the chip for 2–4 min to associate the effector, and finally 5 μM target was flowed over the chip for 4 min to monitor effector dissociation. Target was included at 5 μM (higher than its affinity to the ternary complex) throughout the experiment to ensure the host remained saturated with target, preventing changes in target binding from convoluting the response from effector binding. Association data was fitted with the following single exponential decay function.

$$S = S_0 + S_1\left(1 - e^{-k_{app}(t-t_0)}\right)$$

where S is the modeled SPR response, S_0 is the baseline, S_1 is the amplitude, k_{app} is the apparent rate constant, t is the time, and t_0 is the time at which dissociation initiates.

With the peptide effector, the following linear function was fitted to the apparent rate constants.

$$k_{app} = k_{on,TH:E}[E] + k_{off,TH:E}$$

where $k_{on,TH:E}$ and $k_{off,TH:E}$ are on- and off-rate constants and [E] is the concentration of effector flowed over the chip.

With the 3hb effector, the following hyperbolic function was fitted to the apparent rate constants.

$$k_{app} = \frac{1}{2}\left(k_{switch} + k_{unswitch} + k_{on,TH:E}[E] + k_{off,TH:E}\right)$$

$$-\frac{1}{2}\sqrt{\left(k_{switch} + k_{unswitch} - k_{on,TH:E}[E] - k_{off,TH:E}\right)^2 + 4k_{unswitch}k_{on,TH:E}[E]}$$

where k_{switch} is the rate constant for the $TH_X \rightarrow TH_Y$ conformational change, $k_{unswitch}$ is the rate constant for the $TH_Y \rightarrow TH_X$ conformational change, $k_{on,TH:E}$ and $k_{off,TH:E}$ are on- and off-rate constants, and [E] is the concentration of effector flowed over the chip. This function describes the slow relaxation rate constant of binding by conformational selection[2]. The data can be fit with only the slow relaxation because, since the conformational pre-equilibrium favors state X (i.e. $k_{switch} << k_{unswitch}$), the effect of the fast relaxation on k_{app} is minimal. During the fit, $k_{off,TH:E}$ was constrained to a low value (< 1e–4 s^{-1}), as observed.

To measure the effector concentration–dependent rate constant of the full facilitated dissociation process, either biotinylated target protein or biotinylated common gamma γ_c ectodomain (Acro Biosystems ILG-H85E8) was immobilized on the chip. For experiments with ASNeo2 designs, the ASNeo2 hosts were preincubated with IL-2Rβ ectodomain (Acro Biosystems CD2-H5221) before association with γ_c. Each experiment involved multiple cycles of host association and induced dissociation under flow of various concentrations of effector obtained by two-fold serial dilution (Supplementary Fig. 8a). Throughout these cycles, a small population of host that is unresponsive to the effector ("Hn," due to partial degradation or misfolding induced by the strain in the ternary complex) could accumulate on the chip (Supplementary Fig. 8a,b). The following

system of differential equations describing the expected behavior of the proteins on the chip (accounting for this accumulation) can be fitted to the dissociation curve of cycle *n* (Supplementary Fig. 8c).

$$\frac{d[THE]}{dt} = -k_{off,T:HE}[THE] + k_{on,TH:E}[TH][E] - k_{off,TH:E}[THE]$$

$$\frac{d[TH]}{dt} = -k_{off,T:H}[TH] - k_{on,TH:E}[TH][E] + k_{off,TH:E}[THE]$$

$$\frac{d[THn]}{dt} = -k_{off,T:Hn}[THn]$$

with initial values computed for each cycle by

$$[TH]_{final,0} = 0$$

$$[THn]_{final,0} = 0$$

$$[T]_{final,n-1} = 1 - [TH]_{final,n-1} - [THn]_{final,n-1}$$

$$[THE]_{initial,n} = 0$$

$$[TH]_{initial,n} = [TH]_{final,n-1} + f_{responsive}[T]_{final,n-1}$$

$$[THn]_{initial,n} = [THn]_{final,n-1} + \left(1 - f_{responsive}\right)[T]_{final,n-1}$$

and the modeled concentrations of each complex state on the chip is related to the SPR response by

$$S = f_n(a_{TH}[TH] + a_{THE}[THE] + a_{THn}[THn])$$

where *S* is the modeled SPR response, [*THE*], [*TH*], and [*THn*] are concentrations of complex states on the chip, t is the time after the start of the dissociation cycle, [*E*] is the concentration of effector flowed over the chip, $k_{off,T:H}$, $k_{off,T:HE}$, $k_{on,TH:E}$, $k_{off,TH:E}$, and $k_{off,T:Hn}$ are on- and off-rate constants, a_{TH}, a_{THE}, and a_{THn} are amplitudes relating the concentration of each state on the chip to an SPR response, f_n is an amplitude fudge factor for cycle *n* accounting for small differences in amplitude across cycles, and $f_{responsive}$ is the fraction of host that is responsive to the effector. Varying all these parameters, this model is then globally fit to the dissociation curves of all cycles using nonlinear least-squares minimization. Note that with a sufficiently high value of $k_{on,TH:E}$, this model's dissociation kinetics are primarily determined by the target dissociation parameters $k_{off,T:H}$ and $k_{off,T:HE}$; meanwhile, the effector binding parameters $k_{on,TH:E}$ and $k_{off,TH:E}$ tend to tightly covary and cannot be accurately determined from these fits. Also note that for designs with low values for $k_{off,T:HE}$, this model may be less accurate because the assumption that [*THE*] = 0 at the beginning of each cycle may no longer be valid. To compute the effective rate constant of the full facilitated dissociation process for intact host, we used the following simplified system of differential equations which no longer accounts for a small population of unresponsive host.

$$\frac{d[THE]}{dt} = -k_{off,T:HE}[THE] + k_{on,TH:E}[TH][E] - k_{off,TH:E}[THE]$$

$$\frac{d[TH]}{dt} = -k_{off,T:H}[TH] - k_{on,TH:E}[TH][E] + k_{off,TH:E}[THE]$$

$$[THE]_{initial} = 0$$

$$[TH]_{initial} = 1$$

For each effector concentration [*E*], this system was solved for the half-time of the target:host interaction $t_{1/2}$ using the rate parameters determined from the original model fit to the data, and the effective rate constant of the full dissociation process k_{eff} was computed from each half-time as follows.

$$[THE](t_{1/2}) + [TH](t_{1/2}) = 0.5$$

$$k_{eff} = \frac{ln(2)}{t_{1/2}}$$

The following hyperbolic function was fitted to the effective rate constants (constrained to the values of $k_{off,T:HE}$ and $k_{off,T:H}$ obtained from the global fit).

$$k_{eff} = \frac{k_{off,T:HE}[E]}{K_{1/2} + [E]} + k_{off,T:H}$$

where $k_{off,T:H}$ is the base effector off-rate constant, $k_{off,T:HE}$ is the off-rate constant for accelerated effector dissociation from the ternary complex, $K_{1/2}$ is the concentration at which half the rate increase from $k_{off,T:H}$ to $k_{off,T:HE}$ is reached, and [*E*] is the concentration of effector flowed over the chip.

The discrepancy in the 3hb EC_{50} between the 3hb association experiment in Fig. 6f (right) and the target facilitated dissociation experiment in Fig. 6h (right) could result from the fusion tag used to affix AS1 to the surface competing with the 3hb for binding the cleft, reducing the apparent 3hb on-rate in the 3hb association experiment but not in the target facilitated dissociation experiment.

All SPR measurements in the main figures were repeated at least once, obtaining similar results.

Circular dichroism (CD) spectroscopy

CD spectra were measured at 25°C on protein samples at 0.2 mg/mL in TBS (20 mM Tris pH 8.0, 100 mM NaCl) using a Jasco J-1500 spectrophotometer.

X-ray crystallography

AS1 TH and THE complexes required increased hydrophobicity to crystallize. This was accomplished by lysine methylation (for crystals AS1_TH #1, AS1_TH #2, and AS1_THE #1) or hydrophobic surface mutations K46L, E50W, K172W, and E173Y (for crystal AS1_THE #2).

Protein was expressed from NEB BL21(DE3) *E. coli* cells using TBII autoinduction media as above but at a larger scale: either 8x 50 mL or 1–2x 500 mL cultures. Cells were harvested by centrifugation, resuspended in lysis buffer, and lysed by sonication. The lysate was clarified by centrifugation at 14,000 x g for 30 min. Protein in the soluble lysate was bound to 8 mL Ni-NTA resin (Qiagen), washed with 10 mL low salt wash buffer, 30 mL high salt wash buffer, and 10mL SNAC cleavage buffer (100 mM CHES, 100 mM Acetone oxime, 100 mM NaCl, 500 mM GnCl, pH 8.6)[63], and incubated in 40 mL SNAC cleavage buffer + 2 nM $NiCl_2$ for 12 hours at room temperature to cleave. Afterwards, the flowthrough was collected and the beads were washed with 40 mL lysis buffer (minus the protease inhibitors). The amount of cleaved protein in the flowthrough and wash was assessed with SDS-PAGE, and fractions with enough cleaved protein were concentrated and further purified using SEC on an FPLC system with either a Superdex 75 Increase 10/300 GL column or a HiLoad 20/600 Superdex 75 pg column in either TBS (20 mM Tris pH 8.0, 100 mM NaCl) or lysine methylation buffer (50 mM HEPES pH 7.5, 250 mM NaCl) if lysines in the protein are to be methylated. For protein complex cocrystallization, the purified proteins and/or chemically synthesized effector were mixed at equimolar ratios. For some samples (resulting in crystals AS1_TH #1, AS1_TH #2, and AS1_THE #1), lysines were methylated as previously described[69], and the reaction was quenched using SEC on an FPLC system to buffer-exchange into TBS. Finally, the samples were concentrated to crystallization levels.

Crystallization experiments were conducted using the sitting drop vapor diffusion method. Initial crystallization trials were set up in 200 nL drops using the 96-well plate format at 20 ˚C. Crystallization plates were set up using a Mosquito LCP from SPT Labtech, then imaged using UVEX microscopes and UVEX PS-256 from JAN Scientific. Diffraction quality crystals formed in 0.2 M Magnesium chloride hexahydrate, 0.1 M Sodium cacodylate pH 6.5 and 50% v/v PEG 200 for AS1_H; in 0.2 M Sodium chloride, 0.1M Na/K phosphate pH 6.2 and 50% v/v PEG 200 for CS221B; in 0.1 M Sodium acetate pH 5.0, 5% w/v γ-PGA (Na+ from LM) and 30% v/v PEG 400 for LHD101An1; in 0.2 M Magnesium chloride hexahydrate, 0.1 M Tris pH 8.5 and 25% w/v Polyethylene glycol 3,350 for AS5_HE; in 0.1 M Sodium acetate pH 5.0, 20% (v/v) MPD for AS5_H; in 0.2M 1,6-Hexanediol, 0.2M 1-Butanol, 0.2M 1,2-Propanediol, 0.2M 2-Propanol, 0.2M 1,4-Butanediol, 0.2M 1,3-Propanediol, Sodium HEPES; MOPS (acid) pH 7.5 and 40% v/v PEG 500 MME; 20% w/v PEG 20000 for AS1_HE; in 0.1 M Citric acid pH 3.5 and 2.0 M Ammonium sulfate for AS1_THE #1; in 1.0 M Lithium chloride, 0.1 M Citrate pH 4.0, and 20 % w/v PEG 6000 for AS1_THE_#2; in 2.4 M Sodium malonate pH 7.0 for AS1_TH #1 ($P\ 6_1\ 2\ 2$); and in 1.8 M Ammonium citrate tribasic pH 7.0 for AS1_TH #2 ($P\ 2_1\ 2_1\ 2_1$).

Diffraction data was collected either at the National Synchrotron Light Source II on beamline 17-ID-1 (FMX/AMX) or Advanced Light Source beamline 821/822 or Advanced Photon Source NECAT 24ID-C. X-ray intensities and data reduction were evaluated and integrated using XDS[70] and merged/scaled using Pointless/Aimless in the CCP4 program suite[71]. Structure

determination and refinement starting phases were obtained by molecular replacement using Phaser[72] using the designed model for the structures. Following molecular replacement, the models were improved using phenix.autobuild; with rebuild-in-place to false and using simulated annealing. Structures were refined in Phenix[73]. Model building was performed using Coot[74]. The final model was evaluated using MolProbity[75]. Data collection and refinement statistics are recorded in Extended Data Table 1.

Double electron-electron resonance (DEER) spectroscopy

Spin label modeling and distance distribution predictions were performed as previously described[7] using chiLife[76] with the off-rotamer sampling method[77]. Site pair selections were performed as previously described[7]. Host protein variants containing cysteines at the selected sites were purified as described above, except that 0.5 mM TCEP was included in the lysis buffer and the first two Ni-NTA resin washes, and the proteins were labeled immediately after elution from the Ni-NTA resin: to the elutions, 50 µL of 200 mM MTSL in DMSO was added and allowed to incubate for at least 2 hours at room temperature prior to further purification by SEC. Successful labeling was confirmed using LC-MS. DEER samples were prepared at 20 µM labeled host protein in deuterated solvent buffered by 20 mM Tris at pH 8.0 with 100 mM NaCl and 20% d_8-glycerol (Cambridge Isotope Laboratories, Inc.) as a glassing agent. When appropriate, target and effector were added to a concentration of 100 µM each. 15-30 µL of each sample were loaded into a quartz capillary (Sutter Instrument, 1.1 mm inner diameter, 1.5 mm outer diameter) and flash frozen with liquid nitrogen. Samples were stored at −80°C until the DEER experiment was conducted.

DEER experiments were performed as previously described[7]. An ELEXSYS E580 spectrometer (Bruker) at Q-band (~34 GHz) with an EN5107D2 resonator (Bruker) was used for all experiments. Temperature was maintained at 50 K using a cryogen-free cooling system (ColdEdge). The 4-pulse DEER sequence was used using 60 ns Gaussian observer pulses with a full width at half maximum (FWHM) of 30 ns and a frequency near the center of the field-swept spectrum and 150 ns sech/tanh probe pulses with center 80 MHz above the observer frequency, 80 MHz bandwidth, and a truncation parameter of 10. All shaped pulses were generated using the SpinJet arbitrary waveform generator (Bruker). Pulse shapes were calculated using PulseShape (https://github.com/stolllab/PulseShape) using both resonator compensation and transmitter nonlinearity compensation. All data were collected using a 2 ms shot repetition time, 8-step phase cycling, and τ_1 averaging from 400 ns to 528 ns in 16 ns steps. All other experimental parameters (including pump pulse time step, τ_2 delays, number of scans, and others) were chosen on a per-sample basis and are reported in Supplementary Table 3.

All DEER data were analyzed using the DeerExp module of the eprTools Python package (https://github.com/mtessmer/eprTools). All data were fit using separable non-linear least squares[78]. The foreground signal was modeled using Tikhonov regularization with the second derivative operator. The regularization parameter was selected using generalized cross-validation. The background was modeled using a 3D-homogeneous spin distribution. An additional penalty restraining the modulation depth to be low was used to prevent the fitting of

long-distance artifacts in the foreground as previously done[79]. Confidence intervals were estimated using bootstrap sampling with 100 samples using a fixed regularization parameter. Fit parameters such as the regularization parameter, the modulation depth, and the signal-to-noise ratio are listed in Supplementary Table 3.

Molecular dynamics (MD) simulations

Input files for the MD simulation were prepared with CHARMM-GUI[80,81] with AlphaFold2 structure as the initial structure. The rectangular water box of edge length 10Å was placed around the protein. The water box contained potassium and chlorine ions of concentration 0.15M that neutralized the protein's net charge. The ions were placed in the water box using Monte Carlo method. To model the system, the CHARMM36m force field[82] was used. After the explicit solvent system was made, the system was minimized and equilibrated before the production MD run. All three steps were performed with the GROMACS 2020.2 MD engine[83,84].

Steepest descent method was used for energy minimization, for 5000 steps with an energy tolerance of 1000 kJ/mol/nm. The neighbor list was updated every 10 steps with a cut-off distance of 1.2 nm. Cut-off was used to calculate Van der Waals interactions with switch distance of 1.0 nm and cut-off distance of 1.2 nm. The force was smoothly switched off between the switch distance and the cut-off distance. The fast smooth particle-mesh Ewald method was used to calculate electrostatics with a cut-off distance of 1.0 nm. All bonds with hydrogen atoms were treated as rigid using the Linear Constraint Solver (LINCS) algorithm[85].

The equilibration step was performed with a leap-frog algorithm using a timestep of 1 fs and total simulation time of 125 ps. The system was propagated in the NVT ensemble. The temperature was maintained at 303.15K using the velocity rescaling method. The solute and solvent were coupled with a time constant for coupling of 1 ps. The center of mass translational velocity was removed every 100 steps to prevent the system from drifting. The same cut-off scheme for Van der Waals and electrostatic interactions were used as in the minimization step except the neighbor list was updated every 20 steps. The velocities were generated from Maxwell distribution with temperature of 303.15K. The same LINCS method was used to constrain the hydrogen atoms during the equilibration step.

The production step was performed with a leap-frog algorithm using a timestep of 2 fs and total simulation time of 1 μs. The trajectories with the same initial equilibrated structure were obtained in triplicate. The system was propagated in the NPT ensemble. Temperature was maintained at 303.15K using velocity rescaling method. The solute and solvent were coupled with a time constant of 1 ps. Exponential relaxation pressure coupling and isotropic coupling with time constant of 5.0 ps was used to maintain pressure at 1.0 bar. The cut-off schemes for Van der Waals and electrostatic interactions were the same as those used in the minimization step, except that the neighbor list was updated every 20 steps and the Coulomb cut-off distance was set as 1.2 nm. The same center of mass velocity removal was the same as that used in the equilibration step. The same LINCS method was used to constrain the hydrogen atoms during the production step.

Analysis of the trajectories, such as RMSD and RMSF calculations, was performed with MDAnalysis[86]. To simulate DEER distance distributions from these trajectories, structures along each trajectory were clustered using the Gromos clustering algorithm[87] in GROMACS, distance distributions were predicted (using chiLife[76] with the off-rotamer sampling method[77]) for the center structure of each cluster, and the resulting distributions were averaged weighted by the occupancies of their corresponding clusters.

Chain reactions with Förster resonance energy transfer (FRET) readout

Hinge protein cs201F_E249L (H2) was purified as described above, except that 0.5 mM TCEP was included in the lysis, wash, and elution buffers, and the SEC buffer was PBS (20 mM sodium phosphate pH 7.0, 100 mM NaCl, 0.5 mM TCEP). To double label with dyes, 50 μM H2 was incubated with 250 μM Alexa Fluor™ 555 C_2 Maleimide (donor, Thermo Fisher Scientific) and 250 μM Alexa Fluor™ 647 C_2 Maleimide (acceptor, Thermo Fisher Scientific) shaking at room temperature for at least 2 hours. The reaction was quenched by adding DTT to 10 mM, and the proteins were separated from excess dye by SEC in TBS (20 mM Tris pH 8.0, 100 mM NaCl).

FRET binding experiments were performed at 25°C in TBS (20 mM Tris pH 8.0, 100 mM NaCl) with 0.05% v/v TWEEN20 in 96-well plates (Corning 3686). Fluorescence intensity was measured using a Synergy Neo2 plate reader, exciting the donor at 520 nm wavelength and reading acceptor emission at 665 nm wavelength.

To measure E2-target on-rate constant, 40 μL H2 at 10 nM was prepared in 6 wells. To each well, 40 μL E2-target at various concentrations was added and rapidly mixed using a multichannel pipette, and the measurement was started immediately afterward. The following single exponential decay function was fitted to the measured FRET time courses using nonlinear least-squares minimization.

$$S = S_0 + S_1 e^{-k_{app} t}$$

where S is the modeled fluorescence signal, S_0 is the fluorescence at equilibrium, S_1 is the amplitude of the change in fluorescence, k_{app} is the apparent rate constant, and t is the time after the start of the measurement. The following linear function was fitted to the apparent rate constants.

$$k_{app} = k_{on}[E2] + k_{off}$$

where k_{on} and k_{off} are on- and off-rate constants and [*E2*] is the total concentration of E2-target.

To measure the accelerated transfer of E2 from AS114 to H2, 1067 nM AS114 and 533 nM E2-target were incubated for 15 minutes to fully cage E2-target in AS114. A control solution of just 1067 nM AS114 was also prepared. 37.5 μL of 42.7 nM H2 was prepared in 8 wells. 37.5 μL of AS114·E2-target was added to 4 wells and 37.5 μL of AS114 was added to the other 4 wells using a multichannel pipette, and the measurement was started immediately afterward. 5 min later, 5 μL of buffer, 100 μM target, 16 μM effector, or 100 μM target and 16 μM effector were

added to each set of 4 wells using a multichannel pipette, and the measurement was immediately continued for 1 hr. Mixing components at these concentrations resulted in final concentrations of 500 nM AS114, 250 nM E2-target, 20 nM H2, 1 μM effector, and 6 μM target. A baseline drift function of the following form was fit to the AS114+buffer data and subtracted from the other time courses.

$$S = \frac{S_1}{1 + e^{-k(t - t_{1/2})}} + S_0$$

where S is the modeled fluorescence signal, S_0 is the fluorescence at equilibrium, S_1 is the amplitude of the change in fluorescence, k is a rate constant, t is the time after the start of the measurement, and $t_{1/2}$ is the time at which the fluorescence has changed by half the full amplitude. AS114 was used as, in state X, it does not clash with E2 extending past the target in E2-target.

Rapid sensors and split enzymes with luminescence readout

Luminescence experiments were performed at 25°C in TBS (20 mM Tris pH 8.0, 100 mM NaCl) with 0.05% v/v TWEEN20 in 96-well plates (Corning 3686). Luminescence was measured using a Synergy Neo2 plate reader with a LUM filter cube.

To measure rapid breakage of a split luciferase, 111 pM AS1-LgBiT and 22 nM target-SmBiT were incubated for 1 hr to load AS1 with the target and reconstitute the split luciferase. 72 μL of this mixture was added to 2 wells. 8 μL of 1/10 diluted Nano-Glo® substrate (Promega N1130) and either 10 μM effector and 200 μM target or just 200 μM target was added to these wells using a multichannel pipette, and the measurement was started immediately afterward. Excess target was included to fully outcompete target-SmBiT to enable measurement of dissociation rate. Mixing components at these concentrations resulted in final concentrations of 100 pM AS1-LgBiT, 20 nM target-SmBiT, 1 μM effector, 20 μM target, and 1/100 diluted Nano-Glo® substrate.

To measure rapid analyte sensing, 64 μL of 12.5 pM sensor was added to 8 wells. 8 μL of 1/10 diluted Nano-Glo® substrate was added to these wells using a multichannel pipette, and the measurement was started immediately afterward. 5 min later, 8 μL of various concentrations of analyte obtained by ten-fold serial dilution were added using a multichannel pipette, and the measurement was immediately continued for 30–60 min. Mixing components at these concentrations resulted in final concentrations of 10 pM sensor and 1/100 diluted Nano-Glo® substrate. Analytes were target, effector, or SARS-CoV-2 RBD (Acro Biosystems SPD-C52H3). Fig. 8e shows a time course with 800 nM SARS-CoV-2 RBD.

Live cell single molecule imaging

For cell surface labeling, receptors were N-terminally fused to suitable tags using a pSems vector including the signal sequence of Igκ (pSems-leader). Common gamma chain (γ_c) was fused to the ALFA-tag[88] and IL-2Rβ was fused to nonfluorescent monomeric GFP (mXFP)[89]. HeLa cells

(ACC 57, DSMZ Germany) were cultured as previously described[90]. For transient transfection, cells were incubated for 4–6 h with a mixture of 150 mM NaCl, 10 µL of 1 mg/mL polyethylenimine (PEI MAX®, Polysciences 24765) and 200 ng of DNA of pSems leader ALFAtag-γc and 2800ng of pSems leader mXFPe1-IL-2Rβ[91]. Labeling, washing and subsequent imaging were performed after mounting the coverslips into custom-made incubation chambers with a volume of 1 ml. Cells were equilibrated in medium with FBS but lacking phenol red, supplemented with an oxygen scavenger and a redox-active photoprotectant (0.5 mgmL^{-1} glucose oxidase (Sigma-Aldrich), 0.04 mgmL^{-1} catalase (Roche), 5% w/v glucose, 1 µM ascorbic acid and 1 µM methylviologene) to minimize photobleaching[92].

Selective cell surface receptor labeling was achieved by using anti-GFP and anti-ALFAtag Nanobodies (NBs), which were site-specifically labeled by maleimide chemistry via a single cysteine residue at their C-termini[92]. Anti-ALFA NB labeled with Cy3B (DOL; 1.06) and anti-GFP NB labeled with ATTO 643 (DOL; 1.0) were added at concentrations of 3 nM each, at least 10 min before imaging. Coverslips were precoated with poly-l-lysine-graft-poly(ethylene glycol) to minimize unspecific binding of NBs and functionalized with RGD peptide for efficient cell adhesion[93].

During the imaging experiments, ASNeo2 was used at 100 nM, and 10 µM effector was used to induce receptor dissociation.

Dual-color imaging was carried out by total internal reflection fluorescence microscopy using an inverted microscope (IX-83, Olympus) equipped with a spectral image splitter (QuadView, Photometrics) and an EMCCD camera (iXon Ultra, Andor) as described in detail elsewhere[94]. Fluorophores were excited by sequential illumination with a 561-nm laser (2RU-VFL-P-2000-560-B1R, 2000W, MPB communications) and a 642-nm laser (2RU-VFL-P-2000-642-B1R, 2000W, MPB communications). Alternating laser excitation was achieved with a simple micro-controller (Arduino Uno) and open-source acquisition software[95] synchronizing laser shuttering via an AOTF (AA.AOTFnC-400.650-TN, AA Opto Electronic) and camera triggering. For long term tracking experiments, 1500 frames per channel were acquired at 40 fps. Resulting image stacks were divided into 5-frame stacks and dimerization was determined for each stack. For Fig. 9f, 3 time courses, each normalized to its average initial relative dimerization, are overlaid for each condition. For all other tracking experiments, 200 frames per channel were acquired at 40 fps and dimerization was determined over the whole image stack.

Dual-color single molecule co-tracking time-lapse images were evaluated using an in-house developed MATLAB software (SLIMfast4C, https://zenodo.org/record/5712332)[92]. After channel registration based on calibration with fiducial markers, molecules were localized using the multi-target tracking algorithm[96]. Immobile emitters were filtered out by spatiotemporal cluster analysis[97]. Frame-by-frame co-localization within a cut-off radius of 150nm was applied followed by tracking of co-localized emitters using the utrack algorithm[98]. Molecules co-diffusing for 10 frames or more were then identified as co-localized. Relative levels of co-localization were determined based on the fraction of co-localized particles relative to all localizations in the ALFA-

γc channel (561 nm). Diffusion properties were determined from pooled single trajectory using mean squared displacement analysis for all trajectories with a lifetime greater than 10 frames. Diffusion constants were determined from the mean squared displacement by linear regression. Relative dimerization was estimated by:

$$Relative\ Dimerization = \frac{\{co\text{-}localizations\}}{\{IL\text{-}2R\beta\ localizations\}}$$

FRET efficiencies were evaluated using an in-house developed MATLAB software (provided and described in detail elsewhere as supplementary software[94]). In brief, alternating laser excitation FRET experiments provide three separated emission channels: directly excited donor $D_{D_{ex}}^{D_{em}}$ and acceptor $A_{A_{ex}}^{A_{em}}$ as well as a sensitized FRET $F_{D_{ex}}^{A_{em}}$ channels. First, channels were aligned based on calibration with fiducial markers. Then, after applying a single molecule localization algorithm[99], single-molecule intensities were determined from background subtracted images ($I_{D_{ex}}^{D_{em}}$, $I_{A_{ex}}^{A_{em}}$, $I_{D_{ex}}^{A_{em}}$). To evaluate FRET efficiencies, donor-acceptor pairs were co-localized based on an optimized search radius. For these pairs, the apparent FRET Efficiency was calculated by:

$$E_{raw} = \frac{I_{D_{ex}}^{A_{em}}}{I_{D_{ex}}^{D_{em}} + I_{D_{ex}}^{A_{em}}}$$

In order to achieve accurate FRET efficiencies, standard further corrections were applied. These include the donor leakage coefficient, crosstalk corrected proximity ratio and the correction factor γ[94,100].

pSTAT5 signaling assay with human NK (YT) cells

Human NK (YT-1) cells were cultured in RPMI 1640 complete medium, supplemented with 10% fetal bovine serum, 2 mM L-glutamine, minimum essential non-essential amino acids, sodium pyruvate, 25 mM HEPES, and penicillin-streptomycin (Gibco). For the flow cytometry-based pSTAT5 detection assay, 2–5 × 10^5 IL-2Rα positive YT-1 cells were seeded in 350 µL of medium per well of a 96-well plate. The cells were stimulated with 1 nM ASNeo2 or Neo2 for 5 minutes at 37°C. As a control, 50 µL of untreated YT-1 cells were set aside at the start of each experiment and evaluated after 45 minutes alongside the treated cells. After stimulation, all cells were transferred to three separate wells containing either a control (no treatment), 10 µM Effector or 40 µM Ruxolitinib. One-seventh of the cells (i.e., 50 µl) were resuspended in 17 µl of 16% paraformaldehyde (PFA) for immediate fixation. This process was repeated at 5, 10, 15, 30, and 45-minute intervals. After all the time points were fixed, the cells were re-fixed in 4% PFA for 15 minutes at room temperature. Following fixation, the cells were washed once with PBS containing 0.5% BSA (PBSA) and permeabilized with 100% methanol for 45 minutes at 4°C. After permeabilization, the cells were washed twice with PBSA and stained for 1 hour at room temperature using Alexa Fluor® 647-conjugated Phospho-STAT5 (Tyr694) rabbit monoclonal antibody (Cell Signaling Technology, #9365, clone C71E5) diluted 1:100. After three washing steps, the cells were analyzed using a CytoFlex S flow cytometer (Beckman Coulter). Data were

analyzed with CytExpert software, and cells were gated based on SSC-A vs FSC-A. Each experiment was conducted in triplicate, and the results were analyzed accordingly.

For Fig. 9g, pSTAT5 signal is normalized to the background level. For Fig. 9h, n=3 time courses were normalized to the signal at time 0 (just prior to effector addition), a baseline signal was determined by the average of this normalized pSTAT5 of the untreated cells, then each time course was renormalized to this baseline signal. Some batches of cells were unresponsive to stimulation; data from these batches were excluded from analysis.

Cell Line Sources

HeLa cells for single molecule imaging were sourced from the German Collection of Microorganisms and Cell Cultures GmbH (ACC 57); YT (CD25+) cells were sourced from the American Type Culture Collection (ATCC). Cell lines were authenticated by STR profiling. HeLa cells were tested negatively for mycoplasma contamination by PCR.

Activation and stimulation of human T cells

Primary human peripheral blood mononuclear cells (PBMCs) isolated from a healthy human donor by leukapheresis were thawed and resuspended at a cell density of 2×10^6 cells/ml in T cell medium, which contained RPMI-1640 (Gibco), FBS (10% v/v, Gibco/Thermo Fisher Scientific), HEPES (25mM, Gibco/Thermo Fisher Scientific), penicillin/streptomycin (1% v/v, Gibco/Thermo Fisher Scientific), sodium pyruvate (1% v/v, Gibco/Thermo Fisher Scientific), MEM Non-Essential Amino Acids Solution (1% v/v, Gibco/Thermo Fisher Scientific), and 2-mercaptoethanol (0.1% v/v, Gibco/Thermo Fisher Scientific), and supplemented with human IL-2 (100 U ml^{-1}). For human T cell activation, cells were activated with plate-bound anti-human CD3ε (1µgml^{-1}, clone OKT-3, BioXCell) and soluble anti-human CD28 (5µgml^{-1}, clone 9.3, BioXCell) for 48h. Cells were then expanded in T cell medium with human IL-2 (100 U ml^{-1}) for 8 days. On day 9, IL-2 was withdrawn for 36 hours, after which cells were resuspended at 1×10^6 cells/ml and stimulated with ASNeo2 (1 nM or 5 nM) for either 5 or 25 minutes, as indicated. Effector peptide (10 µM) was then added to terminate signaling. After 48 or 72 hours, cells were collected for counting and phenotypic analysis by flow cytometry.

For Fig. 9i,j, cells were stimulated with 1 nM ASNeo2. For Fig. 9k–n, cells were stimulated with 5 nM ASNeo2.

Flow cytometry analyses of human T cells

For surface marker staining, cells were collected into U-bottom 96-well plates (Thermal Fischer Scientific), blocked with Human TruStain FcX™ (BioLegend), and incubated with indicated antibodies at 4°C for 20 min, followed by live/dead staining by 4',6-diamidino-2-phenylindole (DAPI, Thermo Fisher Scientific). Cells were then washed and resuspended with FACS buffer (PBS containing 0.2 % BSA, Sigma-Aldrich) for flow cytometry analyses. For phospho-STAT staining, primary human T cells were rested in T cell medium lacking IL-2 for 24h before signaling assays. Cells were plated in a 96-well round bottom plate in 50µl T cell medium. Cells were

stimulated with 50 µL of ASNeo2 for 5 or 25 minutes, followed by the addition of effector peptide and incubation for another 20 minutes at 37°C, and the reaction was terminated by fixation with 1.5% paraformaldehyde (PFA) for 15min at room temperature with agitation. Cells were washed and permeabilized with ice-cold 100% methanol for 60min on ice. Afterward, cells were washed with FACS buffer before staining with pSTAT5 antibodies for 1h at 4°C in the dark. Cells were washed and resuspended in FACS buffer for flow cytometry analyses. For caspase-3 staining, cells were first stained for surface markers and Zombie Violet Fixable Dye (BioLegend), followed by staining with a FITC Active Caspase-3 Apoptosis Kit (BD Biosciences) according to the manufacturer's protocol. For transcription factor staining, cells were first stained for surface markers and Zombie Violet Fixable Dye, then fixed and permeabilized using a Foxp3/Transcription Factor Staining Buffer Set (eBioscience) as per the manufacturer's instructions. Cells were subsequently incubated with the indicated antibodies for intracellular staining. Detection was performed using a CytoFlex (Beckman Coulter), and data were analyzed with FlowJo (v10.10.0).

Antibodies and reagents for flow cytometry of human T cells

The following antibodies or staining reagents were purchased from BioLegend: human CD3 (OKT3, 317324), human GATA3 (W19195B, 386906), human CD69 (FN50, 310932), human CD25 (BC96, 302611), human BCL2 (100, 658708), human Ki-67 (Ki-67, 350526), Human TruStain FcX™ (422302) and Zombie Violet™ Fixable Viability Kit (423114). The following antibodies or staining reagents were purchased from BD Biosciences: pSTAT5 (47/Stat5, 612599), and BD Pharmingen™ FITC Active Caspase-3 Apoptosis Kit (571606). DAPI was purchased from Thermo Fisher.

Antibodies were diluted 1:200 for surface markers (CD3, CD28, CD69, CD25), 1:100 for intracellular proteins (GATA3, Ki-67, BCL2), and 1:50 for pSTAT and caspase-3 staining.

Antibodies were validated by the manufacturers using flow cytometry.

qPCR

Human T cells on day 9 post-activation were subjected to IL-2 starvation for 36 hours. NT cells were maintained in culture without IL-2. For transient IL-2 signaling, cells were stimulated with ASNeo2 (5 nM) for 25 minutes, followed by the addition of Effector peptide (10 µM) to terminate signaling. For sustained signaling, ASNeo2 (5 nM) was continuously maintained in the culture medium. Total RNA was extracted using the Quick-RNA Miniprep Kit (Zymo Research) following the manufacturer's instructions. cDNA was synthesized using the High-Capacity cDNA Reverse Transcription Kit (Thermo Fisher Scientific) with random primers. Quantitative PCR (qPCR) was performed using Taqman master mix (Thermo Fisher Scientific) on a StepOnePlus™ Real-Time PCR Systems. BCL2 expression was measured using the TaqMan BCL2 assay, and gene expression was normalized to GAPDH (Thermo Fisher Scientific). Relative expression levels were calculated using the ΔΔCt method.

RNA-sequencing sample preparation and data analysis

Human T cells on day 8 post-activation were subjected to IL-2 starvation for 36 hours. NT cells were maintained in culture without IL-2. For transient IL-2 signaling, cells were stimulated with ASNeo2 (5 nM) for 25 minutes, followed by the addition of Effector peptide (10 μM) to terminate signaling. For sustained signaling, ASNeo2 (5 nM) was continuously maintained in the culture medium. After 6 hours, cells were collected, and total RNA was extracted using the Quick-RNA Miniprep Kit (Zymo Research). RNA libraries were prepared using a poly(A) enrichment-based mRNA library preparation kit following the manufacturer's instructions. Libraries were pooled and sequenced on the NovaSeq X Plus Series (PE150). Reads were aligned to the reference genome (GRCh38) using Rsubread, and gene expression was quantified with featureCounts. For exploring pathway enrichment, gene set co-regulation analysis (GESECA) was performed with Hallmark genesets. To reduce redundancy, we performed hierarchical clustering of Hallmark genesets with Jaccard's distance to yield 8 geneset clusters with minimal gene overlaps. Only one geneset with the lowest FDR-adjusted *P*-value per cluster is shown in figure 5. Differential expression analysis was performed using DESeq2, with FDR-adjusted *P*-value < 0.05 as a threshold for differential expression. Heatmaps were created using normalized counts of genes identified as differentially up- or down-regulated in both sustained vs. unstimulated and transient vs. unstimulated.

Statistics and Reproducibility

The main text SPR, CD, FP, FRET, and luminescence experiments, and also a subset of DEER and SEC experiments, were performed two (SPR in Fig. 6d,h, 4b; FRET in Fig. 8c; SEC in Supplementary Fig. 9a) or three (SPR in Fig. 6a,e,f,g; FP in Fig. 8b, Supplementary Fig. 5c, Supplementary Fig. 12; luminescence in Fig. 8d,e; SEC in Supplementary Fig. 6b; DEER with AS1 in Extended Data Fig. 2) times to ensure reproducibility and low variance, and one representative experiment was reported due to low variance among replicates. Having established low variance for these experiments, some similar measurements reported in the supplement were performed once. For all microscopy, cell staining, and qPCR/RNA-seq experiments, three or four independent biological replicates were performed unless otherwise noted in the figure caption. All attempted replications of all experiments were successful, with the exception that some batches of YT-1 cells were unresponsive to stimulation; the findings in Fig. 9h were not observed with those batches.

Data Availability

All data generated during this study are included in either the main text or as Supplementary Information. Data deposition, atomic coordinates, and structure factors for all crystal structures reported in this paper have been deposited in the Protein Data Bank (PDB), https://www.rcsb.org, with accession codes 9DCX, 9DCY, 9DCZ, 9DD0, 9DD1, 9DD2, 9DD3, 9DD4, 9DD5, and 9OLQ. PDB models and sequences for all designs and source data with analysis scripts has been deposited at Zenodo under https://doi.org/10.5281/zenodo.16749448. Single molecule tracking data has been deposited at Zenodo: calibration beads, unstimulated samples, long term measurements and labeled ligand experiments under https://doi.org/10.5281/zenodo.13957447, Neo2 and Neo2 + effector

under https://doi.org/10.5281/zenodo.13957498 and ASNeo2 and ASNeo2 + effector, as well as smFRET data under https://doi.org/10.5281/zenodo.13957540. The raw RNA-seq data have been deposited in the NCBI Sequence Read Archive (SRA) under BioProject accession code PRJNA1302552 at https://ncbi.nlm.nih.gov/bioproject/PRJNA1302552. The SKEMPI database can be accessed at https://life.bsc.es/pid/skempi2/database/index. The reference genome GRCh38 (accession code GCF_000001405.26) can be accessed at https://hgdownload.soe.ucsc.edu/goldenPath/hg38/bigZips/. Hallmark gene sets can be accessed from the Human Molecular Signatures Database (MSigDB) at https://www.gsea-msigdb.org/gsea/msigdb/collections.jsp.

Code Availability

Code used to generate designs and analysis scripts used to generate all figures has been deposited at Zenodo (design code: https://doi.org/10.5281/zenodo.16749263; data analysis: https://doi.org/10.5281/zenodo.16749448).

Authors and Acknowledgements

Authors

Adam J. Broerman[*1,2,3], Christoph Pollmann[4], Yang Zhao[5], Mauriz A. Lichtenstein[1,6], Mark D. Jackson[7], Maxx H. Tessmer[7], Won Hee Ryu[8], Masato Ogishi[5], Mohamad H. Abedi[1,2], Danny D. Sahtoe[1,2], Aza Allen[1,2], Alex Kang[1,2], Joshmyn De La Cruz[1,2], Evans Brackenbrough[1,2], Banumathi Sankaran[9], Asim K. Bera[1,2], Daniel M. Zuckerman[8], Stefan Stoll[7], K. Christopher Garcia[5,10], Florian Praetorius[*†1,2], Jacob Piehler[4], David Baker[*1,2,11]

1. Institute for Protein Design, University of Washington, Seattle, WA, USA.
2. Department of Biochemistry, University of Washington, Seattle, WA, USA.
3. Department of Chemical Engineering, University of Washington, Seattle, WA, USA.
4. Department of Biology/Chemistry and Center for Cellular Nanoanalytics, Osnabrück University, Osnabrück, Germany.
5. Department of Molecular and Cellular Physiology, Stanford University School of Medicine, Stanford, CA, USA.
6. Institute for Chemistry and Biochemistry, Freie Universität Berlin, Berlin, Germany.
7. Department of Chemistry, University of Washington, Seattle, WA, USA.
8. Department of Biomedical Engineering, Oregon Health and Science University, Portland, OR, USA.
9. Molecular Biophysics and Integrated Bioimaging, Lawrence Berkeley National Laboratory, Berkeley, CA, USA.
10. Howard Hughes Medical Institute, Stanford University, Stanford, CA, USA.
11. Howard Hughes Medical Institute, University of Washington, Seattle, WA, USA.

* Corresponding author email: broerman@uw.edu, florian.praetorius@ist.ac.at, dabaker@uw.edu

† Current address: Institute of Science and Technology Austria, Klosterneuburg, Austria

Acknowledgements and Funding

We thank P. J. Y. Leung, K. L. Shelley, A. Pillai, C. Demakis, M. Exposit, R. J. Ragotte, G. Ahn, and M. Glögl for helpful discussions and technical support, K. VanWormer and L. Goldschmidt for technical support, S. R. Gerben and A. Murray for protein production support, and X. Li, M. Lamb, Z. Taylor, and V. Adebomi for LC-MS support. This work was supported by the Audacious Project at the Institute for Protein Design (A.J.B., A.K., J.D.L.C., E.B., and A.K.B.), by a gift from Microsoft (A.J.B.), by the Nordstrom Barrier Institute for Protein Design Directors Fund (M.H.A. and F.P.), by Bill and Melinda Gates Foundation #OPP1156262 (A.K., J.D.L.C.), by the Open Philanthropy Project Improving Protein Design Fund (E.B., A.K.B.), by the National Institutes of Health's National Institute of Allergy and Infectious Disease grant R0AI160052 (A.K.B.), by CRI Irvington Postdoctoral Fellowship 315511 (Y.Z.), by National Cancer Institute K00 award 4K00CA274708 (M.O.), by National Science Foundation grant MCB 2119837 and National Institutes of Health grant GM115805 (W.H.R. and D.M.Z.), by National Institutes of Health grant GM151956 (S.S.), by NIH AI-51321 (K.C.G.), by the DFG grants PI 405/15 and SFB 1557 (C.P. and J.P.), and by the Howard Hughes Medical Institute (A.K.B., K.C.G, and D.B.). The EPR spectrometer used for the DEER experiments was in part supported by National Institutes of Health grant S10OD021557. This research used resources (FMX/AMX) of the National Synchrotron Light Source II, a U.S. Department of Energy (DOE) Office of Science User Facility operated for the DOE Office of Science by Brookhaven National Laboratory under Contract No. DE-SC0012704. The Center for BioMolecular Structure (CBMS) is primarily supported by the National Institutes of Health, National Institute of General Medical Sciences (NIGMS) through a Center Core P30 Grant (P30GM133893), and by the DOE Office of Biological and Environmental Research (KP1607011). This work is based upon research conducted at the Northeastern Collaborative Access Team beamlines, which are funded by the National Institute of General Medical Sciences from the National Institutes of Health (P30 GM124165). This research used resources of the Advanced Photon Source, a U.S. Department of Energy (DOE) Office of Science User Facility operated for the DOE Office of Science by Argonne National Laboratory under Contract No. DE-AC02-06CH11357. The Berkeley Center for Structural Biology is supported by the NIH, National Institute of General Medical Sciences, and the HHMI. The ALS is supported by the Director, Office of Science, Office of Basic Energy Sciences and US Department of Energy (DOE) (DE-AC02-05CH11231).

Author Contributions

A.J.B. developed the facilitated dissociation design concept, developed the computational design pipeline, designed the allosteric switches, and characterized their binding kinetics with SPR, FP, FRET, luminescence, and SEC experiments. C.P. performed and analyzed single molecule localization microscopy and NK (YT) signaling activity experiments. Y.Z. performed and analyzed transient stimulation experiments on primary T cells. M.A.L. and A.J.B. designed and characterized the rapid sensors. M.D.J. and M.H.T. performed and analyzed DEER experiments. W.H.R and A.J.B. performed and analyzed MD simulations. M.O. and A.J.B. analyzed RNA-seq

data. A.J.B. and M.H.A. performed initial signaling activity experiments. D.D.S. and A.A. performed site-saturation mutagenesis on LHD101. A.K., A.J.B., J.D.L.C., E.B., B.S., and A.K.B. determined and analyzed crystal structures. D.B., J.P., F.P., K.C.G., S.S., and D.M.Z. supervised research. A.J.B. and D.B. wrote the manuscript. F.P., C.P., M.A.L., Y.Z., M.H.T., and W.H.R. contributed to the manuscript. All authors read and commented on the manuscript.

Competing Interests

A.J.B., F.P., A.K.B., and D.B. are in the process of filing a provisional patent application that incorporates discoveries described in this article. The remaining authors declare no competing interests.

Extended Data

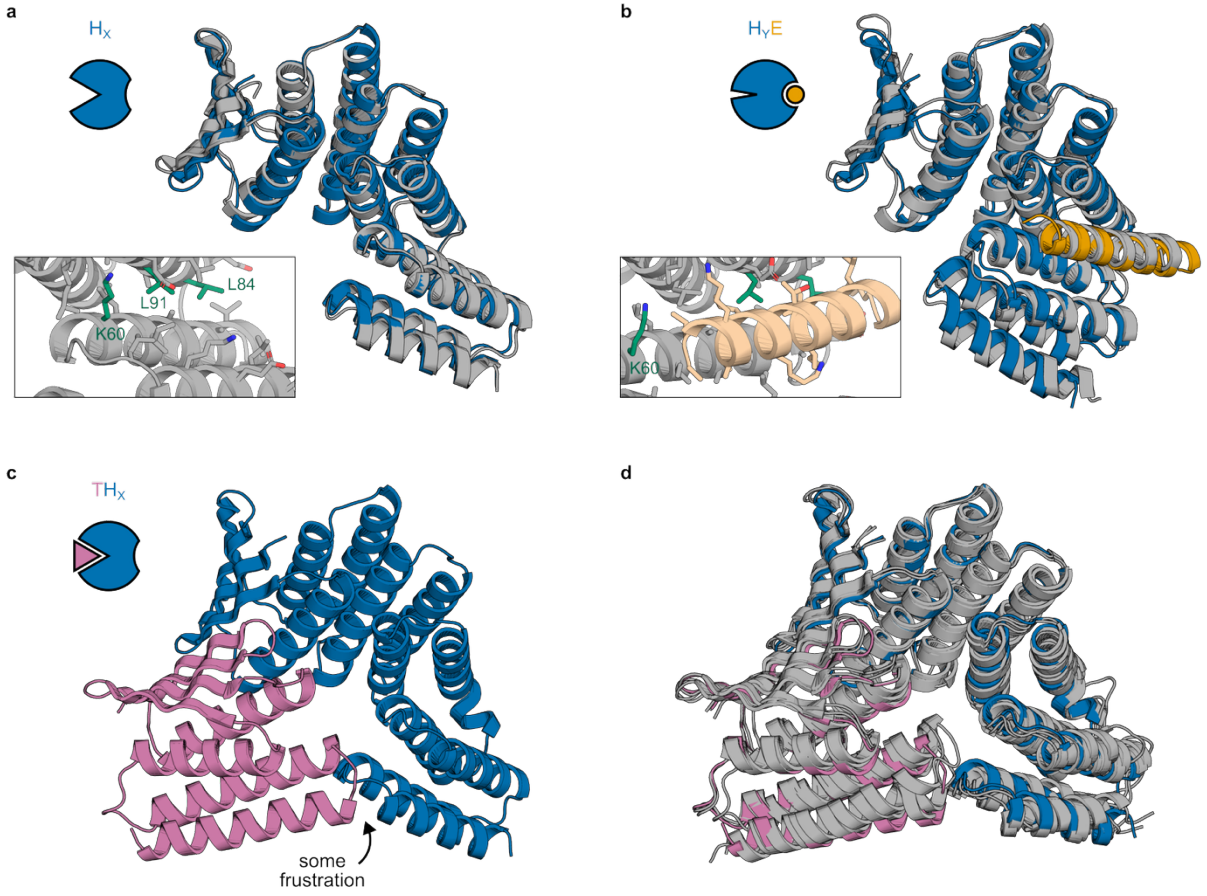

Extended Data Fig. 1: Structural characterization of AS5 and structural frustration of AS1 state TH_X. a, Crystal structure of AS5 alone (gray) overlaid with the design model of AS5 in state X (blue). Inset shows a detailed view of side chains in the partially-open effector-binding cleft. **b**, Cocrystal structure of AS5 and peptide effector (gray) overlaid with the design model of the AS5·effector complex in state Y (AS5 in blue, effector in orange). Inset shows the same view of the side chains in the effector-binding cleft as in (a). **c**, Design model of AS1 in state X (blue)

aligned to the target (pink), showing a minor clash. **d**, Three cocrystal structures of AS1 (with intact cleft) and target with methylated lysines (gray) overlaid with the AF2 model of the target·AS1 complex in state X (AS1 in blue, target in pink), showing fluctuation in the target binding conformation.

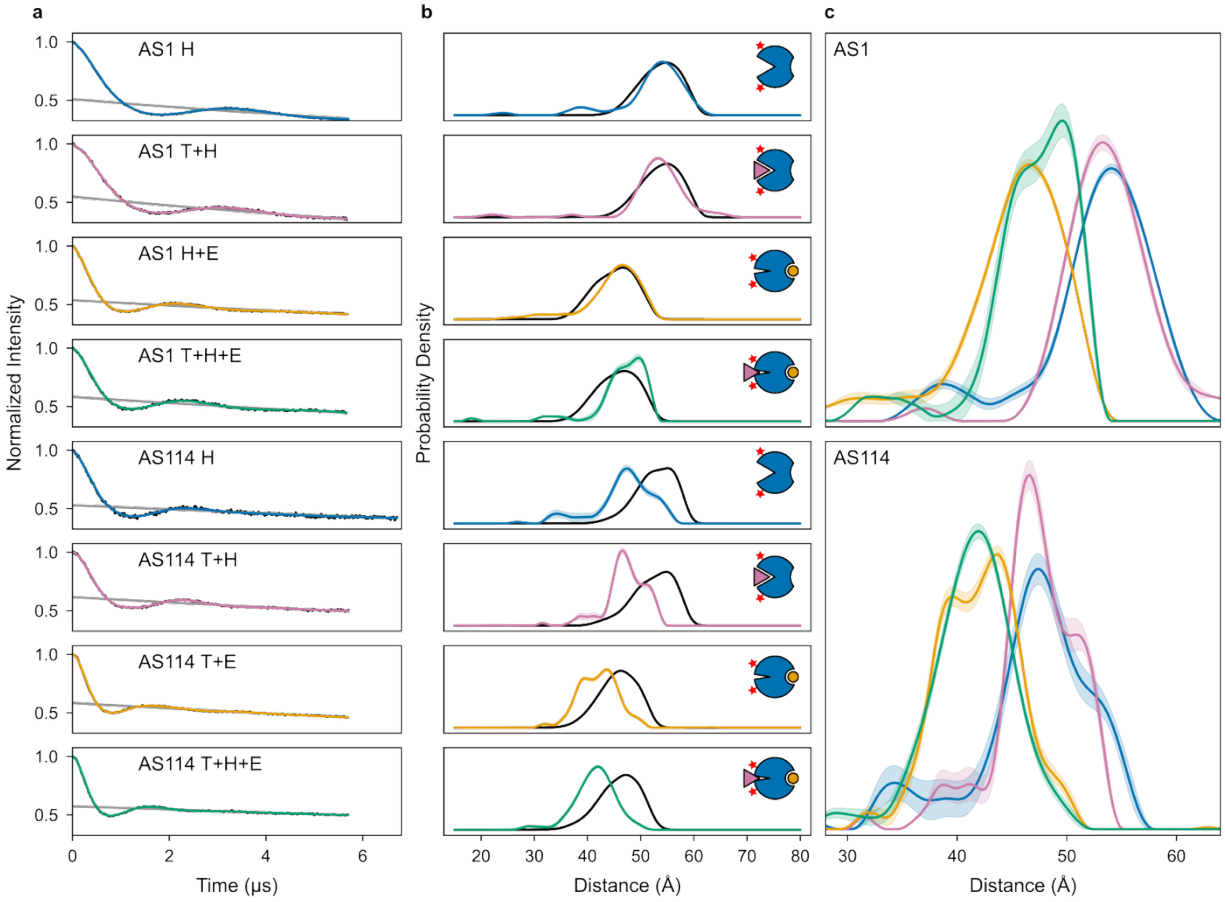

Extended Data Fig. 2: DEER characterization of AS1 and AS114. a, Raw DEER traces (black), foreground fits (colors), and background fits (gray) for AS1 and AS114 with all combinations of target and effector. Experiments on complexes included the target, effector, or both in excess over the host at concentrations higher than required to fully form the complex (Supplementary Fig. 9), and spin labels were placed far from the target and effector binding sites. Thus, changes in the DEER distance distributions with different combinations of target and effector should only reflect changes in host conformation. **b**, Distance distributions from experiment (colors) and simulated from the structural state represented by the cartoons (black). For AS1, the simulated and experimental distance distributions agree well, further validating that each state adopts its designed conformation. For AS114, the simulations consistently overestimate the experimental distribution by ~5 Å, but the shift in the distance distributions with the effector compared to those without validates the designed conformational change. **c**, Experimental distance distributions of all states, colored corresponding to (b). For both AS1 and AS114, the ternary complex distribution (green) aligns with the host-effector complex distribution (orange) and not with the host alone (blue) or target-host complex (pink) distributions, confirming that the ternary complex

is primarily in state Y. **b** and **c**, Lines represent the distance distribution that best fits the time domain data; shaded regions represent 95% confidence intervals from bootstrapping (methods).

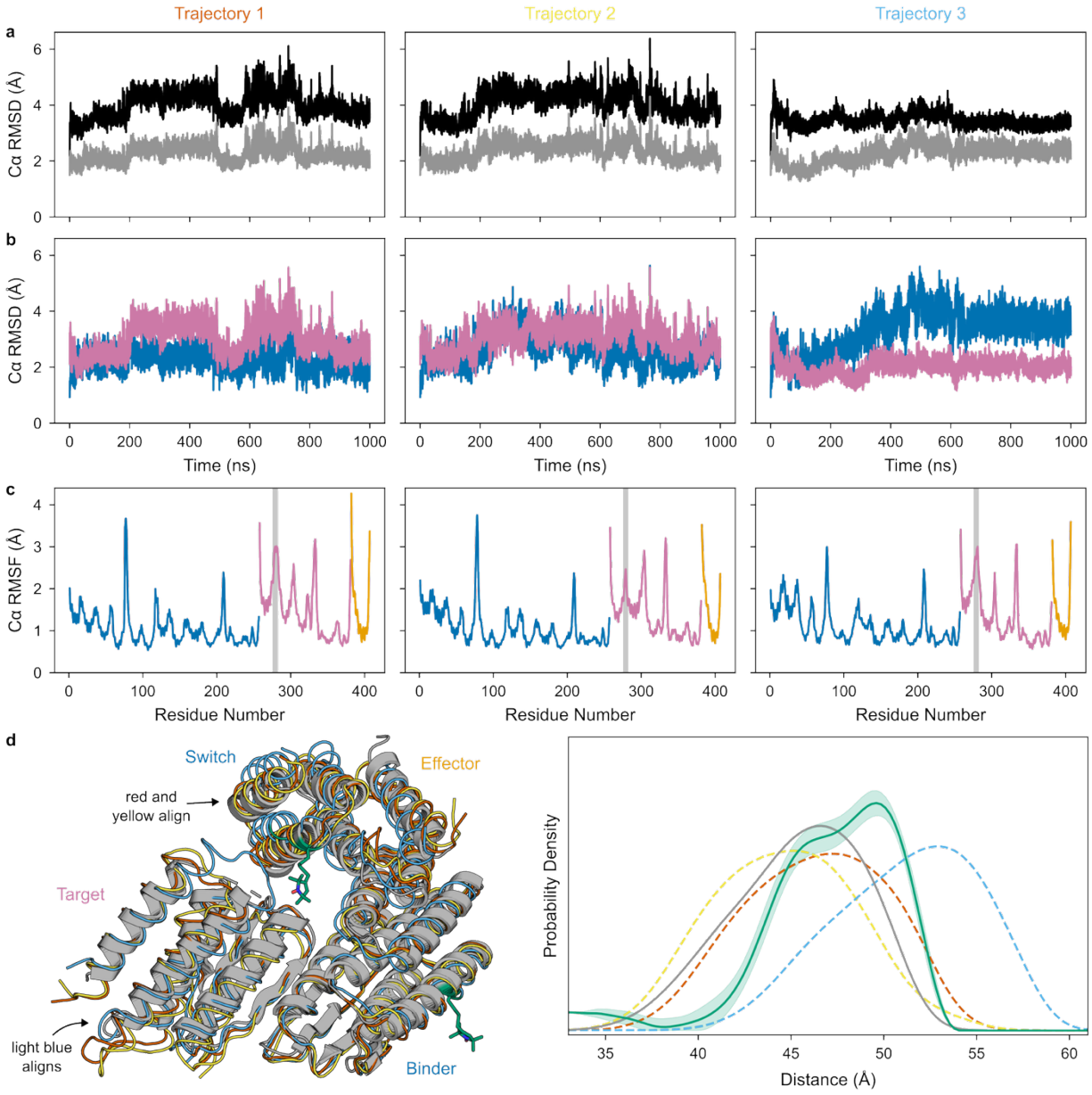

Extended Data Fig. 3: MD analysis of the AS1 ternary complex. a, Lower Cα RMSD of the MD trajectories from the crystal structure (gray) than from the aligned clashing design models of target and host·effector complex (black), showing that the MD simulations strain away from the clashing state in a manner similar to the crystal structure. **b**, Cα RMSD of the switch (blue) and target (pink) from their position in the crystal structure when the entire structures are aligned. Compared to trajectories 1 and 2, trajectory 3 shows reduced target deformation and increased switch deformation, showing that these trajectories differ in where they localize strain to resolve the clash. **c**, Per-residue Cα RMSF of the host (blue), target (pink), and effector (orange) in the

ternary complex computed from each trajectory. The clashing region of the target (highlighted in gray) shows significant flexibility, according with this region being disordered in the crystal structure. **d**, Comparison of MD simulations to experimental data. (Left) Crystal conformation of the ternary complex (gray) aligned to representative conformations from each MD trajectory (red, yellow, and light blue). DEER spin label positions are shown in green. In the crystal structure, the clashing region on the target is disordered. In the MD simulations, though flexible, this region remains mostly ordered, causing additional deformation compared to the crystal structure. Illustrating the differences in strain localization among trajectories shown in panel (b), in the first two trajectories (red and yellow), the switch conformation aligns with the crystal structure and the target deforms more; in the third trajectory (light blue), the target conformation aligns with the crystal structure and the switch deforms instead. (Right) experimentally measured DEER distance distribution of the ternary complex (green line representing the best fit to the time domain data and shaded region representing 95% confidence interval from bootstrapping (methods)) and distance distributions simulated from the crystal structure (gray line) or MD trajectories (dashed lines, colors correspond to the conformations shown at left). The distance distribution simulated from the crystal structure aligns with the left peak in the experimental distance distribution, whereas the distance distributions simulated from the MD trajectories span the experimental distance distribution, suggesting that these trajectories more fully sample the space of ternary complex dynamics.

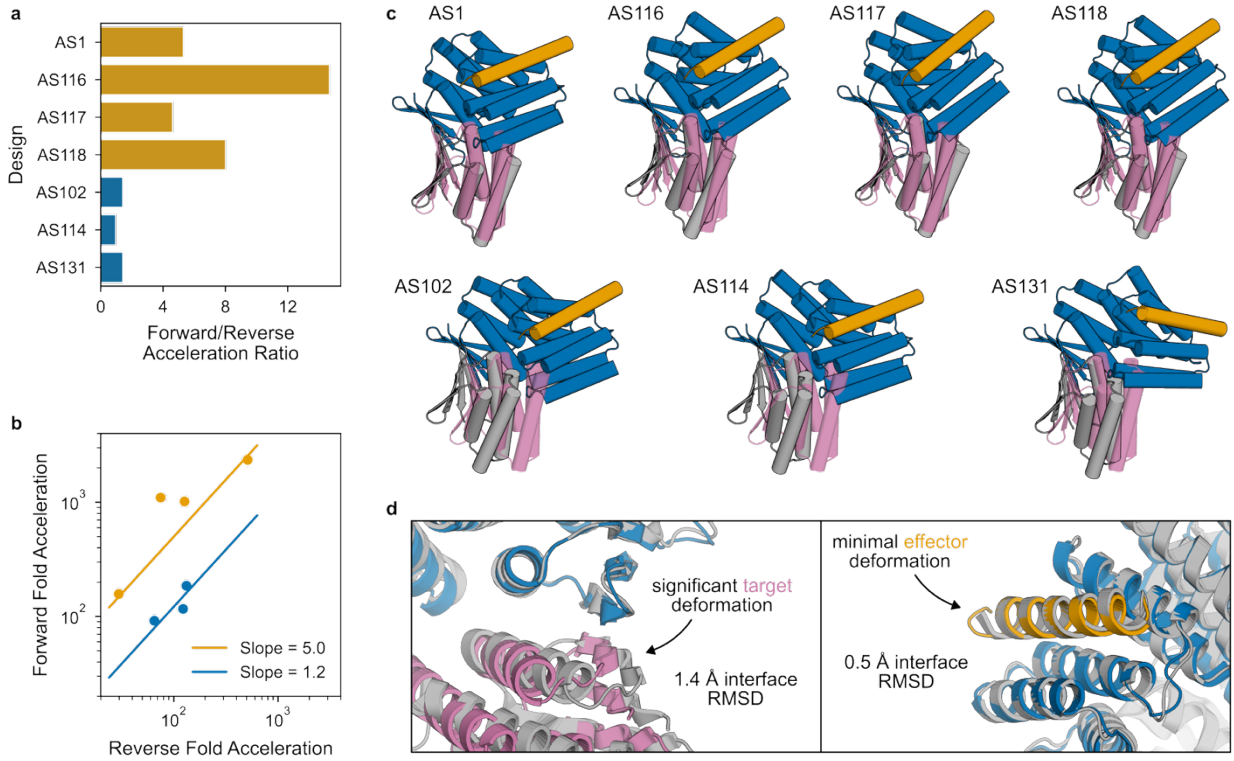

Extended Data Fig. 4: Nonuniform distribution of strain in the ternary complex. a, Ratios of fold accelerations in the forward direction to those in the reverse direction, given by the equation

$$\text{Acceleration Ratio} = \frac{\frac{k_{off,T:HE}}{k_{off,T:H}}}{\frac{k_{off,TH:E}}{k_{off,H:E}}}.$$

Acceleration ratios corresponding to designs with asymmetric distributions of strain are colored orange, and to symmetric blue. **b**, Plot of forward vs reverse acceleration ratios, with linear fits for the symmetric and asymmetric groups. Note that on a log-log plot, the slope of a straight line passing through the origin becomes the y-intercept. **c**, For each design, design model of host·effector complex in state Y (blue and orange) aligned to the target (pink) to show the designed allosteric clash, and (gray) AF2 prediction of the target position relative to the switch in the ternary complex to show how the clash resolves through global strain. The target deforms downward in designs with an asymmetric distribution of strain, shearing the beta sheet, whereas it deforms outward in designs with a more symmetric distribution of strain, bending the beta sheet. **d**, Comparison of the AS1 binder:target interface (left) and switch:effector interface (right) (aligned at the host side) in the binary (colors) and ternary (gray) complex conformations, all from crystal structures, showing the binder:target interface deforms significantly more than the switch:effector interface in the ternary complex.

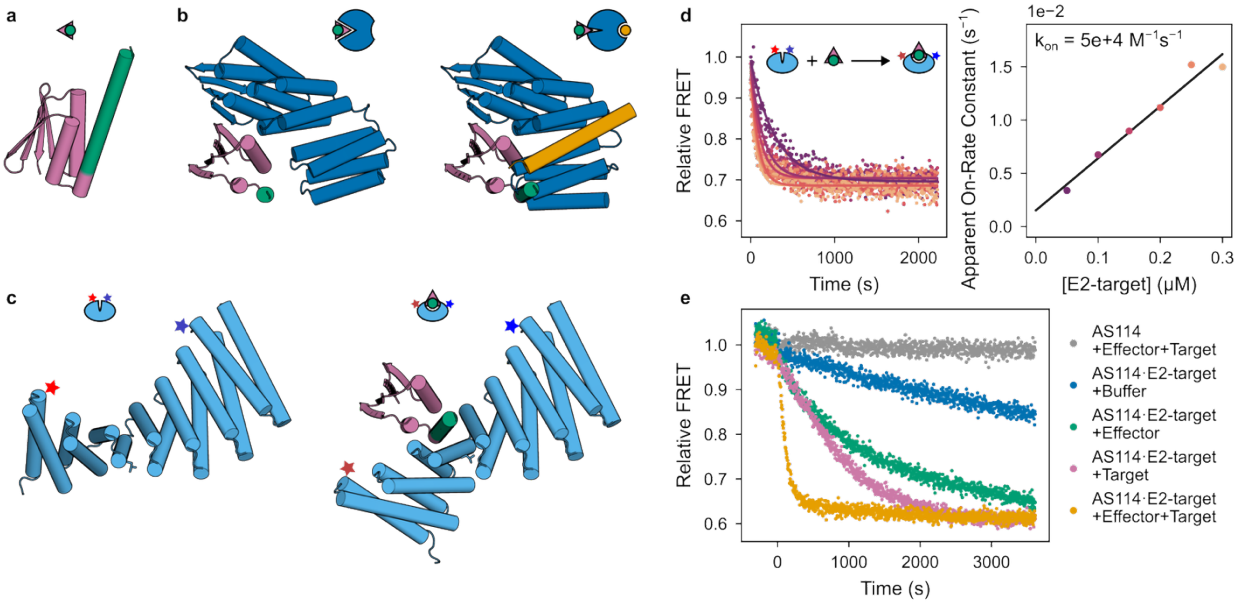

Extended Data Fig. 5: Construction and characterization of the chain reaction. a, Design model of E2-target, comprising the target LHD101A (with mutations R43V and V69Q) fused to the effector peptide "E2" (cs201B) for hinge cs201. E2 is colored green and LHD101A is colored pink. **b**, Design models of E2-target (green/pink) bound to AS114 (blue) in state X showing no clash (left) and in state Y with the effector peptide (orange) showing a strong clash (right). **c**, Design models of the reporter hinge "H2" (cs201F with mutation E249L (sticks) that increases E2 on-rate and labeled with Alexa Fluors 555 and 647 at positions indicated by stars) in state X (left) and in state Y with E2-target (right). AS114 and H2 would significantly overlap if simultaneously bound to E2-target, so their binding should be mutually exclusive: AS114 should

cage E2 until its release by the effector. **d**, Kinetics of E2-target and H2 association, measured by a change in FRET efficiency due to the conformational change in H2 upon binding. (Left) FRET time courses (normalized to the initial signal) with varying concentrations of E2-target and 5 nM H2; data (circles) fit with single exponentials (lines). (Right) apparent on-rate constants plotted against E2-target concentration (circles) and a linear fit. The value of the association rate constant (5e+4 $M^{-1}s^{-1}$) is higher than the reported value (4.5e+3 $M^{-1}s^{-1}$) for the original hinge cs201F with effector cs201B, suggesting that mutation E249L on H2 biases its conformational pre-equilibrium toward state Y to increase the apparent association rate. **e**, Additional data for the kinetically governed chain reaction shown in Fig. 8c. In the gray control time course, 500 nM AS114 was added to 20 nM H2, then 1 μM effector and 6 μM target was added at time 0, showing that none of these components bind to H2 to cause a change in FRET signal. In the other time courses, preincubated 500 nM AS114 and 250 nM E2-target was added to 20 nM H2, then buffer (blue), 1 μM effector (green), 6 μM target (pink), or both (orange) were added at time 0. A baseline drift (obtained from 500 nM AS114 after adding 20 nM H2 then at time 0 adding buffer) was subtracted from each time course, and time courses were normalized to the initial signal. The chain reaction proceeds faster when just excess target is added, likely due to blocking rebinding of E2-target to AS114 after transient dissociation[45], but this effect is insufficient to achieve full acceleration. The chain reaction also proceeds faster when just effector is added, but likely due to transient rebinding of E2-target to re-form the strained ternary complex, this also does not achieve full acceleration. Adding both effector (to accelerate E2-target dissociation from AS114) and excess target (to prevent E2-target rebinding to AS114) is required to fully accelerate the chain reaction. Note that if a single-chain effector is desired to fully accelerate the chain reaction, the effector and target could be flexibly fused into a single construct. Such a multivalent effector would be reminiscent of CITED2, whose multivalency enables rapid and unidirectional competition against HIF-1α[101].

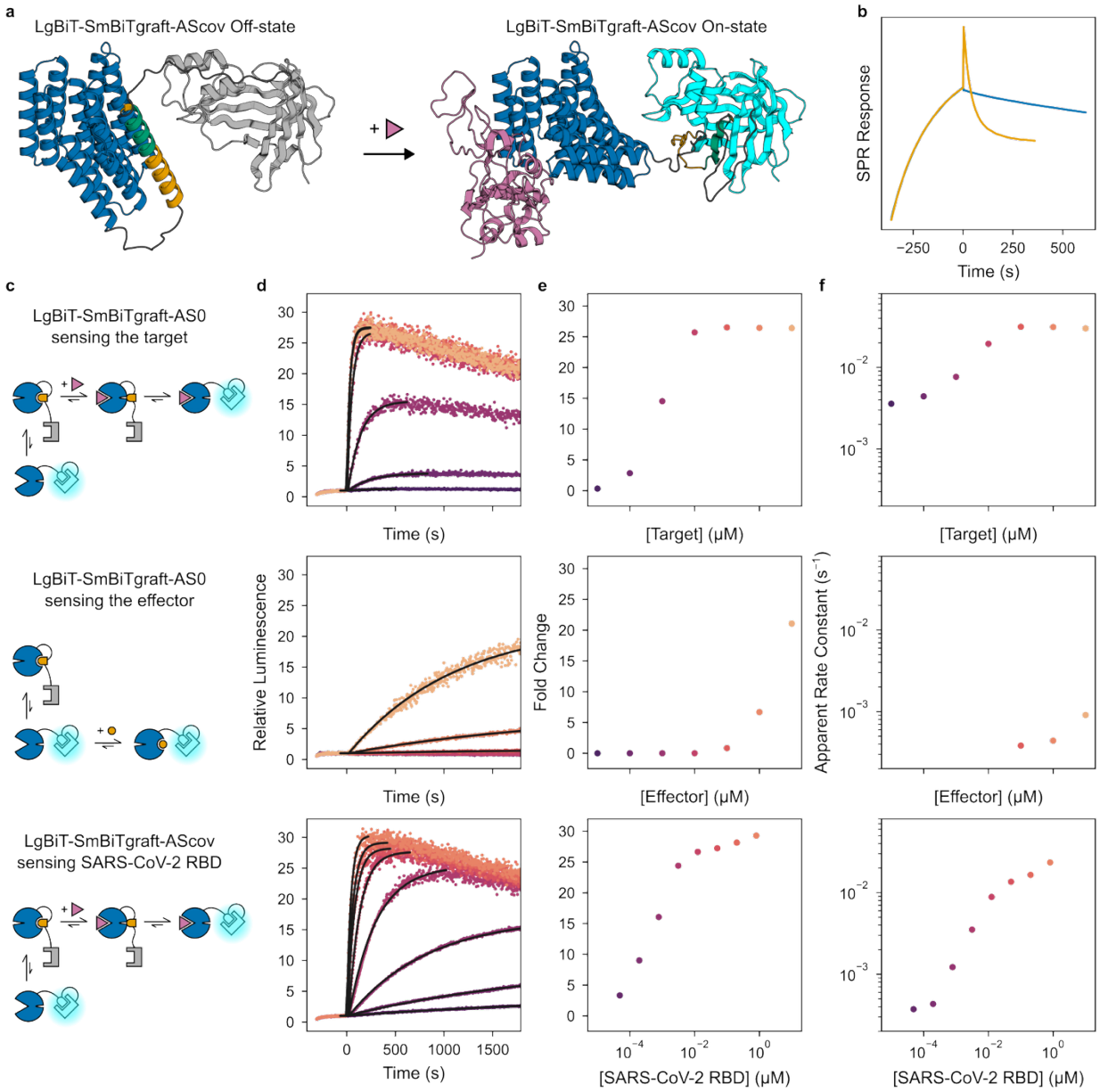

Extended Data Fig. 6: Construction and characterization of rapid sensors. a, Structural model of the best SARS-CoV-2 sensor construct, comprising AScov (blue), the SmBiTgraft peptide with the effector (orange) and grafted SmBiT (green), LgBiT (gray or cyan), and flexible linkers (black). In this design, SmBiT is caged in a helical conformation when SmBiTgraft is bound to the switch and is free to reconstitute the luciferase when SmBiTgraft is released. To form SmBiTgraft, SmBiT was grafted onto the effector peptide such that most of its hydrophobic residues are buried within the switch:SmBiTgraft interface when in the bound helical conformation. Since the original effector peptide binds so strongly to the switch, it could accommodate replacing some of its interface residues with residues from SmBiT without reducing its affinity so much that it no longer effectively cages the SmBiT. **b**, SPR data showing sfGFP-SmBiTgraft binding to AS0 (blue and orange, association phase), slow subsequent

dissociation in the absence of target (blue), and rapid subsequent dissociation upon addition of 10 μM target (orange) caused by rapid target binding to form a transient ternary complex, causing the spike at the beginning of the dissociation phase. **c–f**, Rapidly sensing the target through a facilitated dissociation mechanism (top), slowly sensing the effector limited by the slow base exchange rate of SmBiTgraft between binding AS0 and LgBiT (middle), and rapidly sensing the SARS-CoV-2 RBD with facilitated dissociation (bottom). **c**, Schematics showing the mechanism of sensing. **d**, Luminescence time courses (normalized to the initial signal) of 10 pM sensor construct then at time 0 adding varying concentrations of analyte (target, effector, or SARS-CoV-2 RBD); data (colors) fit (black) with single exponentials up to the maximum signal for time courses that showed appreciable signal increase. In some time courses, signal slowly decreases due to depletion of luciferase substrate. **e**, Luminescence signal fold change plotted against analyte concentration. **f**, Sensor response rate constant plotted against analyte concentration for time courses that showed appreciable signal increase.

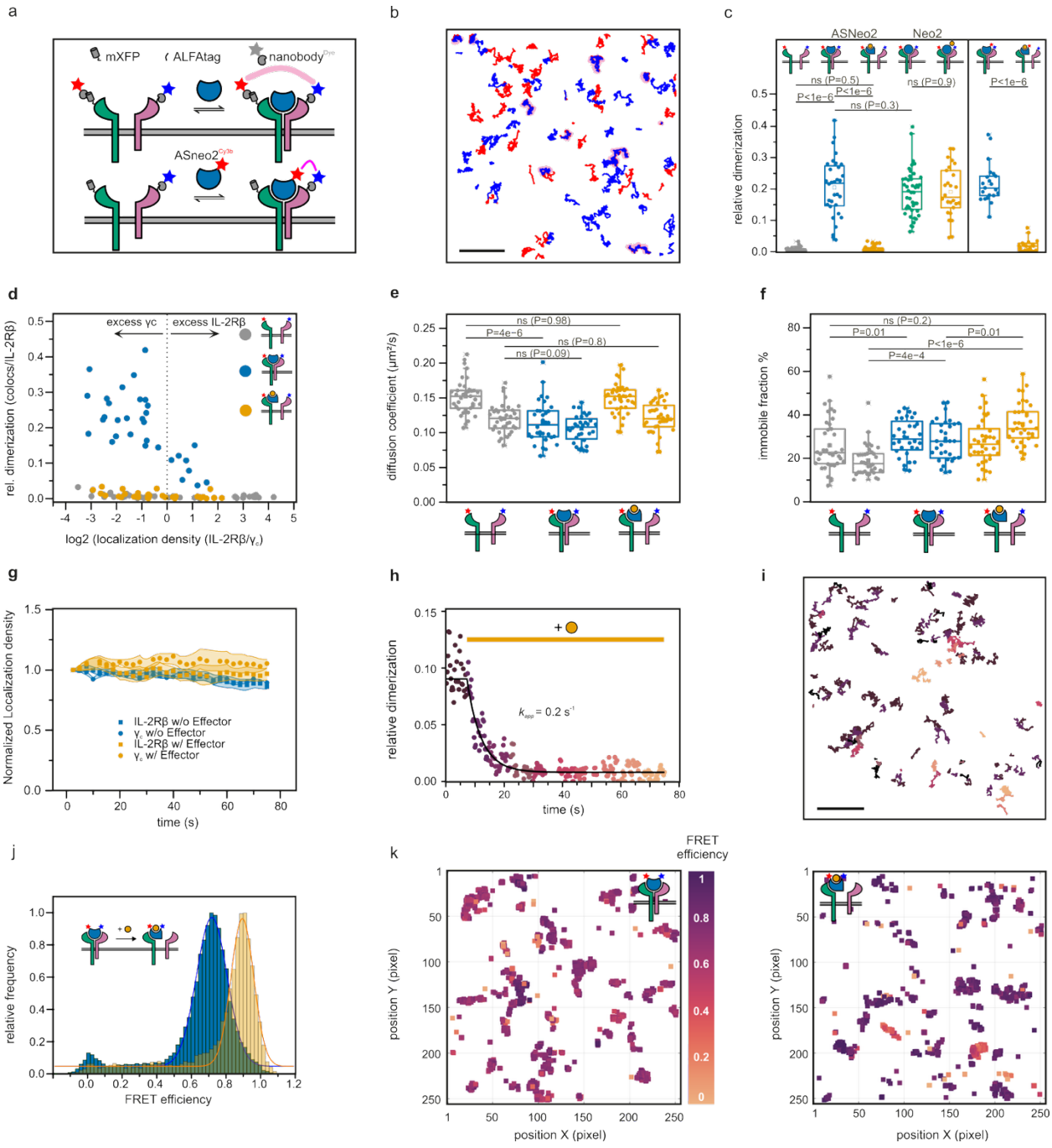

Extended Data Fig. 7: Detailed functional characterization of ASNeo2. **a**, Schematic depiction of labeling strategy for single molecule tracking experiments. **b**, Single molecule trajectories of IL-2Rβ (red), γ_c (blue) and ASNeo2-induced heterodimers (magenta). **c**, Data from Fig. 9e as boxplots to display datapoint variation including Neo2 (+/- effector) (green and orange, left side) and single molecule tracking experiments with labeled ASNeo2 and γ_c (right side). Sample sizes and independent repeats are: unstimulated: 37 and 3; ASNeo2: 32 and 3; ASNeo2 + Effector: 33 and 3; Neo2: 44 and 4; Neo2 + Effector: 26 and 2; labeled ASNeo2: 21 and 2; labeled ASNeo2 + Effector: 18 and 2. **d**, Relative dimerization in relation to receptor cell surface

density ratio indicates that high dimerization data variance is caused by differing IL-2Rβ to γ_c ratios at the plasma membrane. Even at high γ_c excess, effector-bound ASNeo2 shows no residual affinity for γ_c. **e**, Diffusion properties of IL-2Rβ and γ_c are reverted to the ground state after addition of effector. **f**, Immobile particles are increased upon stimulation, but not decreased after effector addition, potentially indicating receptors internalizing in membrane proximal endosomes. For e and f, the left box always corresponds to IL-2Rβ and the right one to γ_c. Sample sizes for d–f are as in **c**. **g**, Normalized localization density over time confirms minimal single molecule bleaching in long term single molecule tracking experiments. Sample sizes and independent repeats are: without Effector: 5 and 5; with Effector: 3 and 3. **h**, **i**, Dissociation of ASNeo2-induced IL-2Rβ/γ_c dimers at the cell surface upon addition of 10 μM effector as detected by time-lapse single-molecule co-tracking (h) with color-coded corresponding co-trajectories (i). **j**, **k**, Conformational change of ASNeo2 bound to the cell surface receptor probed by smFRET. **j**, FRET efficiency histograms for ASNeo2 E4C/K211C labeled with Cy3B and ATTO643 bound to cells expressing IL-2Rβ and γ_c in the absence (blue) and presence (yellow) of 10 μM effector. Sample sizes are: without Effector: 7; with Effector: 5. **h**, smFRET co-localizations of one individual cell before the effector was added (left) and after it was added (right) color-coded for FRET efficiency, highlighting the observation of individual molecules. Statistics for c, e and f were performed using two-sided two-sample Kolmogorov–Smirnov tests (ns “not significant,” p-values noted). Boxplots show the distribution of the dataset, highlighting the median, quartiles, and outliers, with whiskers extending to the range limits. Scale bar in b and i: 5 μm.

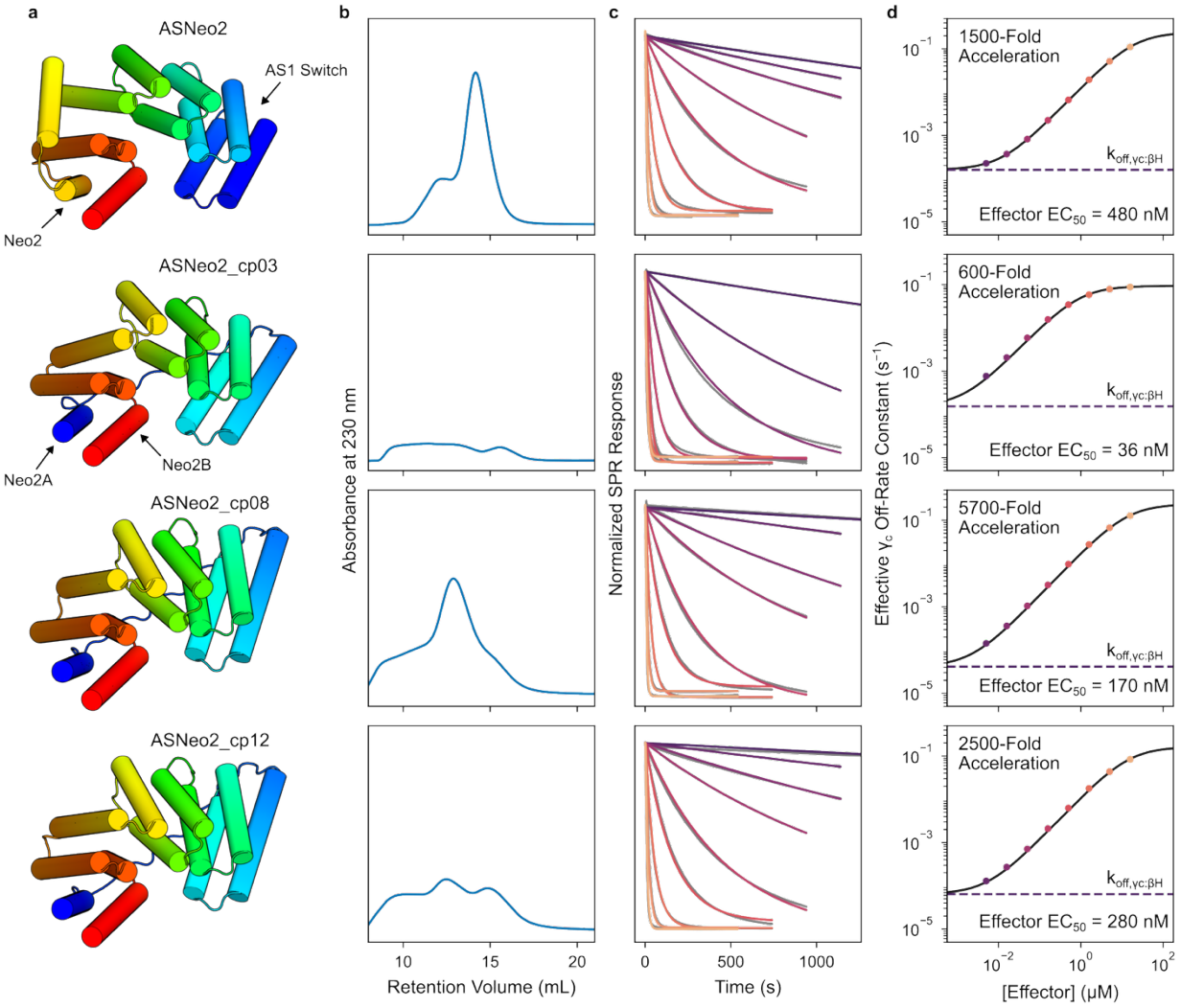

Extended Data Fig. 8: Characterization of cyclic permutations of ASNeo2. a, Design models of ASNeo2 and selected cyclic permutations in state X, rainbow-colored from N-terminus (blue) to C-terminus (red) to illustrate the protein topology. In ASNeo2, the switch is at the N-terminus and Neo2 is at the C-terminus. In the cyclic permutations, though the relative positions of the switch and Neo2 changes minimally, the switch is in the middle of the protein, part of Neo2 is at the N-terminus, and the other part is at the C-terminus. This way, the regulatory switch cannot degrade without also breaking Neo2. **b**, SEC purifications performed on a Superdex 200 Increase 10/300 GL column. The cyclic permutations are prone to aggregation during expression, but distinct monomer peaks can be picked out. **c**, Fast effector concentration–dependent dissociation of γ_c from the ASNeo2·IL-2Rβ·γ_c complex upon addition of peptide effector. Data (gray) fit (colors) as described in methods (neglecting the accumulation modeling because accumulation on the SPR surface was negligible with these proteins). **d**, Rate constants of facilitated γ_c dissociation computed from the model fit by ln(2)÷{half-time of γ_c:host interaction} plotted against effector concentration (circles) and fit with hyperbolic equations (black lines).

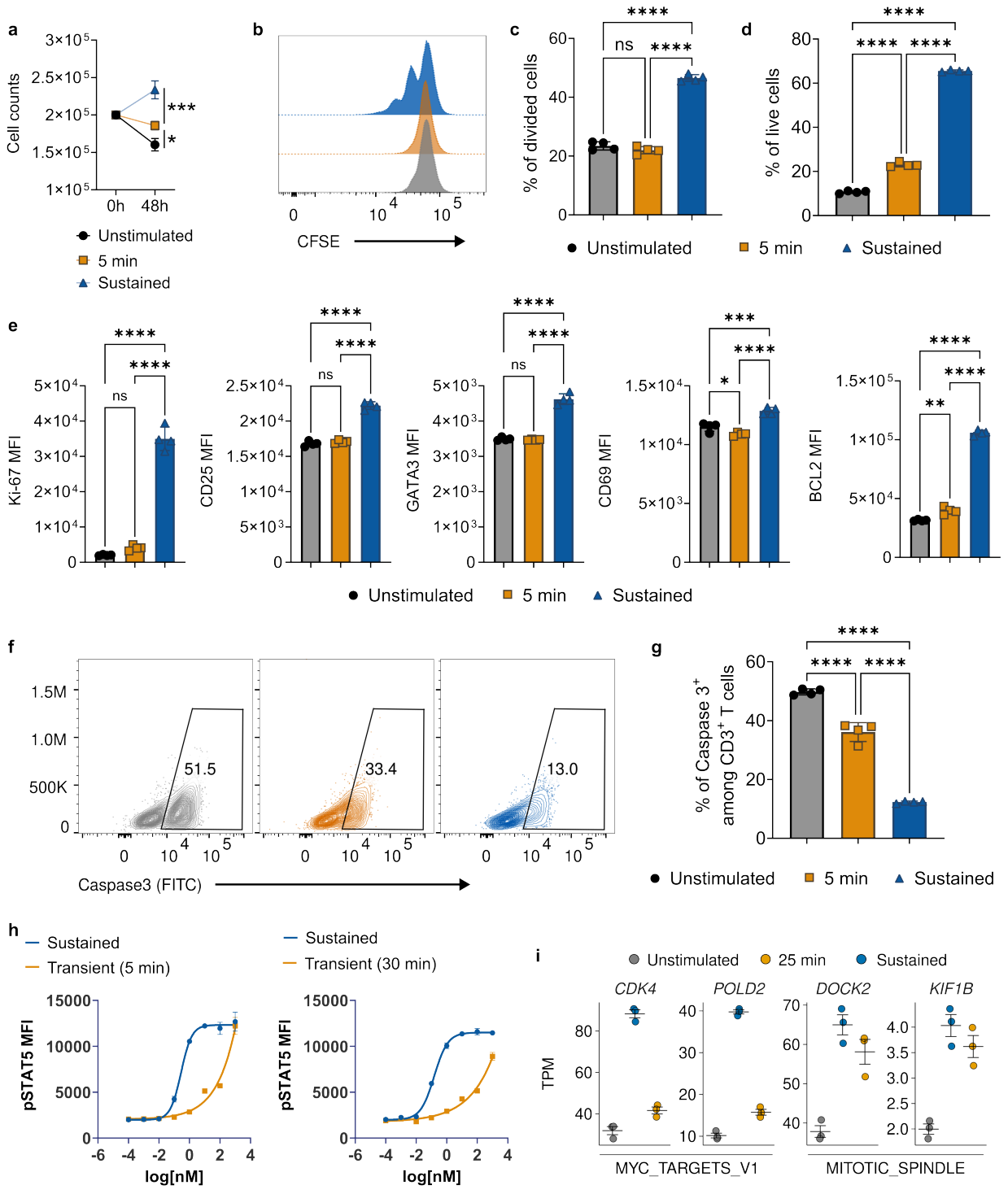

Extended Data Fig. 9: Additional characterization of differential effects of transient ASNeo2 stimulation on T cell behavior. Human T cells were stimulated with 1 nM (a–g) or 5 nM (i) ASNeo2 for 5 minutes (a–h), 30 minutes (h), or 25 minutes (i) or left untreated as a control. Signaling was either sustained by continued ASNeo2 treatment or terminated by the addition of 10 μM effector. Cells were collected for counting and phenotypic analysis by flow cytometry after

72 hours (b,c; n = 4) or 48 hours (a,e–g; n = 4), for pSTAT signaling analysis by flow cytometry after 20 minutes (h, n = 3), or for RNA-seq analysis after 6 hours (i, n = 3). **a**, Changes in viable T cell counts from 0 hours to 48 hours across each group. **b**, **c**, Representative flow cytometry histogram of CFSE (b) and quantitative analysis of divided cells (c). **d**, Frequencies of live T cells. **e**, Mean fluorescence intensity (MFI) of Ki-67, CD25, GATA3, CD69, and BCL2. **f**, **g**, Representative flow cytometry plots (f) and quantitative analysis of caspase-3+ cells (g, n=4). **h**, Dose-dependent pSTAT5 curves. **i**, Transcripts per million (TPM) of *CDK4* and *POLD2* in the MYC_TARGETS_V1 gene set (left); TPM of *DOCK2* and *KIF1B* in the MITOTIC_SPINDLE gene set (right). **a**, **c**–**e**, **g**, Statistics were obtained from ANOVA with two-sided Tukey's post-test (ns "not significant" ($p > 0.05$), * $p = 0.04$, ** $p = 0.001$, *** $p = 0.0002$, **** $p < 0.0001$). Lines or bars represent means; error bars represent SEM (a, h, i) or SD (c–e, g); n refers to biologically independent samples.

	AS1_H (PDB: 9DCX)	AS1_HE (PDB: 9DCY)	AS1_TH #1 (PDB: 9DCZ)	AS1_TH #2 (PDB: 9DD0)	AS1_THE #1 (PDB: 9DD1)
Data collection					
Space group	*P 61 2 2*	*P* 2_1	*P* 6_1 *2 2*	*P* 2_1 2_1 2_1	*P 43* 2_1 *2*
Cell dimensions					
a, *b*, *c* (Å)	61.54, 61.54, 236.10	78.44, 35.98, 88.90	80.71, 80.71, 546.85	62.98, 74.07, 211.77	110.85, 110.85, 65.53
α, β, γ (°)	90, 90, 120	90. 109.63, 90	90, 90, 120	90, 90, 90	90, 90, 90
Resolution (Å)	48.58 - 1.80 (1.85 - 1.80)	47.98 - 2.35 (2.47 - 2.35)	34.75 - 2.90 (2.94 - 2.90)	30.25 - 3.88 (4.34 - 3.88)	28.21 - 3.70 (3.93 - 3.70)
R_{sym} or R_{merge}	0.084 (0.945)	0.090 (0.221)	0.369 (2.128)	0.270 (0.717)	0.190 (0.951)
I / σI	22.53 (8.59)	8.70 (1.88)	10.5 (2.1)	5.80 (3.5)	10.70 (2.65)
Completeness (%)	99.31 (100.00)	99.66 (99.89)	99.90 (100)	99.80 (100.00)	100.00 (100.00)
Redundancy	12.7 (13.3)	4.8 (5.1)	31.4 (34.2)	9.6 (9.4)	11.8 (12.1)
Refinement					
Resolution (Å)	48.58 - 1.80 (1.85 - 1.80)	47.98 - 2.35 (2.47 - 2.35)	34.75 - 2.90 (2.94 - 2.90)	30.25 - 3.88 (4.34 - 3.88)	28.21 - 3.70 (3.93 - 3.70)
No. reflections	25499 (1764)	19956 (2831)	24845 (960)	9667 (1344)	4667 (756)
R_{work} / R_{free}	0.2135 (0.2862) / 0.2552 (0.3298)	0.1937 (0.2226) / 0.2437 (0.3186)	0.2094 (0.3779) / 0.2550 (0.4580)	0.2261 (0.2743) / 0.2789 (0.3296)	0.2472 (0.3015) / 0.2772 (0.3010)
No. atoms					
Protein	1965	4340	6010	5891	3062
Ligand/ion	n/a	n/a	n/a	n/a	n/a
Water	92	59	7	n/a	n/a
B-factors					
Protein	38	42	84	115	92
Ligand/ion	n/a	n/a	n/a	n/a	n/a
Water	44	37	56	n/a	n/a
R.m.s. deviations					
Bond lengths (Å)	0.008	0.001	0.003	0.003	0.002
Bond angles (°)	0.81	0.34	0.52	0.53	0.40

	AS5_H (PDB: 9DD2)	AS5_HE (PDB: 9DD3)	LHD101An1 (PDB: 9DD4)	CS221B (PDB: 9DD5)	AS1_THE #2 (PDB: 9OLQ)
Data collection					
Space group	*P 43*	*C 2*	*P* 2_1 2_1 2_1	*C 2*	*C 2*
Cell dimensions					
a, *b*, *c* (Å)	62.37, 62.37, 78.50	90.17, 35.66, 75.52	64.97, 70.66, 76.39	54.67, 25.09, 34.67	285.58, 96.40, 74.69
α, β, γ (°)	90, 90, 90	90, 116.2, 90	90, 90, 90	90, 102.77, 90	90, 90.39, 90
Resolution (Å)	48.84 - 1.72 (1.75 - 1.72)	31.69 - 1.64 (1.68 - 1.64)	51.88 - 2.11 (2.17 - 2.11)	33.81 - 1.5 (1.62 - 1.50)	41.16 - 3.48 (3.67 - 3.48)
R_{sym} or R_{merge}	0.047 (0.709)	0.062 (0.537)	0.037 (0.911)	0.060 (0.788)	0.316 (2.305)
I / σI	18.50 (2.2)	6.62 (1.14)	21.25 (1.80)	12.57 (1.71)	4.9 (1.2)
Completeness (%)	100.00 (100.00)	91.01 (95.00)	99.63 (99.82)	99.71 (99.38)	99.6 (99.4)
Redundancy	9.0 (9.2)	1.9 (1.9)	6.4 (6.5)	6.7 (6.8)	6.9 (7.1)
Refinement					
Resolution (Å)	48.84 - 1.72 (1.75 - 1.72)	31.69 - 1.64 (1.68 - 1.64)	51.88 - 2.11 (2.17 - 2.11)	33.81 - 1.5 (1.62 - 1.50)	41.16 - 3.48 (3.57 - 3.48)
No. reflections	31945 (2281)	24347 (1919)	20777 (1711)	7489 (1451)	25996 (1868)
R_{work} / R_{free}	0.2035 (0.2755) / 0.2431 (0.3195)	0.2018 (0.3285) / 0.2509 (0.3520)	0.2222 (0.3295) / 0.2617 (0.3301)	0.2091 (0.2512) / 0.2494 (0.3124)	0.2475 (0.3276) / 0.2871 (0.3802)
No. atoms					
Protein	2001	2149	1976	430	15510
Ligand/ion	n/a	n/a	n/a	n/a	n/a
Water	125	70	16	45	n/a
B-factors					
Protein	40	35	80	31	111
Ligand/ion	n/a	n/a	n/a	n/a	n/a
Water	46	41	69	46	n/a
R.m.s. deviations					
Bond lengths (Å)	0.006	0.003	0.002	0.004	0.002
Bond angles (°)	0.68	0.53	0.35	0.60	0.40

Extended Data Table 1 | Crystallographic data collection and refinement. Values in parentheses are for highest-resolution shell.

Supplementary Information

Supplementary Note 1 | Nomenclature

“Host” refers to the switch-binder fusion with allosterically coupled target and effector binding sites.

“Target” refers to the protein that binds tightly to the host but can be rapidly induced to dissociate.

“Effector” refers to the protein/peptide that binds to the host at a different site to cause a conformational change in the host that destabilizes target binding.

“Binder” refers to the component of the host designed to bind to the target.

“Switch” refers specifically to the effector-responsive conformational switch component of the host proteins, and we avoid using “switch” to refer to the entire host protein. This way, we distinguish between designing switches (multi-state design) and designing hosts (fusing switches to binders).

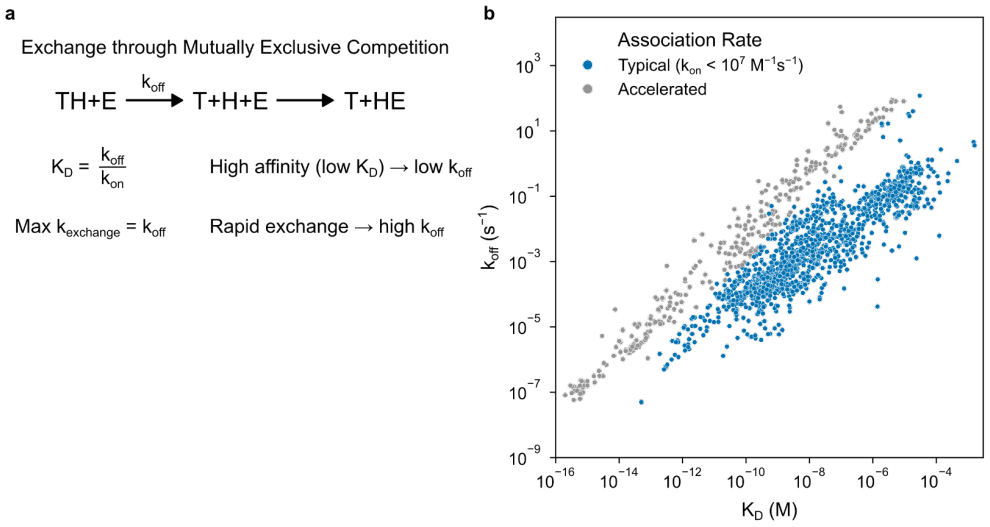

Supplementary Figure 1 | Relationship between affinity and exchange rate. a, For protein-protein interactions with typical diffusion-limited association rates in the 10^5–10^6 $M^{-1}s^{-1}$ range, high affinity (K_D < 1 nM) requires low off-rates (k_{off} < 10^{-3} s^{-1}). This precludes rapid exchange through mutually exclusive competition, which requires high off-rates. **b**, Off-rate constant vs affinity for a set of natural and mutant proteins with typical on-rates (blue) and high on-rates (gray) depicting this tradeoff. Data obtained from the SKEMPI database[102].

High affinity and rapid exchange could be simultaneously achieved in binary interactions with high on-rates (k_{on} > 10^7 $M^{-1}s^{-1}$)[103], but these are usually caused by long-range electrostatic attraction and are not a general feature of protein-protein interactions. Although electrostatically accelerated association has been engineered into proteins[104], this is not possible in general with native targets because it requires patches of complementary surface charge on both binding partners.

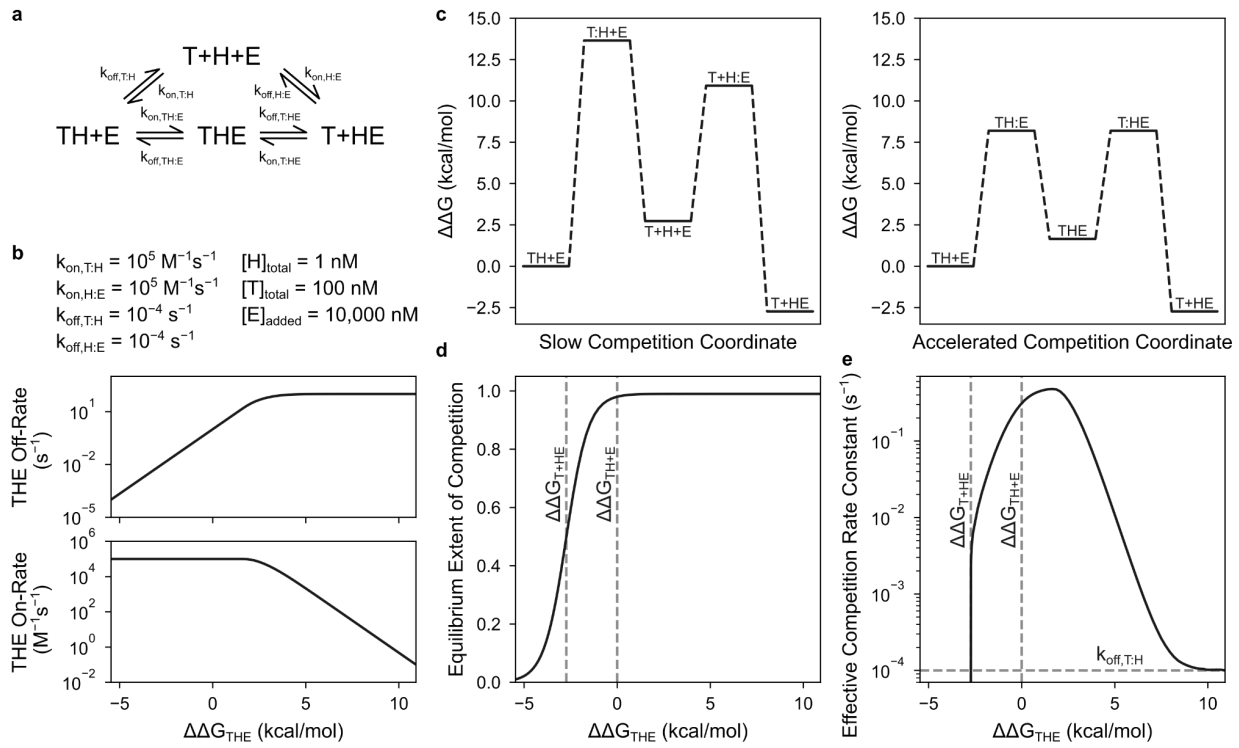

Supplementary Figure 2 | Dependence of facilitated dissociation on the energy of the ternary intermediate. a, Kinetic model of a facilitated dissociation system. We modeled the dynamics of a facilitated dissociation process for a range of ternary intermediate energies, simulated in this model by pre-equilibrating H and T then adding excess E. **b**, Model parameters used to simulate facilitated dissociation. We fixed the binary interaction rate constants, and we varied the ternary interaction rate constants to set the ternary intermediate energy. The plots show the relationships we chose between the ternary intermediate energy and the ternary interaction rate constants. These hold with physical intuition: low to moderate increases in ternary intermediate energy primarily affect dissociation rates, whereas high increases in ternary intermediate energy additionally affect association rates. **c**, Energy diagrams of slow mutually exclusive competition (left) and facilitated dissociation (right). Colons denote binding transition states between components. Binding E reduces the energy of the entire system, including the T dissociation transition state. Frustration between T and E causes the ternary intermediate energy to reduce less, lowering the barrier for T dissociation. **d**, Dependence of the equilibrium extent of the competition reaction on the ternary intermediate energy. If the ternary intermediate energy is too low (too little strain), the ternary complex becomes the dominant equilibrium state and T dissociation is not favored. **e**, Dependence of the competition rate constant on the ternary intermediate energy. The effective rate is defined as ln(2)÷{time to 50% extent of reaction} (this is undefined when $\Delta\Delta G_{THE} < \Delta\Delta G_{T+HE}$ because the final extent of reaction is less than 50%). The rate of competition peaks at an optimal ternary intermediate energy, then recedes to the basal rate of mutually exclusive competition as the ternary intermediate becomes increasingly energetically inaccessible.

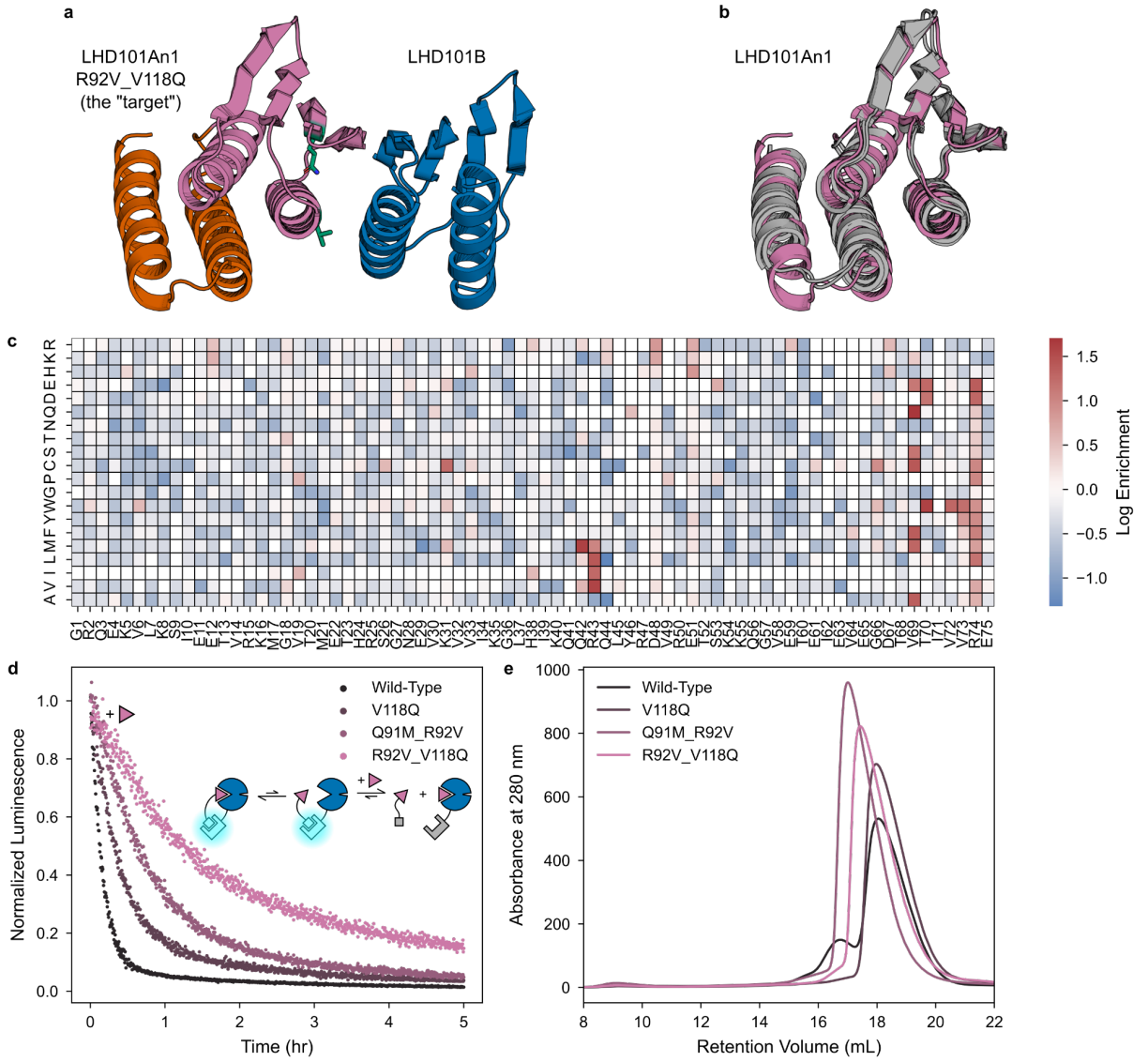

Supplementary Figure 3 | Design and characterization of the target. a, Design models of the target (pink/red) and binder (blue) in complex. Starting from LHD101A (pink), we built additional structure (red) to increase opportunities for steric clashing, resulting in the target protein "LHD101An1." Unless otherwise stated, "target" refers to LHD101An1 with affinity-enhancing mutations R92V and V118Q (green). **b**, Crystal structures of LHD101An1 (gray) overlaid with the design model (pink). **c**, Site-saturation mutagenesis heatmap showing the enrichment over wild-type of each LHD101A point mutation displayed on yeast sorted against 10 nM LHD101B. Mutations Q42M, R43V, and V69Q on LHD101A correspond to Q91M, R92V, and V118Q on LHD101An1. **d**, Dissociation time courses of preincubated 20 nM LHD101An1-SmBiT mutants and 100 pM AS0-LgBiT after adding 20 μM LHD101An1 competitor, showing the double mutant R92V V118Q especially reduces the intrinsic target-host off-rate. **e**, SEC purification runs of LHD101An1 mutants, performed on a Superdex 200 Increase 10/300 GL column with injection concentrations greater than 500 μM, showing these mutants remain well-behaved in solution.

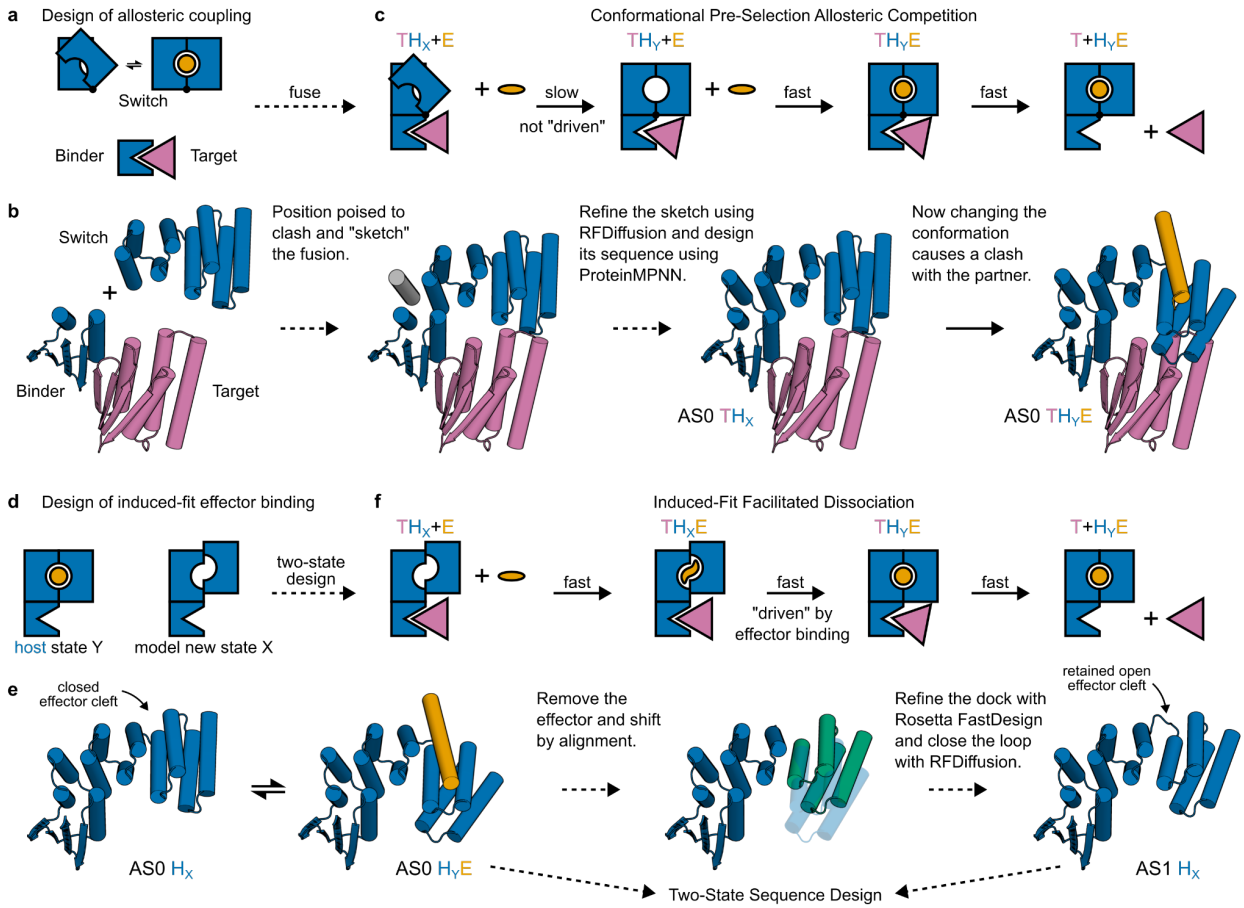

Supplementary Figure 4 | Approach to designing facilitated dissociation systems. a, **b**, Approach to designing host proteins by fusing a target binder and an effector-responsive switch. **a**, Cartoons of the starting components (a previously designed hinge switch and binder-target pair). **b**, Structural models showing how the switch and binder were fused to construct the first generation of hosts (including AS0). **c**, Cartoons showing the expected mechanism of competition, rate-limited by hinge opening. **d**, **e**, Approach to designing register-shift host proteins that retain an open cleft in state X. **d**, Cartoons of the register-shift hosts (AS0 state Y and a new state X with an open cleft). **e**, Structural models showing how the new state X was modeled from the state Y of AS0 to construct the second generation of hosts (including AS1). **f**, Cartoons showing the expected mechanism of competition, with a conformational change driven by effector binding.

The closed state X of the original hinge blocks effector binding, so the hinge must change conformation before the effector can bind: a conformational selection mechanism. In the absence of pre-existing conformational fluctuations of the target, spontaneous hinge opening against the target will generally be slow. The open state X of the new switches could allow weak effector binding that triggers the conformational change: an induced-fit mechanism. Our two-state design process generates sequences for the switch considering the state X alone and the effector-bound state Y. Thus, the switch is only designed to make strong interactions with the effector when in state Y, causing effector binding to promote the register shift to state Y.

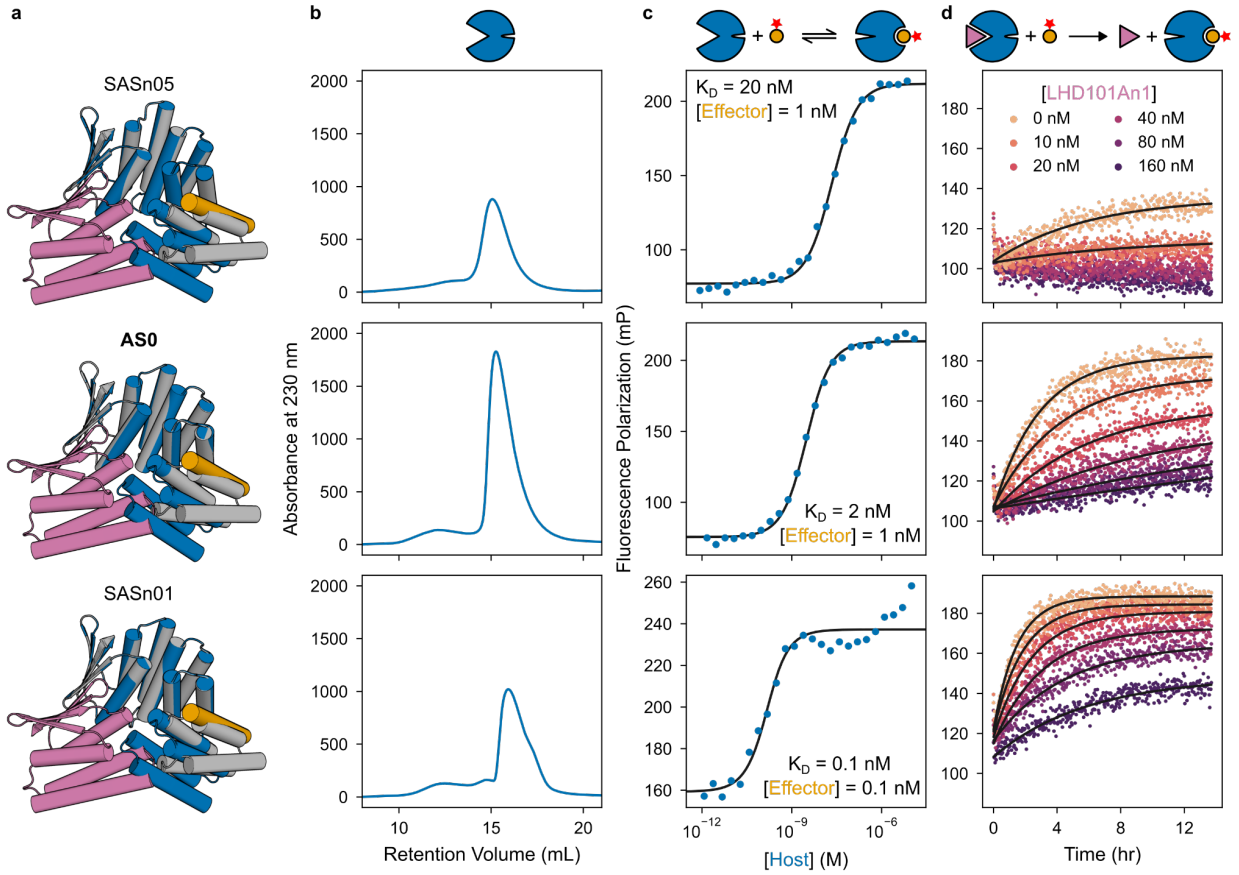

Supplementary Figure 5 | Negative allosteric coupling between target and effector. a, Design models of selected hinge-based host-effector complexes in state Y (blue and orange) aligned to the target (pink) and to the host in state X (gray). **c**, SEC host purifications performed on a Superdex 200 Increase 10/300 GL column. **d**, Fluorescence polarization (FP) titrations with a constant concentration of TAMRA-labeled effector and varying host concentrations. Data (blue) fit with a standard binding isotherm (black). **e**, Association of 20 nM TAMRA-labeled effector to 20 nM host against varying concentrations of the target LHD101An1, showing competition between target and effector binding. FP data (colors) fit with single exponentials (black).

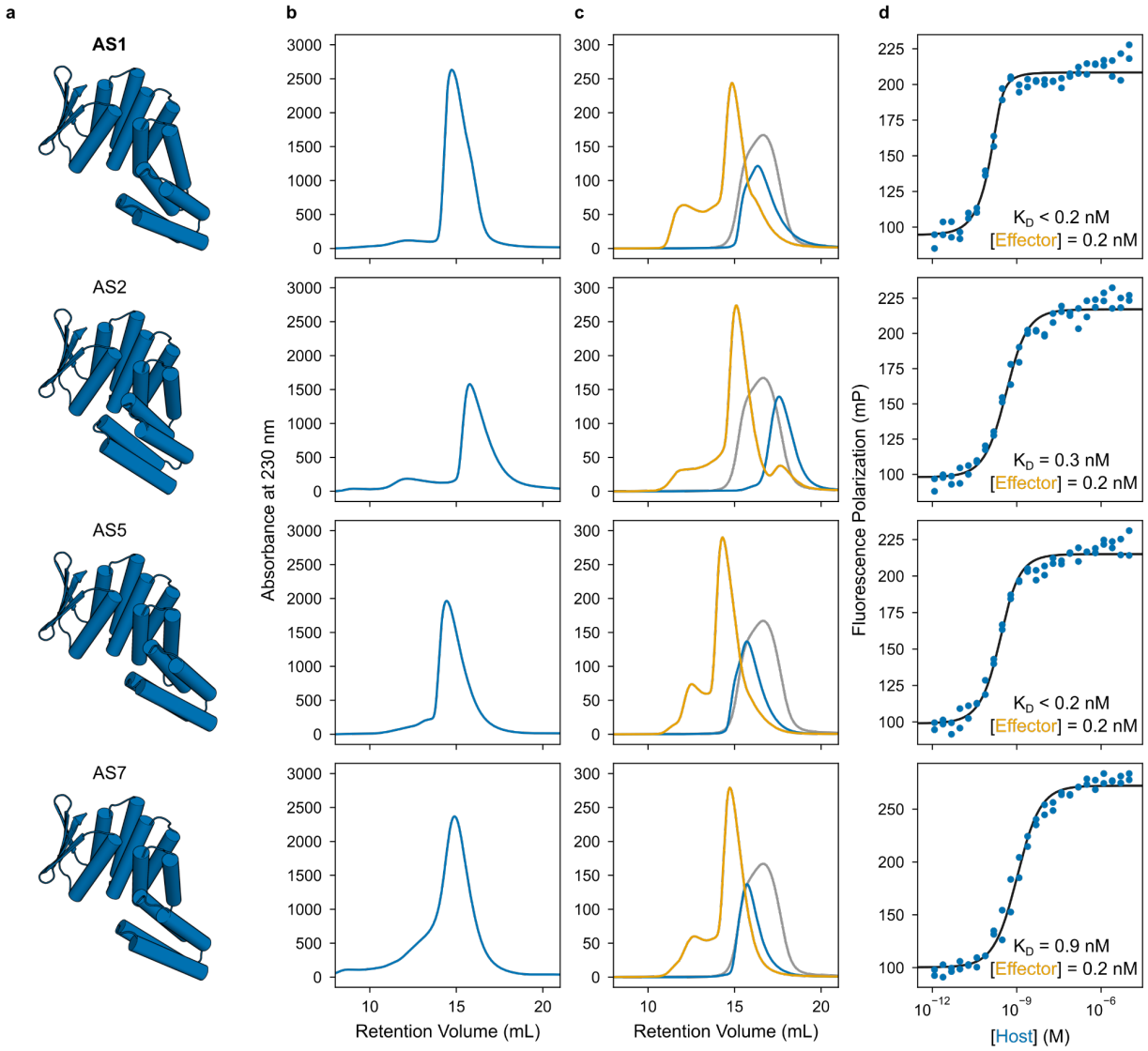

Supplementary Figure 6 | Initial characterization of register-shift host designs. a, Design models of selected register-shift host proteins in state X, showing the diversity of the new state X. **b**, SEC host purifications performed on a Superdex 200 Increase 10/300 GL column. **c**, SEC binding experiments performed on a Superdex 200 Increase 10/300 GL column. All components were injected at 20 μM. The mixtures of host and sfGFP-tagged effector (orange) run larger than the hosts alone (blue) or sfGFP-effector alone (gray), indicating host-effector binding. **d**, FP titrations with a constant concentration of TAMRA-labeled effector and varying host concentrations. Data (blue) fit with a standard binding isotherm (black).

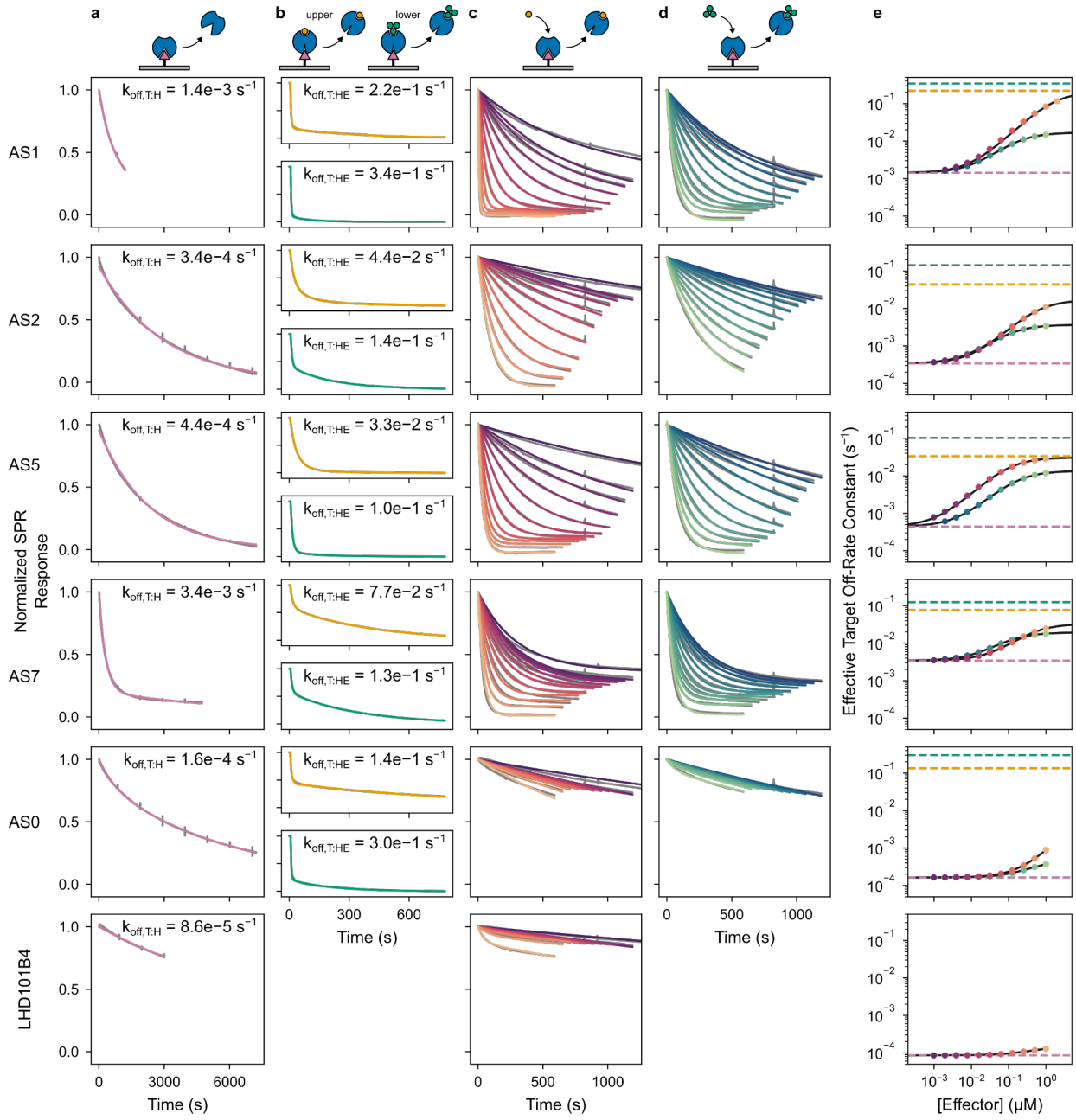

Supplementary Figure 7 | SPR characterization of facilitated dissociation in host designs. **a**, Slow dissociation of the target from the host in the absence of effector. Data (gray) fit with exponential decay functions (pink). For AS2 and AS5, single exponentials were used, whereas for the other designs, double exponentials were used to account for populations of host protein with different dissociation kinetics. For the double exponential fits, the reported dissociation rate constant, $k_{off,T:H}$, is the rate constant from the higher amplitude exponential in the fit. **b**, Faster dissociation of the target from the ternary complex with effector. In each row, the top plot corresponds to the peptide effector and the bottom plot to the 3hb effector. Data (gray) fit with double exponential decay functions (orange for peptide, green for 3hb) to account for a population of target-host complex lacking the effector. The reported dissociation rate constant,

$k_{off,T:HE}$, is the higher of the two rate constants in the fit. **c** and **d**, Effector concentration–dependent dissociation of the target upon addition of peptide (c) or 3hb (d) effector. Data (gray) fit (colors) as described in methods. **e**, Effective target off-rate constants computed from the model fit by ln(2)÷{half-time of target-host interaction} plotted against effector concentration (circles) and fit with hyperbolic equations (black lines). The orange circles correspond to the data with peptide effector from (c) and the green circles to the data with 3hb effector from (d). The pink line plots $k_{off,T:H}$ measured in (a), the orange line plots $k_{off,T:HE}$ with peptide effector measured in (b), and the green line plots $k_{off,T:HE}$ with 3hb effector measured in (b). With the peptide effector, the effective rate of the full facilitated dissociation pathway approaches the rate of target dissociation from the ternary intermediate, whereas with the 3hb effector, the effective rate of the full facilitated dissociation pathway approaches a lower value. As observed for AS1 (Fig. 6), this likely corresponds to peptide binding through induced-fit and 3hb binding rate-limited by a slower conformational selection. Once the effector is bound, however, the more deformable peptide less effectively strains the target interface (the target off-rate from the ternary complex is generally higher with the rigid 3hb than with the peptide) (Supplementary Table 2). At the top of **a**–**d**, cartoons show the arrangement of proteins relative to the SPR chip (gray). Only the experiments of panels (a) and (c) were performed for the LHD101B4 control. Also note that the data in gray is often hidden behind the colored fit curves.

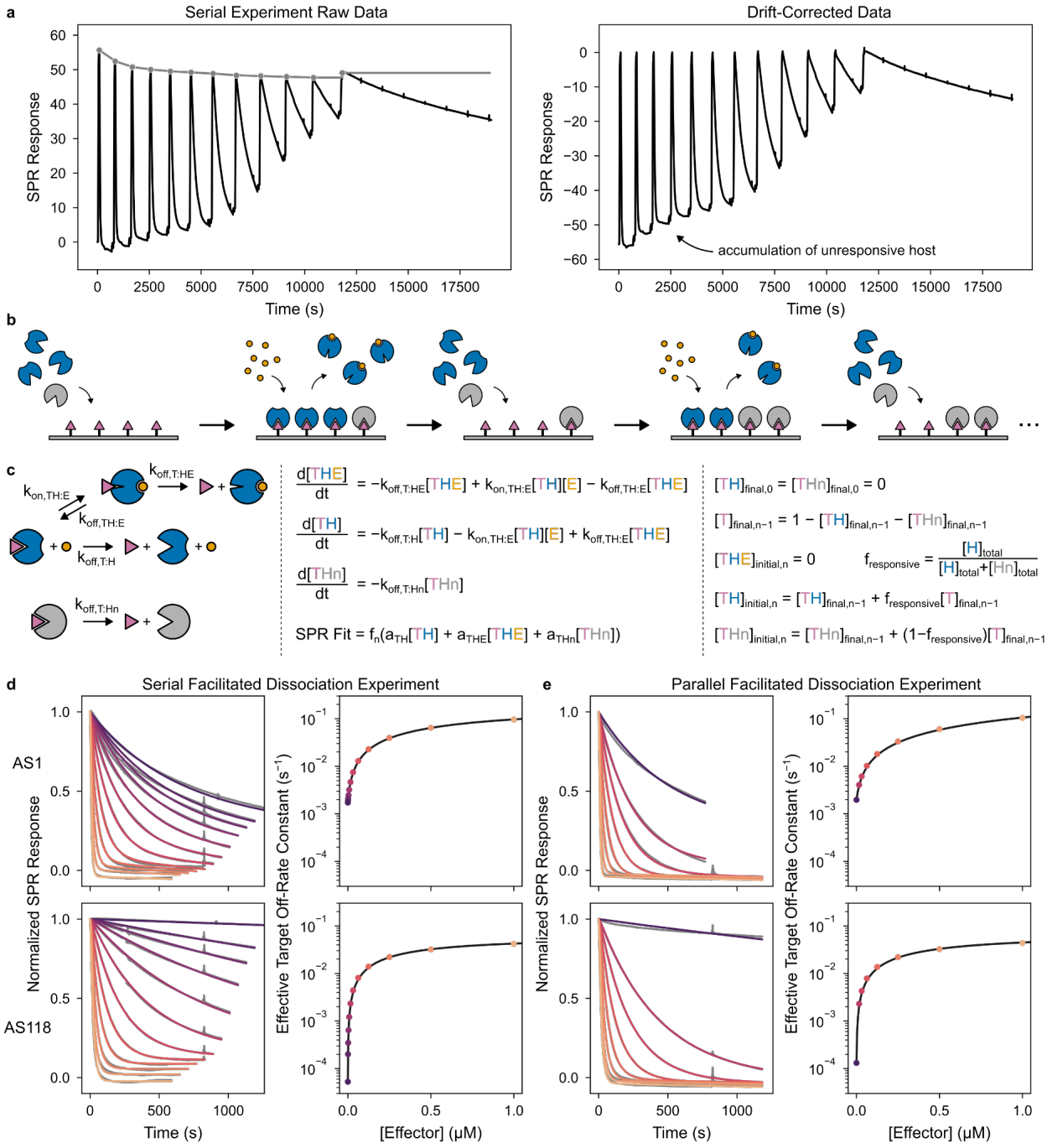

Supplementary Figure 8 | Fitting SPR facilitated dissociation data. a, (Left) raw SPR data (black) of a serial facilitated dissociation experiment involving multiple cycles of associating host then dissociating it with varying concentrations of effector. (Gray) approximate baseline drift estimated by interpolating between the peaks of host association (the SPR response should be the same when the surface is saturated with host). (Right) SPR data corrected for baseline drift by subtracting the gray baseline approximation from the raw SPR data. After each cycle, the dissociation trace plateaus at increasingly higher SPR response values, likely corresponding to accumulation of a small population of host that is unresponsive to the effector—this could be

due to partial degradation or misfolding induced by the strain in the ternary complex. **b**, Cartoons showing how a small population of unresponsive host (gray, “Hn”) will accumulate on the surface after multiple facilitated dissociation cycles. **c**, Kinetic model fit to the facilitated dissociation experiment (see methods). (Left) cartoons depicting the state transitions that would affect the SPR response. (Middle) The system of differential equations corresponding to the kinetic model on the left, which can be fitted to the dissociation curve of each cycle. The bottom equation relates the concentrations of each state on the SPR surface to an SPR response. (Right) initial values for fitting this model to the dissociation curve of cycle *n*. **d** and **e**, (Left) fit data from serial (d) or parallel (e) facilitated dissociation experiments on AS1 (top row) or AS118 (bottom row). Data shown in gray and fits in colors. In the parallel facilitated dissociation experiment, each effector concentration is tested on a fresh SPR surface, minimizing accumulation of unresponsive host. Not needing to account for this, the model used to fit parallel facilitated dissociation data can be simpler. (Right) Effective target off-rate constants computed from the model fit by ln(2)÷{half-time of target-host interaction} plotted against effector concentration (circles, colors correspond to the fit dissociation traces in the left plots) and fit with a hyperbolic equation (black line). The target dissociation kinetics obtained from fitting the serial and parallel facilitated dissociation experiments agree within 4-fold, indicating that the serial experiment provides fairly accurate measurements of the target dissociation kinetics despite requiring a more complex model to fit.

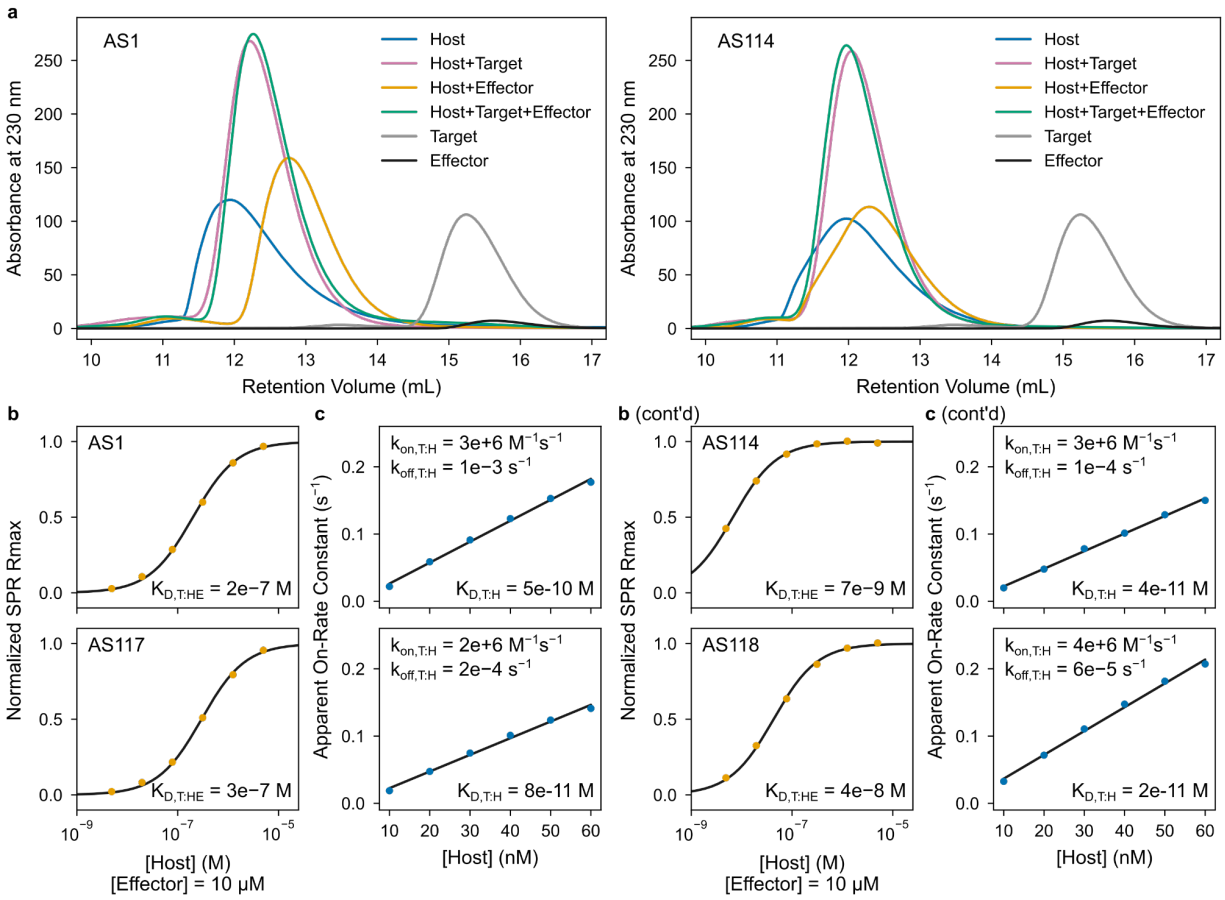

Supplementary Figure 9 | Stability of the AS1 and AS114 ternary complexes at high concentration. a, SEC binding experiments performed on a Superdex 75 Increase 10/300 GL column. All components were injected at 20 μM. In isolation, the target (gray) and effector (black) elute around 15–16 mL. When the host is included, depletion of signal in this range indicates target-host or host-effector binding. The hosts alone (blue) run large and are likely weak homodimers. Including either target (pink) or effector (orange) reduces homodimerization so the complex elutes later; signal past 15 mL is fully depleted, indicating complete binding to the host. Including both target and effector (green) near-fully (for AS1) or fully (for AS114) depletes signal past 15 mL, indicating both target and effector are bound to the host. For the AS1 ternary complex, the target was likely completely bound at the time of injection, but since the target dissociates from AS1 20-fold faster than from AS114 (Fig. 8a), some target dissociated while on the column, leaving the long tail extending past 15 mL. Thus, when both target and effector are present at sufficiently high concentrations, the ternary complex is the dominant state. **b** and **c**, Affinity measurements of the target binding the host-effector complex (b) and the host alone (c). **b**, Maximum response values with titrated host (preincubated with excess effector) plotted against host concentration. Data (points) fit with a standard binding isotherm. **c**, Apparent target:host on-rate constants vs. host concentration with a linear fit. The affinity is calculated as the ratio of the target:host off-rate constant (Fig. 6, Supplementary Fig. 11) and the on-rate constant from the fit.

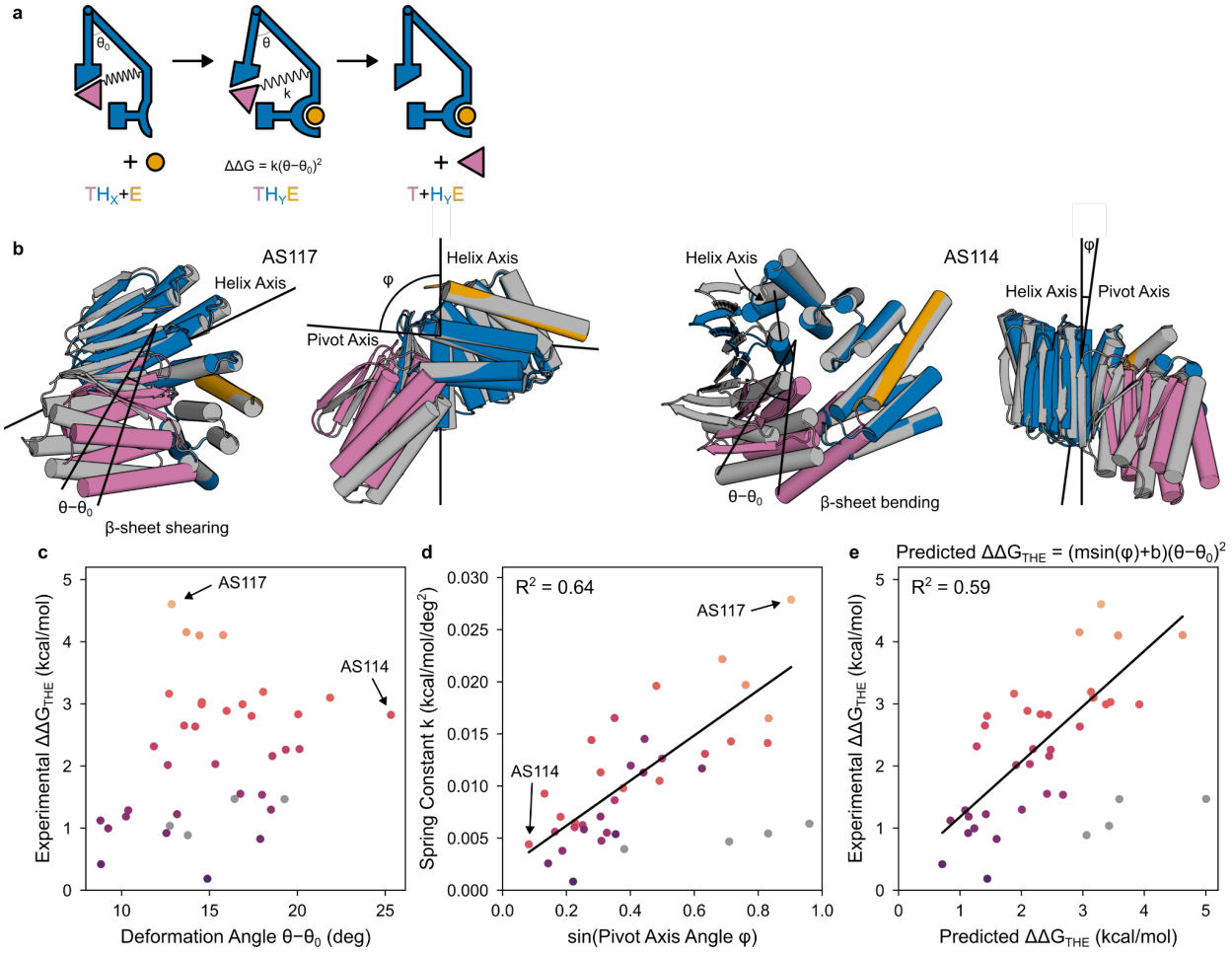

Supplementary Figure 10 | Modeling strain energy in the ternary complex. AF2 predicts AS1 and the fast variants like AS117 to globally deform in different directions from slower designs like AS114. Using a simple coarse-grained model based on the predicted magnitude and direction of the deformation relative to the secondary structure elements in the binder interface, across almost all designs, the predicted strain energy favoring partner dissociation correlates (R^2 = 0.59) with the strain energy estimated from the observed rate enhancement. Pearson's R^2 is calculated from linear least-squares regression.

a, Schematic of structural frustration resolved through strain in a facilitated dissociation pathway. Hooke's law can relate the energy of the ternary intermediate to mechanical properties of the protein.

b, Differences in ternary complex geometry for the fastest AS1 variant (AS117, left) and a slower variant that yet deforms more in the ternary complex (AS114, right). Design models of host·effector complex in state Y (blue and orange) aligned to the target (pink) showing the allosteric clash, and (gray) AF2 predictions of the ternary complex aligned to the switch showing how the clash resolves through global strain. To model the strain energy from these structures using Hooke's law, we measured the global deformation by the angle (θ–θ_0) the target pivots

around some axis (the "pivot axis") to move from its clashing position to its AF2-predicted strained position. The binder helix in the interface with the target tends to be positioned near the centerpoint of the deformation (the point around which the centroid of the target pivots), and the structure of this helix is the same for all variants, so we used the axis of this helix (the "helix axis") to approximate the orientation of the deforming secondary structure elements. For each variant shown, the left view places the pivot of the target within the plane of the page (so the pivot axis is normal to the page), and the right view places the helix axis and the pivot axis both within the plane of the page. In the left view, lines are drawn from the pivot axis through the centroids of the clashing and strained targets; the angle between these lines is the angle of global deformation ($\theta-\theta_0$). The right view shows the angle between the helix axis and the pivot axis (ϕ); this is large for the fast variant and small for the slow but highly deforming variant.

c, Lack of correlation between predicted magnitude of deformation and the experimental strain energy of the ternary complex for a set of host designs (AS1, AS2, AS5, AS7, and the AS1 variants, plotted as circles colored by their experimental strain energy except for AS101, AS115, AS119, and AS120 which were left out of the analysis in (c) and (d) and are colored gray—34 designs in total). The strain energy can be estimated from the observed accelerated off-rate constant as follows.

$$Experimental\ \Delta\Delta G_{THE} = RT\ ln\frac{K_{D,T:HE}}{K_{D,T:H,unstrained}} = RT\ ln\frac{k_{off,T:HE}k_{on,T:H,unstrained}}{k_{off,T:H,unstrained}k_{on,T:HE}}$$

Making the approximation that $k_{on,T:HE} = k_{on,T:H,unstrained}$ and does not vary with $\Delta\Delta G_{THE}$ (Supplementary Fig. 2) simplifies this expression.

$$Experimental\ \Delta\Delta G_{THE} = RT\ ln\frac{k_{off,T:HE}}{k_{off,T:H,unstrained}}$$

The accelerated off-rate constant $k_{off,T:HE}$ is assumed to be the maximum off-rate constant observed in the facilitated dissociation experiments (Supplementary Fig. 11). Since the main target-binder interface does not change across variants, the off-rate constant of the unstrained interface $k_{off,T:H,unstrained}$ should be a constant, k_{base}, with one exception: in some variants, the switch fusion may form additional stabilizing interactions with the target, reducing the base off-rate constant $k_{off,T:H}$ (also measured in the facilitated dissociation experiments). These interactions can likely still form in the strained ternary complex to reduce the accelerated off-rate constant $k_{off,T:HE}$ by the same factor. Thus, the smaller of k_{base} and $k_{off,T:H}$ is used for $k_{off,T:H,unstrained}$. For k_{base}, a value of 2e–4 s^{-1} was used because it gave the best correlation between predicted and experimental $\Delta\Delta G_{THE}$ described in panel (d). Notably, this value is quite close to the target off-rate constant from the unhindered binder fusion LHD101B4, 9e–5 s^{-1} (Supplementary Fig. 7).

d, Linear correlation between the "spring constant" k (which relates the experimental strain energy to the magnitude of the predicted deformation) and the perpendicularity of this deformation to the secondary structure elements in the complex for this set of host designs

(circles colored as in (b)). A linear regression on the colored points is plotted as a black line. The perpendicularity is computed as the sine of the angle between the pivot axis and the helix axis, and the spring constant is computed using Hooke's Law as follows.

$$Spring\ Constant\ k = \frac{\Delta\Delta G_{THE}}{(\theta - \theta_0)^2}$$

This relationship suggests that deforming in a stiff direction (against rather than around helices[44]) deforms the target interface in a more destabilizing direction or better localizes strain to the target interface instead of distributing the strain throughout the entire protein.

e, Agreement between the experimental strain energy and the strain energy estimated entirely from the predicted structure of the strained ternary complex using Hooke's Law for this set of host designs (circles colored as in (b)). A linear regression on the colored points is plotted as a black line. The spring constant was assumed to depend linearly on the deformation perpendicularity to the secondary structure elements, and the parameters of this correlation (m and b) were varied to fit the following expression to the experimental strain energies.

$$Predicted\ \Delta\Delta G_{THE} = (m\ sin(\varphi) + b)(\theta - \theta_0)^2$$

Sources of Error in this Analysis

First, in this simple energetic model of facilitated dissociation described here and in Supplementary Fig. 2, when the effector binds, the energy of the target dissociation transition state will decrease by the binding energy of the effector. When the effector and target are uncoupled, the energy of the ternary complex intermediate will decrease by the same amount so the activation barrier for target dissociation will not change. When strain between the target and effector is incorporated into the ternary intermediate, its energy will decrease less upon effector binding, reducing the activation barrier for target dissociation. This simple energetic model thus assumes that the activation barrier for target dissociation is directly related to the global energy of the ternary complex. In reality, acceleration of target dissociation will arise from local deformation at the target interface[35]. Thus, put differently, the simple energetic model assumes that the global deformation is smoothly distributed across the entire protein. This assumption allows us to directly relate the global deformation predicted by AF2 to the local deformation at the target interface measured by the accelerated target off-rate. In reality, the deformation is likely not smoothly distributed, and this may at least partially explain the imperfect correlation between the predicted and experimental strain energy of the ternary complex. This is exemplified by how the target dissociates more slowly from the AS1 ternary complex with the peptide effector than with the 3hb effector (Fig. 6e,f). Despite forming the same interactions and causing the same conformational change as the 3hb, the more deformable peptide appears to less effectively localize strain to the target once in the ternary complex. Uneven distribution of strain in the ternary complex is also one possible mechanism underlying unidirectional competition in facilitated dissociation systems.

Second, our model estimating the protein stiffness anisotropy using the orientation of the secondary structure elements is likely oversimplified. Proteins have finer levels of structure than the orientation of their secondary structure elements. Much like a normal mode analysis, a more sophisticated model could estimate local spring constants for smaller regions of the protein, then compute a strain energy for each region from its predicted deformation.

Third, inaccuracies in the AF2 predictions of the strained ternary complex could cause much of the variation between the experimental and predicted strain energies. Clear cases of this, variants AS101, AS115, AS119, and AS120 (gray) which do not follow this correlation were left out of this analysis. We hypothesize that these variants can adopt an alternate, less-strained ternary complex conformation than the high-energy conformation predicted by AF2.

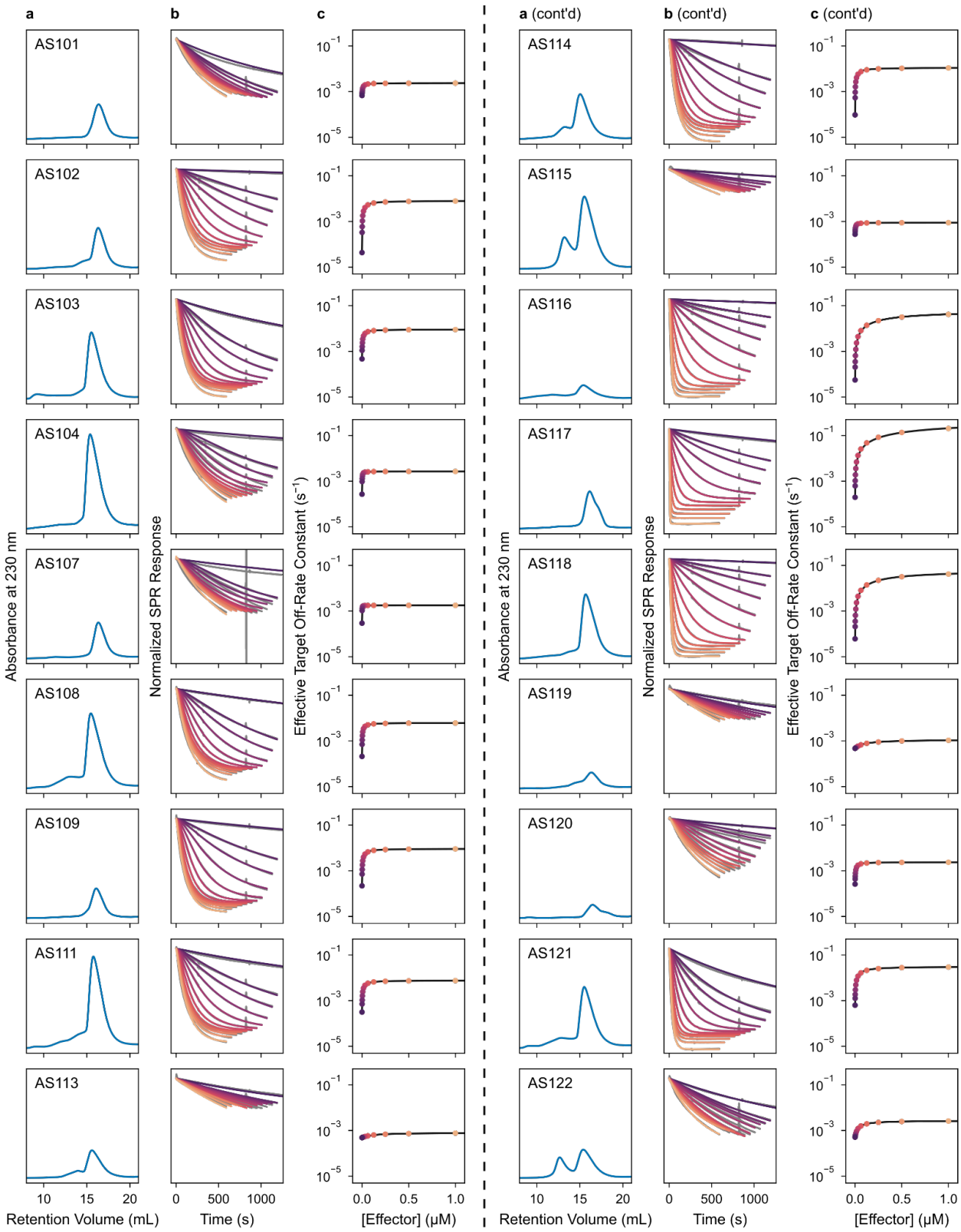
a
b
c
a (cont'd)
b (cont'd)
c (cont'd)
AS101
AS102
AS103
AS104
AS107
AS108
AS109
AS111
AS113
AS114
AS115
AS116
AS117
AS118
AS119
AS120
AS121
AS122
Absorbance at 230 nm
Normalized SPR Response
Effective Target Off-Rate Constant (s⁻¹)
Retention Volume (mL)
Time (s)
[Effector] (μM)

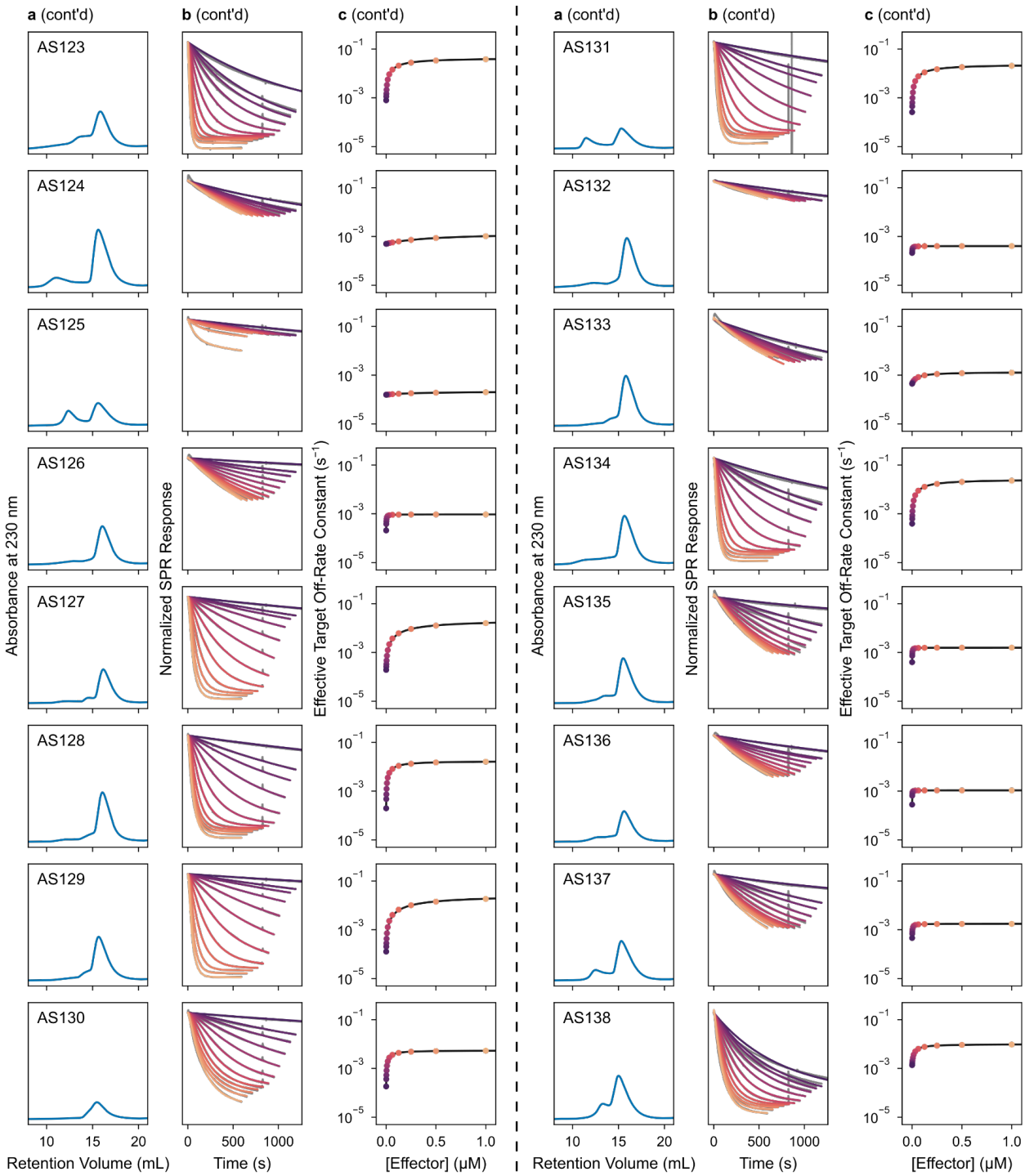

Supplementary Figure 11 | Characterization of AS1 variants. a, SEC host purifications performed on a Superdex 200 Increase 10/300 GL column. **b**, Effector concentration–dependent dissociation of the target upon addition of peptide effector. Data (gray) fit (colors) as described in methods. **c**, Effective target off-rate constants computed from the model fit by ln(2)÷{half-time of target-host interaction} plotted against effector concentration (circles) and fit with hyperbolic equations (black lines).

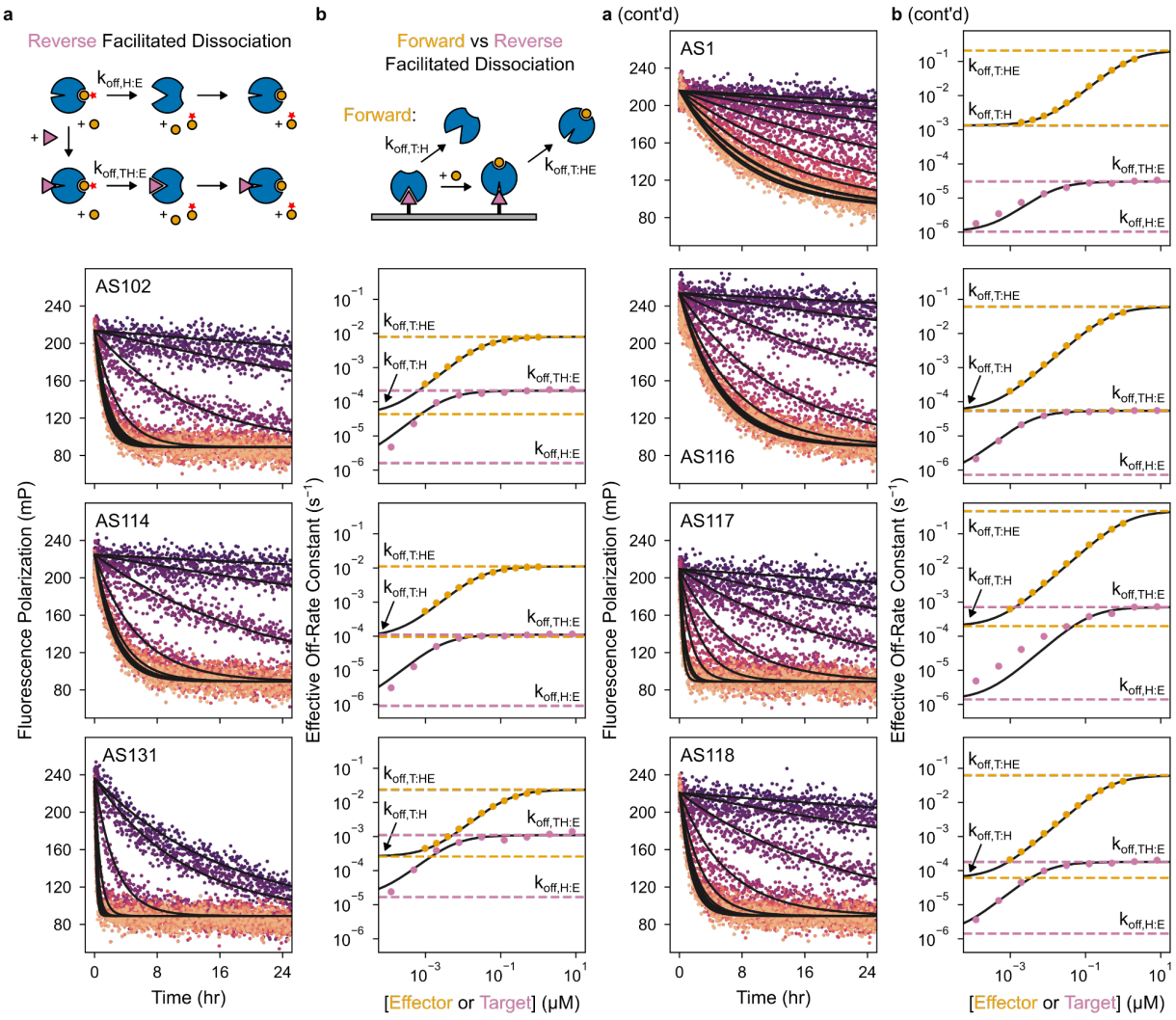

Supplementary Figure 12 | Reverse facilitated dissociation with selected AS1 variants. a, Target concentration–dependent dissociation of TAMRA-labeled effector, made irreversible by the presence of excess unlabeled effector. Fluorescence polarization data (colors) fit (black) with single exponentials. The cartoon shows the pathways of mutually exclusive competition and facilitated dissociation in the reverse competition assay. **b**, Comparison of effective facilitated dissociation rate constants in the forward (orange) and reverse (pink) directions. Forward facilitated dissociation data comes from Fig. 4 and Supplementary Fig. 11. The cartoon illustrates the SPR setup used to measure facilitated dissociation in the forward direction.

The left column shows designs with similar fold accelerations in the forward and reverse directions; the right column shows designs with significantly greater fold acceleration in the forward direction (see Extended Data Fig. 4).

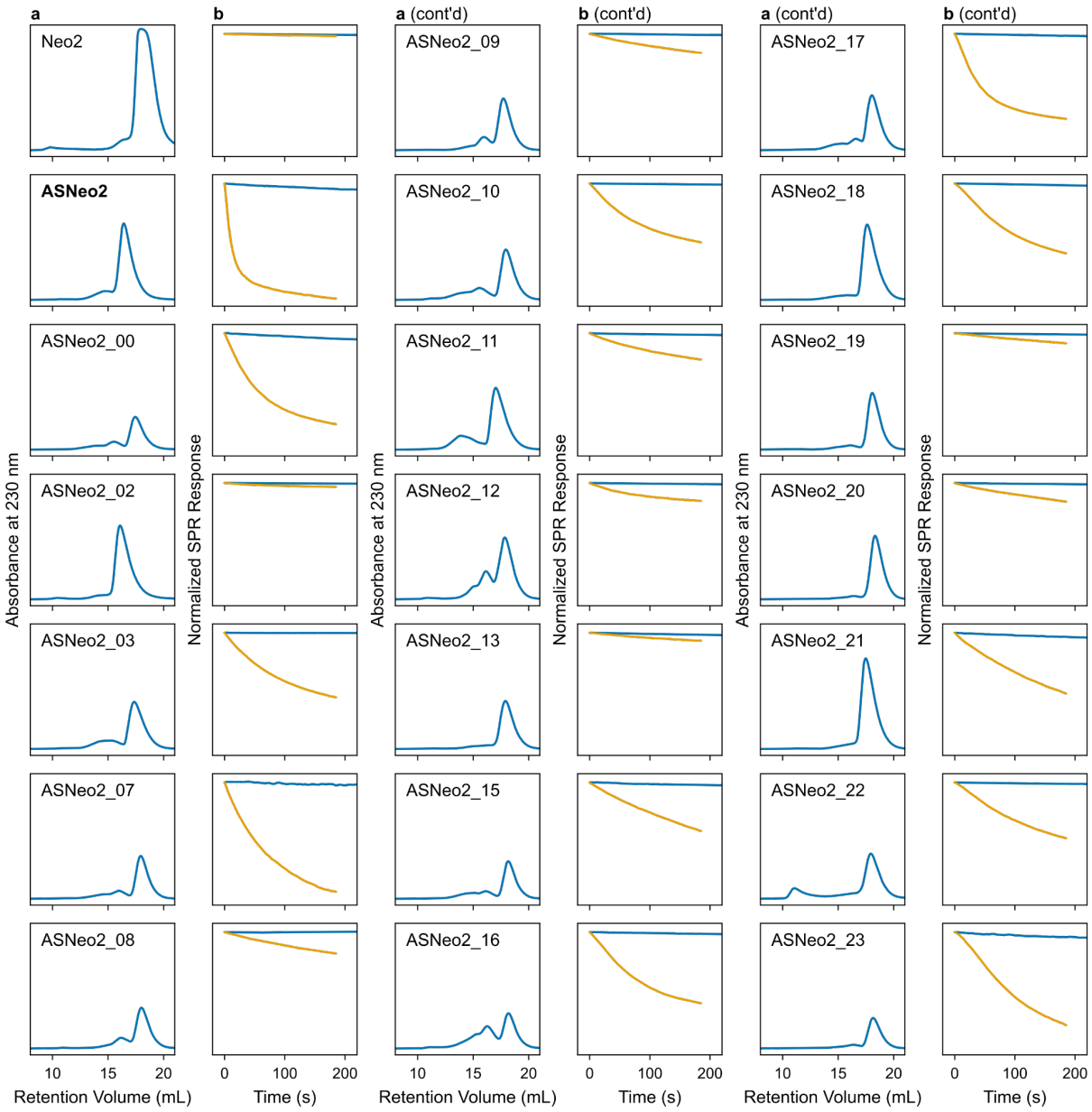

Supplementary Figure 13 | Characterization of initial switchable IL-2 mimic designs. a, SEC purifications performed on a Superdex 200 Increase 10/300 GL column. **b**, Slow dissociation of γ_c from the ASNeo2-IL-2R$\beta\gamma_c$ complex in the absence of effector (blue) and faster dissociation in the presence of effector (orange) as assessed by SPR.

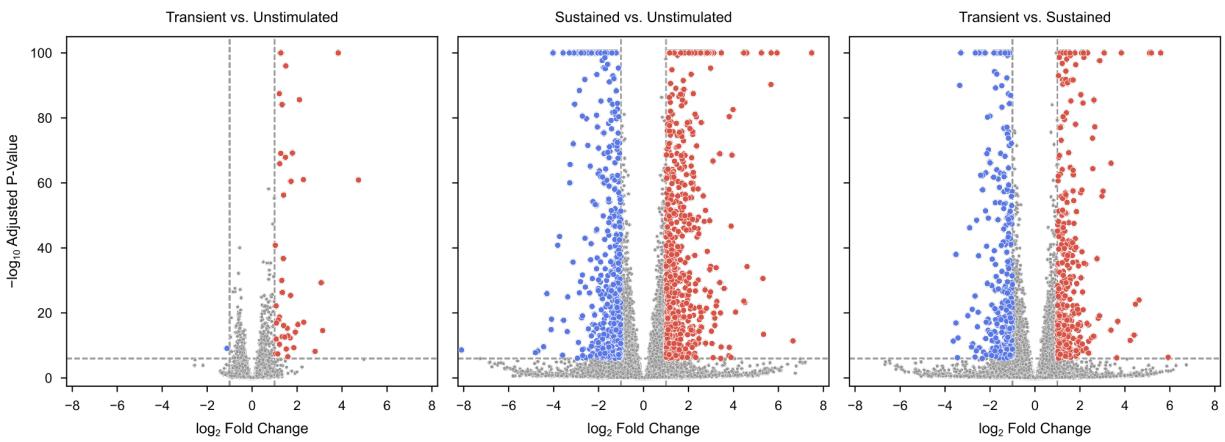

Supplementary Figure 14 | Differences in gene expression between no, transient, and sustained stimulation. Volcano plots showing differences in gene expression between different stimulation conditions. Red: significantly upregulated genes ($\log_2$FC > 1 and $P < 10^{-6}$), blue: significantly downregulated genes ($\log_2$FC < −1 and $P < 10^{-6}$), gray: genes not significantly differentially expressed ($|\log_2 FC| < 1$ or $P > 10^{-6}$). $-\log_{10}$ Adjusted P-value was capped at 100.

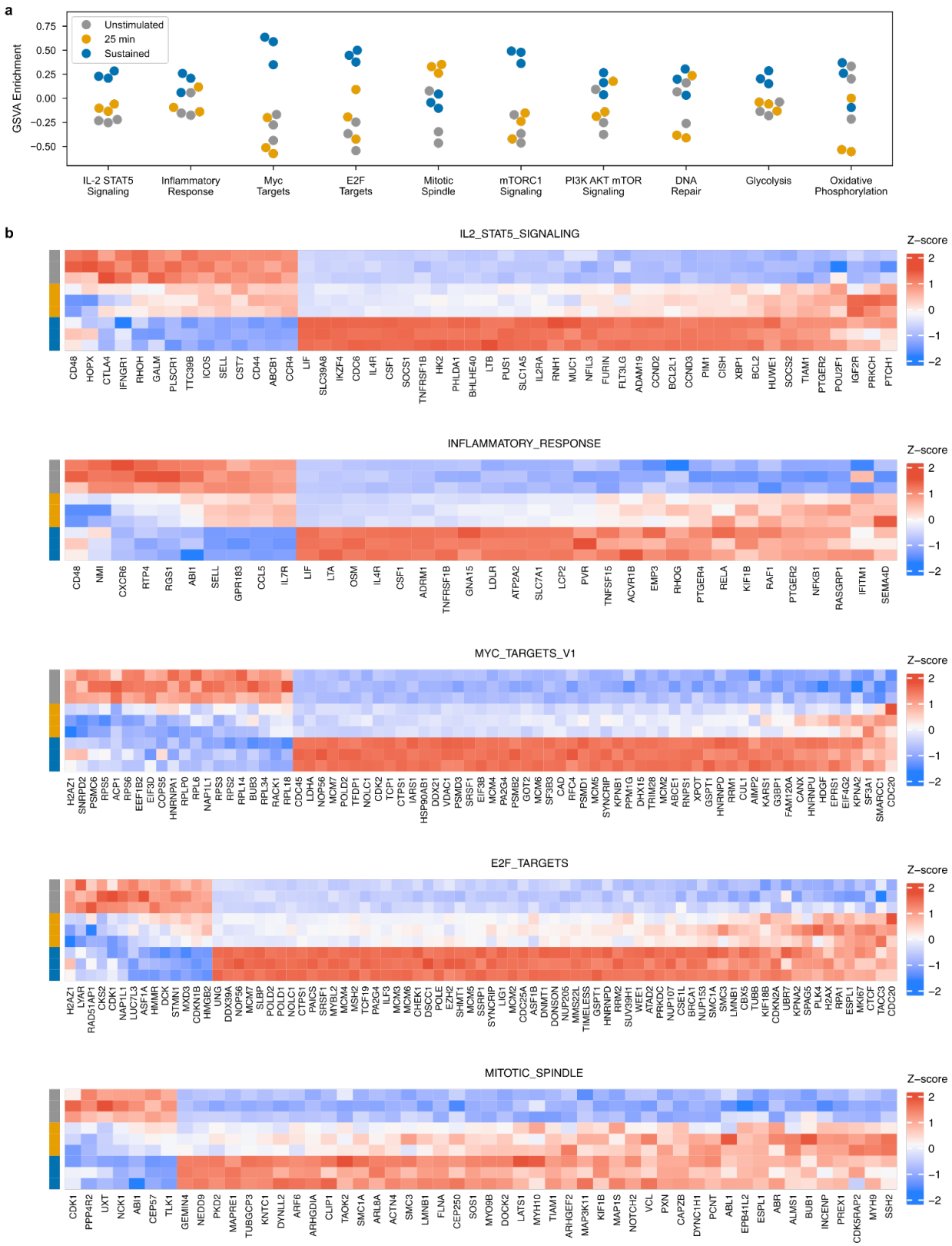
a
GSVA Enrichment
0.75
0.50
0.25
0.00
−0.25
−0.50
Unstimulated
25 min
Sustained
IL-2 STAT5 Signaling
Inflammatory Response
Myc Targets
E2F Targets
Mitotic Spindle
mTORC1 Signaling
PI3K AKT mTOR Signaling
DNA Repair
Glycolysis
Oxidative Phosphorylation
b
IL2_STAT5_SIGNALING
Z−score
2
1
0
−1
−2
CD48 HOPX CTLA4 IFNGR1 RHOH GALM PLSCR1 TTC39B ICOS SELL CST7 CD44 ABCB1 CCR4 LIF SLC39A8 IKZF4 CDC6 IL4R CSF1 SOCS1 TNFRSF1B HK2 PHLDA1 BHLHE40 LTB PUS1 SLC1A5 IL2RA RNH1 MUC1 NFIL3 FURIN FLT3LG ADAM19 CCND2 BCL2L1 CCND3 PIM1 CISH XBP1 BCL2 HUWE1 SOCS2 TIAM1 PTGER2 POU2F1 IGF2R PRKCH PTCH1
INFLAMMATORY_RESPONSE
Z−score
2
1
0
−1
−2
CD48 NMI CXCR6 RTP4 RGS1 ABI1 SELL GPR183 CCL5 IL7R LIF LTA OSM IL4R CSF1 ADRM1 TNFRSF1B GNA15 LDLR ATP2A2 SLC7A1 LCP2 PVR TNFSF15 ACVR1B EMP3 RHOG PTGER4 RELA KIF1B RAF1 PTGER2 NFKB1 RASGRP1 IFITM1 SEMA4D
MYC_TARGETS_V1
Z−score
2
1
0
−1
−2
H2AZ1 SNRPD2 PSMC6 RPS5 ACP1 RPS6 EEF1B2 EIF3D COPS5 HNRNPA1 RPLP0 RPL6 NAP1L1 RPS3 RPS2 RPL14 BUB3 RPL34 RACK1 RPL18 CDC45 LDHA NOP56 MCM7 POLD2 TFDP1 NOLC1 CDK2 TCP1 CTPS1 IARS1 HSP90AB1 DDX21 VDAC1 PSMD3 SRSF1 EIF3B MCM4 PA2G4 PSMB2 GOT2 MCM6 SF3B3 CAD RFC4 PSMD1 MCM5 SYNCRIP KPNB1 PPM1G DHX15 TRIM28 MCM2 ABCE1 RNPS1 XPOT GSPT1 HNRNPD RRM1 CUL1 AIMP2 KARS1 G3BP1 FAM120A CANX HNRNPU HDGF EPRS1 EIF4G2 KPNA2 SF3A1 SMARCC1 CDC20
E2F_TARGETS
Z−score
2
1
0
−1
−2
H2AZ1 LYAR RAD51AP1 CKS2 CDK1 NAP1L1 LUC7L3 ASF1A HMMR DDX1 STMN1 MXD3 CDKN1B HMGB2 UNG DDX39A NOP56 MCM7 SLBP POLD2 POLD1 NOLC1 CTPS1 PAICS SRSF1 MYBL2 MCM4 MSH2 TCF19 PA2G4 ILF3 MCM3 MCM6 CHEK1 DSCC1 POLE EZH2 SHMT1 MCM5 SSRP1 SYNCRIP LIG1 MCM2 CDC25A ASF1B DNMT1 DONSON NUP205 MMS22L TIMELESS GSPT1 HNRNPD RRM2 SUV39H1 WEE1 ATAD2 PRKDC NUP107 CSE1L BRCA1 NUP153 SMC1A SMC3 LMNB1 CBX5 TUBB KIF18B CDKN2A UBR7 KPNA2 SPAG5 PLK4 H2AX RPA1 ESPL1 MKI67 CTCF TACC3 CDC20
MITOTIC_SPINDLE
Z−score
2
1
0
−1
−2
CDK1 PPP4R2 UXT NCK1 ABI1 CEP57 TLK1 GEMIN4 NEDD9 PKD2 MAPRE1 TUBGCP3 KNTC1 DYNLL2 ARF6 ARHGDIA CLIP1 TAOK2 SMC1A ARL8A ACTN4 SMC3 LMNB1 FLNA CEP250 SOS1 MYO9B DOCK2 LATS1 MYH10 TIAM1 ARHGEF2 MAP3K11 KIF1B MAP1S NOTCH2 VCL PXN CAPZB DYNC1H1 PCNT ABL1 EPB41L2 ESPL1 ABR ALMS1 BUB1 INCENP PREX1 CDK5RAP2 MYH9 SSH2

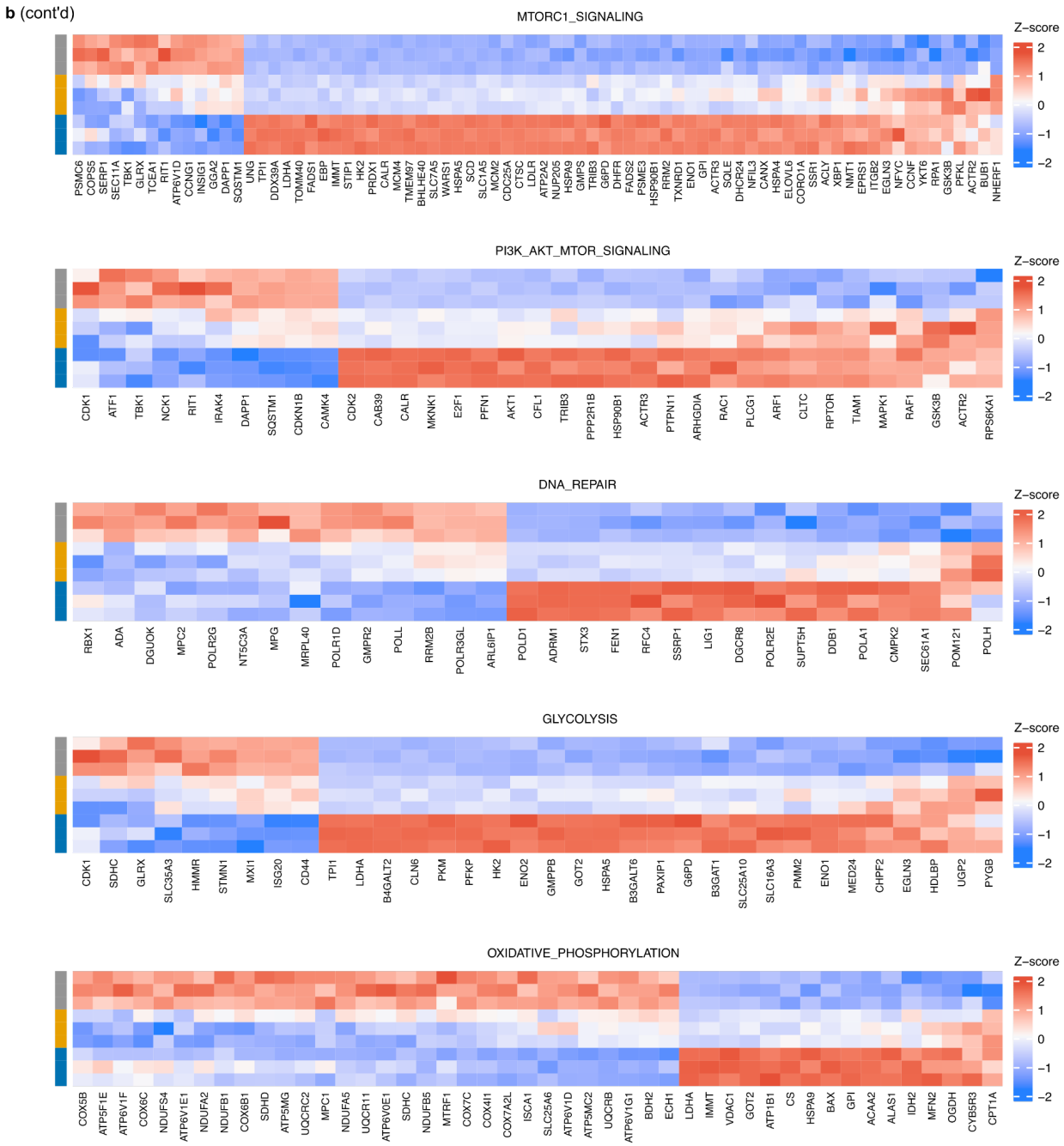

Supplementary Figure 15 | Variation in gene sets following different stimulation conditions. **a**, Gene set variation analysis (GSVA) for relevant hallmark genesets with statistically significant gene correlation, as identified by gene set co-regulation analysis (GESECA). Enrichment scores are shown for each replicate of each stimulation condition. **b**, Heatmaps of differentially expressed genes for each geneset.

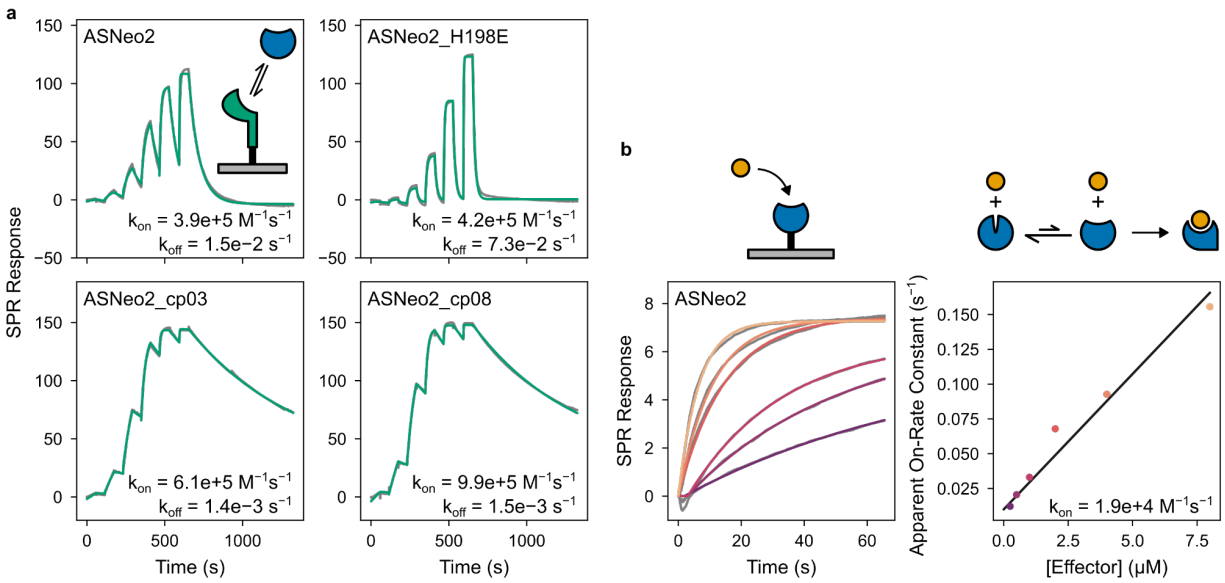

Supplementary Figure 16 | Additional kinetic characterization of ASNeo2 and variants. a, Single-cycle kinetics for ASNeo2 and selected variants binding IL-2Rβ. The mutant H198E reduces the ASNeo2:IL-2Rβ affinity by 5-fold. The cyclic permutations bind IL-2Rβ significantly stronger, perhaps because they lack helix 9 of the original ASNeo2 which may slightly sterically hinder binding to IL-2Rβ. **b**, (Left) effector association with ASNeo2; data (gray) fit with single exponentials (colors). (Right) apparent on-rate constants plotted against effector concentration (circles) and a linear fit. This on-rate is 10-fold slower than that between the effector and AS1, suggesting that the effector binding cleft is predominantly collapsed and the apparent on-rate is thus reduced by a rapid pre-equilibrium between the collapsed and intact conformations.

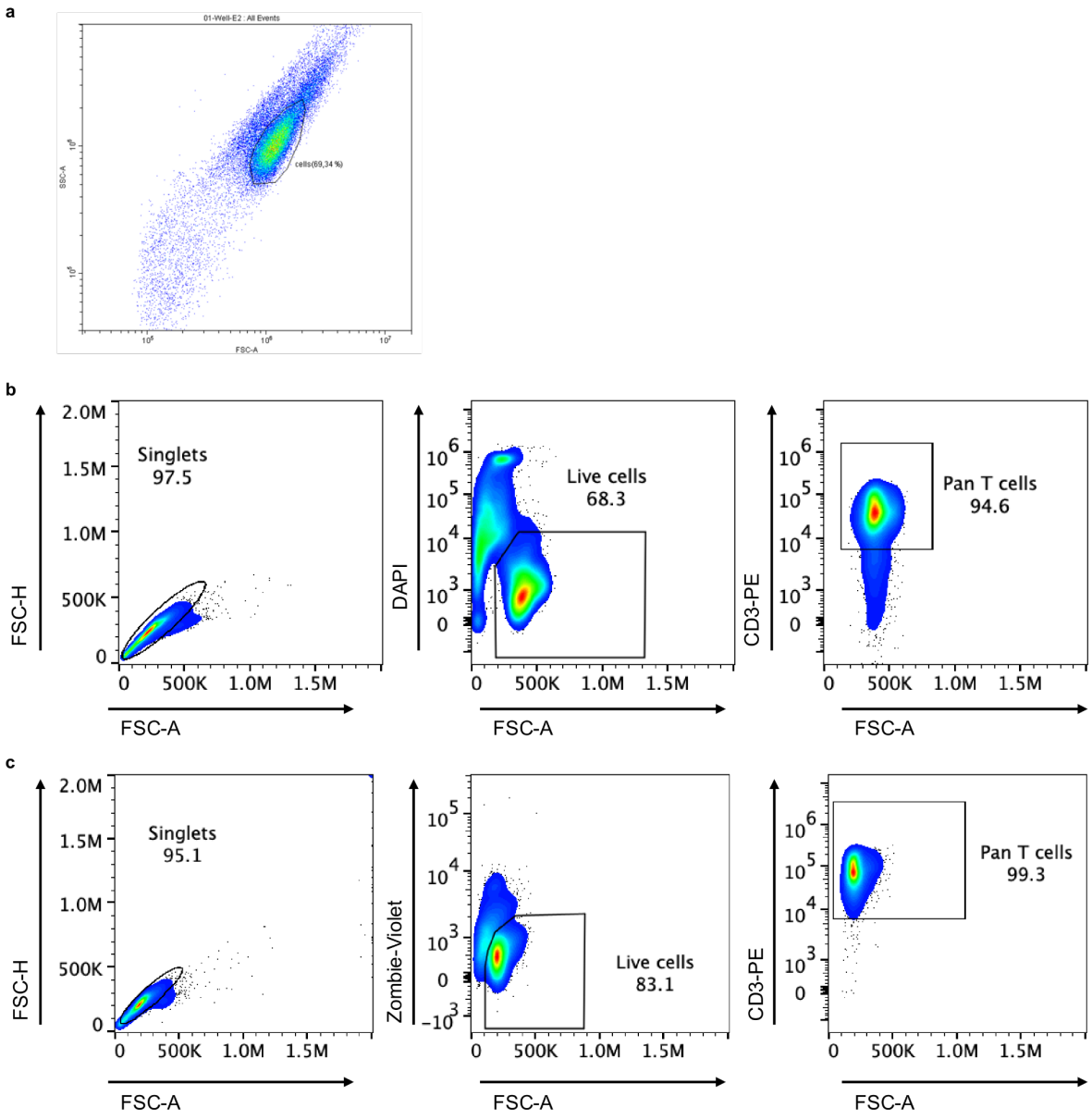

Supplementary Figure 17 | Flow cytometry gating. a, Gating strategy for YT cell identification in Fig. 9g,h based on forward/side scatter profiles. **b**, Gating strategy for T cell phenotyping shown in Fig. 9i,j and Extended Data Fig. 9a–d. Divided cells were gated within the CD3⁺ T cell population after sequential gating on single, live cells. **c**, Gating strategy for T cell phenotyping in Extended Data Fig. 9e–g. Apoptotic and IL-2 downstream signaling markers were analyzed within CD3⁺ T cells after gating on single, live cells.

Supplementary Table 1 | Kinetic parameters from forward and reverse facilitated dissociation experiments with target and peptide effector.

Design	$k_{off,T:H}$ (s^{-1})	$k_{off,T:HE}$ (s^{-1})	Peptide Effector EC_{50} (nM)	$k_{off,H:E}$ (s^{-1})	$k_{off,TH:E}$ (s^{-1})	Target EC_{50} (nM)
LHD101B4	8.6e–5	-	-	-	-	-
AS0	1.6e–4	1.4e–1	6500	-	-	-
AS1	1.4e–3	2.1e–1	130	1.0e–6	3.0e–5	2.2
AS2	3.4e–4	4.4e–2 (1.7e–2)	82	-	-	-
AS5	4.4e–4	3.1e–2	11	-	-	-
AS7	3.4e–3	7.7e–2 (3.3e–2)	130	-	-	-
AS101	6.7e–4	2.4e–3	5.1	-	-	-
AS102	4.3e–5	8.1e–3	2.2	1.6e–6	2.1e–4	0.26
AS103	4.7e–4	9.1e–3	3.5	-	-	-
AS104	2.7e–4	2.7e–3	0.84	-	-	-
AS107	2.9e–4	1.8e–3	0.38	-	-	-
AS108	2.1e–4	6.1e–3	2.4	-	-	-
AS109	2.2e–4	9.2e–3	3.4	-	-	-
AS111	3.2e–4	7.6e–3	4.1	-	-	-
AS113	4.9e–4	8.0e–4	110	-	-	-
AS114	9.6e–5	1.1e–2	2.7	9.0e–7	1.1e–4	0.23
AS115	2.8e–4	8.9e–4	3.3	-	-	-
AS116	5.6e–5	6.1e–2	14	7.3e–7	5.4e–5	0.37
AS117	2.0e–4	4.6e–1	25	1.4e–6	7.1e–4	5.5
AS118	6.1e–5	6.2e–2	14	1.4e–6	1.8e–4	0.63
AS119	4.7e–4	1.1e–3	94	-	-	-
AS120	2.6e–4	2.4e–3	4.2	-	-	-
AS121	6.3e–4	3.1e–2	7.9	-	-	-
AS122	5.1e–4	2.7e–3	29	-	-	-
AS123	7.9e–4	4.4e–2	19	-	-	-

AS124	5.0e–4	1.5e–3	490	-	-	-
AS125	1.6e–4	2.1e–4	320	-	-	-
AS126	2.1e–4	9.4e–4	1.5	-	-	-
AS127	1.9e–4	2.2e–2	33	-	-	-
AS128	2.0e–4	1.7e–2	7.5	-	-	-
AS129	1.3e–4	2.6e–2	28	-	-	-
AS130	1.8e–4	5.5e–3	5.9	-	-	-
AS131	2.6e–4	2.4e–2	15	1.7e–5	1.1e–3	0.62
AS132	2.1e–4	4.1e–4	2.4	-	-	-
AS133	4.5e–4	1.3e–3	46	-	-	-
AS134	3.9e–4	2.6e–2	16	-	-	-
AS135	4.0e–4	1.6e–3	1.3	-	-	-
AS136	2.8e–4	1.1e–3	0.57	-	-	-
AS137	4.6e–4	1.8e–3	2.5	-	-	-
AS138	1.4e–3	9.9e–3	16	-	-	-
ASNeo2	1.6e–4	2.4e–1	480	-	-	-
ASNeo2_cp03	1.5e–4	9.3e–2	36	-	-	-
ASNeo2_cp08	4.1e–5	2.4e–1	170	-	-	-
ASNeo2_cp12	6.4e–5	1.6e–1	280	-	-	-

Values in parentheses give the maximum rate constant of target dissociation induced by effector binding (the full facilitated dissociation pathway), if significantly different from the value of $k_{off,T:HE}$ measured directly by forming the ternary complex on the SPR chip. The EC_{50} is the concentration of effector required to achieve half the total acceleration of target dissociation on a log scale.

Supplementary Table 2 | Kinetic parameters from facilitated dissociation with 3hb effector.

Design	$k_{off,T:H}$ (s^{-1})	k_{switch} (s^{-1})	3hb Effector EC_{50} (nM)	3hb Effector $k_{off,T:HE}$ (s^{-1})	Peptide Effector $k_{off,T:HE}$ (s^{-1})
AS0	1.6e–4	5.1e–4	390	3.0e–1	1.4e–1
AS1	1.4e–3	1.7e–2	57	2.9e–1	2.1e–1
AS2	3.4e–4	3.7e–3	28	1.4e–1	4.4e–2
AS5	4.4e–4	1.4e–2	27	1.0e–1	3.3e–2
AS7	3.4e–3	1.9e–2	40	1.3e–1	7.7e–2
AS114	9.6e–5	-	-	4.7e–2	9.3e–3
AS118	6.1e–5	-	-	9.3e–2	7.4e–2

k_{switch} is the maximum rate constant of target dissociation induced by 3hb effector binding (the full facilitated dissociation pathway rate-limited by the switch conformational change). $k_{off,T:HE}$ is measured directly by forming the ternary complex on the SPR chip. Notably, $k_{off,T:HE}$ is nearly always higher with the 3hb effector than with the peptide, suggesting that the more rigid 3hb effector more effectively can localize strain to the target interface. The EC_{50} is the concentration of effector required to achieve half the total acceleration of target dissociation on a log scale.

Supplementary Table 3 | DEER experimental and fit parameters.

Construct	Sites	State	τ_2 (µs)	Δt (ns)	Scans	λ	SNR	t_0 offset (ns)	α
AS1	R35R1 E173R1	H	6.000	22	47	0.49	117	84.6	23.89
AS1	R35R1 E173R1	T+H	6.000	22	53	0.45	47	113.9	36.92
AS1	R35R1 E173R1	H+E	6.000	22	85	0.46	87	98.4	40.00
AS1	R35R1 E173R1	T+H+E	6.000	22	135	0.42	46	124.2	10.71
AS114	E31R1 E165R1	H	7.000	22	27	0.47	32	91.5	50.00
AS114	E31R1 E165R1	T+H	6.000	22	93	0.38	60	79.4	6.46
AS114	E31R1 E165R1	H+E	6.000	22	140	0.42	89	91.5	7.06
AS114	E31R1 E165R1	T+H+E	6.000	22	138	0.43	70	86.3	22.06

Δt - Pump pulse time step
λ - Modulation depth
SNR - Signal-to-noise
α - Smoothing parameter

References

1. Frauenfelder, H., Sligar, S. G. & Wolynes, P. G. The Energy Landscapes and Motions of Proteins. *Science* **254**, 1598–1603 (1991).

2. Di Cera, E. Mechanisms of ligand binding. *Biophys. Rev.* **1**, 011303 (2020).

3. Huang, P.-S., Boyken, S. E. & Baker, D. The coming of age of de novo protein design. *Nature* **537**, 320–327 (2016).

4. Watson, J. L. *et al.* De novo design of protein structure and function with RFdiffusion. *Nature* **620**, 1089–1100 (2023).

5. Dauparas, J. *et al.* Robust deep learning–based protein sequence design using ProteinMPNN. *Science* **378**, 49–56 (2022).

6. Jumper, J. *et al.* Highly accurate protein structure prediction with AlphaFold. *Nature* **596**, 583–589 (2021).

7. Praetorius, F. *et al.* Design of stimulus-responsive two-state hinge proteins. *Science* **381**, 754–760 (2023).

8. Bogetti, A. T., Presti, M. F., Loh, S. N. & Chong, L. T. The Next Frontier for Designing Switchable Proteins: Rational Enhancement of Kinetics. *J. Phys. Chem. B* **125**, 9069–9077 (2021).

9. Alberstein, R. G., Guo, A. B. & Kortemme, T. Design principles of protein switches. *Curr. Opin. Struct. Biol.* **72**, 71–78 (2022).

10. Huang, P.-S. *et al.* RosettaRemodel: A Generalized Framework for Flexible Backbone Protein Design. *PLOS ONE* **6**, e24109 (2011).

11. Koga, N. *et al.* Principles for designing ideal protein structures. *Nature* **491**, 222–227 (2012).

12. Huang, P.-S. *et al.* High thermodynamic stability of parametrically designed helical bundles. *Science* **346**, 481–485 (2014).

13. Howard, J. Protein power strokes. *Curr. Biol.* **16**, R517–R519 (2006).

14. Ferreiro, D. U., Komives, E. A. & Wolynes, P. G. Frustration in biomolecules. *Q. Rev. Biophys.* **47**, 285–363 (2014).

15. Bergqvist, S. *et al.* Kinetic enhancement of NF-κB·DNA dissociation by IκBα. *Proc. Natl. Acad. Sci.* **106**, 19328–19333 (2009).

16. Kamar, R. I. *et al.* Facilitated dissociation of transcription factors from single DNA binding sites. *Proc. Natl. Acad. Sci.* **114**, E3251–E3257 (2017).

17. Sottini, A. *et al.* Polyelectrolyte interactions enable rapid association and dissociation in high-affinity disordered protein complexes. *Nat. Commun.* **11**, 5736 (2020).

18. Holzbaur, E. L. F. & Johnson, K. A. Microtubules accelerate ADP release by dynein. *Biochemistry* **28**, 7010–7016 (1989).

19. Reubold, T. F., Eschenburg, S., Becker, A., Kull, F. J. & Manstein, D. J. A structural model for actin-induced nucleotide release in myosin. *Nat. Struct. Mol. Biol.* **10**, 826–830 (2003).

20. Packschies, L. *et al.* GrpE Accelerates Nucleotide Exchange of the Molecular Chaperone DnaK with an Associative Displacement Mechanism. *Biochemistry* **36**, 3417–3422 (1997).

21. Singh, A. K. *et al.* Substrate-Induced Facilitated Dissociation of the Competitive Inhibitor from the Active Site of O-Acetyl Serine Sulfhydrylase Reveals a Competitive-Allostery Mechanism. *Biochemistry* **56**, 5011–5025 (2017).

22. Abdiche, Y. N. *et al.* Antibodies Targeting Closely Adjacent or Minimally Overlapping Epitopes Can Displace One Another. *PLOS ONE* **12**, e0169535 (2017).

23. Berlow, R. B., Dyson, H. J. & Wright, P. E. Hypersensitive termination of the hypoxic response by a disordered protein switch. *Nature* **543**, 447–451 (2017).

24. Kim, B. *et al.* Accelerated disassembly of IgE–receptor complexes by a disruptive macromolecular inhibitor. *Nature* **491**, 613–617 (2012).

25. Pennington, L. F. *et al.* Directed evolution of and structural insights into antibody-mediated disruption of a stable receptor-ligand complex. *Nat. Commun.* **12**, 7069 (2021).

26. Alverdi, V., Hetrick, B., Joseph, S. & Komives, E. A. Direct observation of a transient ternary complex during IκBα-mediated dissociation of NF-κB from DNA. *Proc. Natl. Acad. Sci.* **111**, 225–230 (2014).

27. Potoyan, D. A., Zheng, W., Komives, E. A. & Wolynes, P. G. Molecular stripping in the NF-κB/IκB/DNA genetic regulatory network. *Proc. Natl. Acad. Sci.* **113**, 110–115 (2016).

28. Chen, W., Lu, W., Wolynes, P. G. & Komives, E. A. Single-molecule conformational dynamics of a transcription factor reveals a continuum of binding modes controlling association and dissociation. *Nucleic Acids Res.* **49**, 11211–11223 (2021).

29. Berlow, R. B., Martinez-Yamout, M. A., Dyson, H. J. & Wright, P. E. Role of Backbone Dynamics in Modulating the Interactions of Disordered Ligands with the TAZ1 Domain of the CREB-Binding Protein. *Biochemistry* **58**, 1354–1362 (2019).

30. Davies, A. M. *et al.* Allosteric mechanism of action of the therapeutic anti-IgE antibody omalizumab. *J. Biol. Chem.* **292**, 9975–9987 (2017).

31. Erbaş, A. & Marko, J. F. How do DNA-bound proteins leave their binding sites? The role of facilitated dissociation. *Curr. Opin. Chem. Biol.* **53**, 118–124 (2019).

32. Åberg, C., Duderstadt, K. E. & van Oijen, A. M. Stability versus exchange: a paradox in DNA replication. *Nucleic Acids Res.* **44**, 4846–4854 (2016).

33. Zhang, D. Y. & Seelig, G. Dynamic DNA nanotechnology using strand-displacement reactions. *Nat. Chem.* **3**, 103–113 (2011).

34. Sarraf, N., Rodriguez, K. R. & Qian, L. Modular reconfiguration of DNA origami assemblies using tile displacement. *Sci. Robot.* **8**, eadf1511 (2023).

35. Miyashita, O., Onuchic, J. N. & Wolynes, P. G. Nonlinear elasticity, proteinquakes, and the energy landscapes of functional transitions in proteins. *Proc. Natl. Acad. Sci.* **100**, 12570–12575 (2003).

36. Wang, H. & Oster, G. Ratchets, power strokes, and molecular motors. *Appl. Phys. A* **75**, 315–323 (2002).

37. Pennington, L. F. *et al.* Structural basis of omalizumab therapy and omalizumab-mediated IgE exchange. *Nat. Commun.* **7**, 11610 (2016).

38. Sahtoe, D. D. *et al.* Reconfigurable asymmetric protein assemblies through implicit negative design. *Science* **375**, eabj7662 (2022).

39. Huang, Y. & Liu, Z. Kinetic Advantage of Intrinsically Disordered Proteins in Coupled Folding–Binding Process: A Critical Assessment of the “Fly-Casting” Mechanism. *J. Mol. Biol.* **393**, 1143–1159 (2009).

40. Galburt, E. A. & Tomko, E. J. Conformational selection and induced fit as a useful framework for molecular motor mechanisms. *Biophys. Chem.* **223**, 11–16 (2017).

41. Wagoner, J. A. & Dill, K. A. Molecular Motors: Power Strokes Outperform Brownian Ratchets. *J. Phys. Chem. B* **120**, 6327–6336 (2016).

42. Arai, M., Sugase, K., Dyson, H. J. & Wright, P. E. Conformational propensities of intrinsically disordered proteins influence the mechanism of binding and folding. *Proc. Natl. Acad. Sci.* **112**, 9614–9619 (2015).

43. Dietz, H., Berkemeier, F., Bertz, M. & Rief, M. Anisotropic deformation response of single protein molecules. *Proc. Natl. Acad. Sci.* **103**, 12724–12728 (2006).

44. West, D. K., Brockwell, D. J., Olmsted, P. D., Radford, S. E. & Paci, E. Mechanical Resistance of Proteins Explained Using Simple Molecular Models. *Biophys. J.* **90**, 287–297 (2006).

45. Paramanathan, T., Reeves, D., Friedman, L. J., Kondev, J. & Gelles, J. A general mechanism for competitor-induced dissociation of molecular complexes. *Nat. Commun.* **5**, 5207 (2014).

46. Dixon, A. S. *et al.* NanoLuc Complementation Reporter Optimized for Accurate Measurement of Protein Interactions in Cells. *ACS Chem. Biol.* **11**, 400–408 (2016).

47. Quijano-Rubio, A. *et al.* De novo design of modular and tunable protein biosensors. *Nature* **591**, 482–487 (2021).

48. Jackson, C., Anderson, A. & Alexandrov, K. The present and the future of protein biosensor engineering. *Curr. Opin. Struct. Biol.* **75**, 102424 (2022).

49. Cao, L. *et al.* De novo design of picomolar SARS-CoV-2 miniprotein inhibitors. *Science* **370**, 426–431 (2020).

50. Copeland, R. A. The drug–target residence time model: a 10-year retrospective. *Nat. Rev. Drug Discov.* **15**, 87–95 (2016).

51. Moraga, I. *et al.* Instructive roles for cytokine-receptor binding parameters in determining signaling and functional potency. *Sci. Signal.* **8**, ra114–ra114 (2015).

52. Martinez-Fabregas, J. *et al.* Kinetics of cytokine receptor trafficking determine signaling and functional selectivity. *eLife* **8**, e49314 (2019).

53. Shouse, A. N., LaPorte, K. M. & Malek, T. R. Interleukin-2 signaling in the regulation of T cell biology in autoimmunity and cancer. *Immunity* **57**, 414–428 (2024).

54. Lowenthal, J. W. *et al.* High and low affinity IL 2 receptors: analysis by IL 2 dissociation rate and reactivity with monoclonal anti-receptor antibody PC61. *J. Immunol.* **135**, 3988–3994 (1985).

55. Fujii, M. *et al.* High-affinity receptor-mediated internalization and degradation of interleukin 2 in human T cells. *J. Exp. Med.* **163**, 550–562 (1986).

56. Silva, D.-A. *et al.* De novo design of potent and selective mimics of IL-2 and IL-15. *Nature* **565**, 186–191 (2019).

57. Quijano-Rubio, A. *et al.* A split, conditionally active mimetic of IL-2 reduces the toxicity of systemic cytokine therapy. *Nat. Biotechnol.* **41**, 532–540 (2023).

58. Arneja, A., Johnson, H., Gabrovsek, L., Lauffenburger, D. A. & White, F. M. Qualitatively Different T Cell Phenotypic Responses to IL-2 versus IL-15 Are Unified by Identical Dependences on Receptor Signal Strength and Duration. *J. Immunol.* **192**, 123–135 (2014).

59. Jones, R. G. & Thompson, C. B. Revving the Engine: Signal Transduction Fuels T Cell Activation. *Immunity* **27**, 173–178 (2007).

60. Khalil, A. S. *et al.* Kinesin's cover-neck bundle folds forward to generate force. *Proc. Natl. Acad. Sci.* **105**, 19247–19252 (2008).

61. Robustelli, P., Piana, S. & Shaw, D. E. Mechanism of Coupled Folding-upon-Binding of an Intrinsically Disordered Protein. *J. Am. Chem. Soc.* **142**, 11092–11101 (2020).

62. Kumar, A., Moreau, J. L., Gibert, M. & Thèze, J. Internalization of interleukin 2 (IL-2) by high affinity IL-2 receptors is required for the growth of IL-2-dependent T cell lines. *J. Immunol.* **139**, 3680–3684 (1987).

63. Wang, J. *et al.* Scaffolding protein functional sites using deep learning. *Science* **377**, 387–394 (2022).

64. Alford, R. F. *et al.* The Rosetta All-Atom Energy Function for Macromolecular Modeling and Design. *J. Chem. Theory Comput.* **13**, 3031–3048 (2017).

65. Bennett, N. R. *et al.* Improving de novo protein binder design with deep learning. *Nat. Commun.* **14**, 2625 (2023).

66. Brunette, T. J. *et al.* Exploring the repeat protein universe through computational protein design. *Nature* **528**, 580–584 (2015).

67. Wicky, B. I. M. *et al.* Hallucinating symmetric protein assemblies. *Science* **378**, 56–61 (2022).

68. Dang, B. *et al.* SNAC-tag for sequence-specific chemical protein cleavage. *Nat. Methods* **16**, 319–322 (2019).

69. Walter, T. S. *et al.* Lysine Methylation as a Routine Rescue Strategy for Protein Crystallization. *Structure* **14**, 1617–1622 (2006).

70. Kabsch, W. XDS. *Acta Crystallogr. D Biol. Crystallogr.* **66**, 125–132 (2010).

71. Winn, M. D. *et al.* Overview of the CCP4 suite and current developments. *Acta Crystallogr. D Biol. Crystallogr.* **67**, 235–242 (2011).

72. McCoy, A. J. *et al.* Phaser crystallographic software. *J. Appl. Crystallogr.* **40**, 658–674 (2007).

73. Adams, P. D. *et al.* PHENIX: a comprehensive Python-based system for macromolecular structure solution. *Acta Crystallogr. D Biol. Crystallogr.* **66**, 213–221 (2010).

74. Emsley, P. & Cowtan, K. Coot: model-building tools for molecular graphics. *Acta Crystallogr. D Biol. Crystallogr.* **60**, 2126–2132 (2004).

75. Williams, C. J. *et al.* MolProbity: More and better reference data for improved all-atom structure validation. *Protein Sci.* **27**, 293–315 (2018).

76. Tessmer, M. H. & Stoll, S. chiLife: An open-source Python package for in silico spin labeling and integrative protein modeling. *PLOS Comput. Biol.* **19**, e1010834 (2023).

77. Tessmer, M. H., Canarie, E. R. & Stoll, S. Comparative evaluation of spin-label modeling methods for protein structural studies. *Biophys. J.* **121**, 3508–3519 (2022).

78. Fábregas Ibáñez, L., Jeschke, G. & Stoll, S. DeerLab: a comprehensive software package for analyzing dipolar electron paramagnetic resonance spectroscopy data. *Magn. Reson.* **1**, 209–224 (2020).

79. Hasanbasri, Z., H. Tessmer, M., Stoll, S. & Saxena, S. Modeling of Cu(ii)-based protein spin labels using rotamer libraries. *Phys. Chem. Chem. Phys.* **26**, 6806–6816 (2024).

80. Jo, S., Kim, T., Iyer, V. G. & Im, W. CHARMM-GUI: A web-based graphical user interface for CHARMM. *J. Comput. Chem.* **29**, 1859–1865 (2008).

81. Lee, J. *et al.* CHARMM-GUI Input Generator for NAMD, GROMACS, AMBER, OpenMM, and CHARMM/OpenMM Simulations Using the CHARMM36 Additive Force Field. *J. Chem. Theory Comput.* **12**, 405–413 (2016).

82. Huang, J. *et al.* CHARMM36m: an improved force field for folded and intrinsically disordered proteins. *Nat. Methods* **14**, 71–73 (2017).

83. Berendsen, H. J. C., van der Spoel, D. & van Drunen, R. GROMACS: A message-passing parallel molecular dynamics implementation. *Comput. Phys. Commun.* **91**, 43–56 (1995).

84. Van Der Spoel, D. *et al.* GROMACS: Fast, flexible, and free. *J. Comput. Chem.* **26**, 1701–1718 (2005).

85. Hess, B., Bekker, H., Berendsen, H. J. C. & Fraaije, J. G. E. M. LINCS: A linear constraint solver for molecular simulations. *J. Comput. Chem.* **18**, 1463–1472 (1997).

86. Michaud-Agrawal, N., Denning, E. J., Woolf, T. B. & Beckstein, O. MDAnalysis: A toolkit for the analysis of molecular dynamics simulations. *J. Comput. Chem.* **32**, 2319–2327 (2011).

87. Daura, X. *et al.* Peptide Folding: When Simulation Meets Experiment. *Angew. Chem. Int. Ed.* **38**, 236–240 (1999).

88. Götzke, H. *et al.* The ALFA-tag is a highly versatile tool for nanobody-based bioscience applications. *Nat. Commun.* **10**, 4403 (2019).

89. Wilmes, S. *et al.* Mechanism of homodimeric cytokine receptor activation and dysregulation by oncogenic mutations. *Science* **367**, 643–652 (2020).

90. Wilmes, S. *et al.* Receptor dimerization dynamics as a regulatory valve for plasticity of type I interferon signaling. *J. Cell Biol.* **209**, 579–593 (2015).

91. Reed, S. E., Staley, E. M., Mayginnes, J. P., Pintel, D. J. & Tullis, G. E. Transfection of mammalian cells using linear polyethylenimine is a simple and effective means of producing recombinant adeno-associated virus vectors. *J. Virol. Methods* **138**, 85–98 (2006).

92. Sotolongo Bellón, J. *et al.* Four-color single-molecule imaging with engineered tags resolves the molecular architecture of signaling complexes in the plasma membrane. *Cell Rep. Methods* **2**, 100165 (2022).

93. You, C., Richter, C. P., Löchte, S., Wilmes, S. & Piehler, J. Dynamic Submicroscopic Signaling Zones Revealed by Pair Correlation Tracking and Localization Microscopy. *Anal. Chem.* **86**, 8593–8602 (2014).

94. Winkelmann, H., Richter, C. P., Eising, J., Piehler, J. & Kurre, R. Correlative single-molecule and structured illumination microscopy of fast dynamics at the plasma membrane. *Nat. Commun.* **15**, 5813 (2024).

95. Edelstein, A. D. *et al.* Advanced methods of microscope control using μManager software. *J. Biol. Methods* **1**, 1 (2014).

96. Sergé, A., Bertaux, N., Rigneault, H. & Marguet, D. Dynamic multiple-target tracing to probe spatiotemporal cartography of cell membranes. *Nat. Methods* **5**, 687–694 (2008).

97. Niewidok, B. *et al.* Single-molecule imaging reveals dynamic biphasic partition of RNA-binding proteins in stress granules. *J. Cell Biol.* **217**, 1303–1318 (2018).

98. Jaqaman, K. *et al.* Robust single-particle tracking in live-cell time-lapse sequences. *Nat. Methods* **5**, 695–702 (2008).

99. Aguet, F., Antonescu, C. N., Mettlen, M., Schmid, S. L. & Danuser, G. Advances in Analysis of Low Signal-to-Noise Images Link Dynamin and AP2 to the Functions of an Endocytic Checkpoint. *Dev. Cell* **26**, 279–291 (2013).

100. Lee, N. K. *et al.* Accurate FRET Measurements within Single Diffusing Biomolecules Using Alternating-Laser Excitation. *Biophys. J.* **88**, 2939–2953 (2005).

101. Berlow, R. B., Dyson, H. J. & Wright, P. E. Multivalency enables unidirectional switch-like competition between intrinsically disordered proteins. *Proc. Natl. Acad. Sci.* **119**, e2117338119 (2022).

102. Moal, I. H. & Fernández-Recio, J. SKEMPI: a Structural Kinetic and Energetic database of Mutant Protein Interactions and its use in empirical models. *Bioinformatics* **28**, 2600–2607 (2012).

103. Schreiber, G., Haran, G. & Zhou, H.-X. Fundamental Aspects of Protein–Protein Association Kinetics. *Chem. Rev.* **109**, 839–860 (2009).

104. Selzer, T., Albeck, S. & Schreiber, G. Rational design of faster associating and tighter binding protein complexes. *Nat. Struct. Biol.* **7**, 537–541 (2000).